Investigation of the 2^+ Hoyle state candidates in ^{12}C

by

Fhumulani Nemulodi

Dissertation presented for the degree of Doctor of Philosophy

at Stellenbosch University

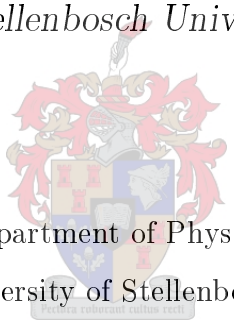

Department of Physics,
University of Stellenbosch,
Private Bag X1, Matieland 7602,
South Africa.

Promoters:

Prof. Paul Papka

Dept. Physics

Dr. Retief Neveling

Dept. of Nuclear Physics, iThemba LABS

March 2015

Declaration

By submitting this dissertation electronically, I declare that the entirety of the work contained therein is my own, original work, that I am the owner of the copyright thereof (unless to the extent explicitly otherwise stated) and that I have not previously in its entirety or in part submitted it for obtaining any qualification.

Signature: ..... Date: .....

Abstract

Over the years the ^{12}C nucleus has proved to be one of the most facinating nuclei to study. This thesis attempts to provide answers regarding some of the open questions regarding certain structural properties of this nucleus. This is done by performing two independent experiments to measure the ^{12}C excitation energy spectrum.

The first experiment was aimed at investigating the existence of the 11.16 MeV 2^+ state claimed to exist in ^{12}C. The measurement was performed with the K600 magnetic spectrometer at iThemba LABS, South Africa, using the ^{11}B(^{3}He,d)^{12}C reaction with a 44 MeV ^{3}He beam at three different laboratory angles θ_{lab} = (25°, 30°, 35°). The results obtained showed no evidence of such a state in ^{12}C and it was concluded that no such state exist. The results also showed signatures of a 2^+ state in the 10 MeV excitation energy region. This state is associated with the 2^+ excitation of the well known Hoyle state reported to exist at this region.

A second experiment was aimed at searching for the 2^+ excitation of the Hoyle state in the 10 MeV excitation energy region. This was achieved by using the ^{14}C(p,t)^{12}C[3α] reaction with a 66 MeV proton beam and observing tritons at a laboratory angle of θ_{lab} = 21°. The measurement was performed with the K600 magnetic spectrometer in conjunction with silicon detectors mounted inside the scattering chamber. The peak fitting analysis performed on a singles event spectrum showed evidence of the population of the 2^+ state at E_x = 9.69 ± 0.11 MeV and width of Γ = 1.43 ± 0.22 MeV. These parameters appear to

shift when the coincidence events are taken into account. The parameters obtained for decay to the ^{8}Be ground state decay mode are $E_x = 9.97 \pm 0.20$ MeV and $\Gamma = 1.03 \pm 0.21$ MeV for energy and width respectively. Whereas, the parameters obtained by gating on other decay modes are $E_x = 9.55 \pm 0.22$ MeV and $\Gamma = 1.15 \pm 0.24$ MeV for energy and width respectively. The newly found state decays predominately via the ^{8}Be ground state decay mode.

Opsomming

Oor die jare heen was die ^{12}C kern nog altyd bekend as 'n fasinerende kern vol geheimenisse. In hierdie tesis word gepoog om antwoorde te verskaf vir ope vraagstukke ten opsigte van die struktuur van hierdie kern. Ten einde hierdie doelwit te bereik is twee onafhanklike eksperimente aangepak opgewekte toestand van ^{12}C te ondersoek.

In die eerste eksperiment word die algemeen aanvaarde aanname ondersoek dat 'n 2^+ toestand by 'n opwekkings energie van 11.16 MeV in ^{12}C bestaan. Die ekspe-rimentele werk is gedoen met behulp van die K600 magnetiese spektrometer by iThemba LABS (Suid Afrika). Die ^{11}B(^{4}He,d)^{12}C reaksie is gebruik vir die ondersoek by drie verskillende verstrooiingshoeke (θ_{lab} = 25°,30°,35°) met 'n 44 MeV ^{3}He bundel. Uit die resultate is dit duidelik dat geen 2^+ toestand waargeneem is in die omgewing van 11.16 MeV nie. Die resultate dui egter op die moontlikheid dat 'n 2^+ toestand bestaan rondom die opwekking energie van 10 MeV. Hierdie toestand, ook waargeneem in ander onlangse eksperimente, word geassosieer met die 2^+ opgewekte toestand van die beroemde Hoyle toestand.

Die doel van die tweede eksperiment was om hierdie 2^+ opgewekte toestand te karakteriseer. 'n Proton bundel met kinetiese energie van 66 MeV is gebruik om die ^{14}C(p,t)^{12}C[3α] reaksie te ondersoek by 'n triton verstrooiingshoek van 21°. Die eksperimentele werk is uitgevoer met behulp van die K600 magnetiese spektrometer tesame met 'n aantal silikon detektors. 'n Piekpassing analise van die opwekking energie spektrum dui op die teenwoordigheid van 'n 2^+

toestand by $E_x = 9.69 \pm 0.11$ MeV met 'n wydte van Γ=1.43 $\pm$ 0.22 MeV. Hierdie parameters blyk te verander wanneer die verval van die toestand deur α-verval in ag geneem word. Die opwekking energie spektrum wat gemeet word in koinsidens met α-verval sodanig dat die oorblywende ^{8}Be kern in die grondtoestand bly dui op 'n 2^+ toestand by $E_x = 9.97 \pm 0.20$ MeV met 'n wydte van $\Gamma = 1.03 \pm 0.21$ MeV. Indien die som totaal van al die ander verval modes beskou word verander die posisie en wydte van die toestand na $E_x = 9.55 \pm 0.22$ MeV en $\Gamma = 1.15 \pm 0.24$ MeV. Dit is bepaal dat die 2^+ toestand hoofsaaklik verval via α-verval wat die oorblywende ^{8}Be kern in die grondtoestand laat.

Acknowledgements

First and foremost, I would like to express special gratitude to my supervisors Prof Paul Papka and Dr Retief Neveling. Thank you for your never ending encouragements, guidance, and for allowing me to grow as a research student. To Prof Papka, thank you for introducing me to this fascinating field of nuclear clustering when we were still working on my honours project. Even though I disappeared for my masters degree, when the opportunity to work together for this PhD thesis availed itself we both jumped into it. For that I would like to say "*merci*". To Dr Neveling "*Captain of the K600*", thank you for keeping your office door open so that I could enter anytime I reached a dead-end. Whenever I have Linux, programming, physics, or spectrometer related problem I still feel free to run to you. "*Ek is daarvoor baie dankbaar.*"
I would also like to thank the following people for their contributions:

- Dr Iyabo Usman for making sure I always had something to keep me busy after joining the K600 group. Those data analysis tasks and DWUCK calculations helped to settle me down.
- Prof Nicholas Keeley for helping me with the FRESCO code and proof-reading the related section.
- Prof Martin Freer for providing me with the R-matrix code and explaining aspects of the code.
- Yvonne Kheswa and Langutani Mathebula for making sure we had a

^{11}B target. Those extra hours you guys put in to make sure this most difficult target was available are very much appreciated.

- Dr Mandla Msimanga for performing the ERDA measurements on the ^{11}B targets.

- My fellow K600 student, Dr Jacobus Swartz, thank you for allowing me to disturb you whenever I required your help. Those valuable discussions in the wee hours of Monday mornings are very much appreciated.

- Dr Evgeni Cherepanov, Dr Andrey Fomichev, Dr Vratislav Chudoba and Bartlomiej Hnatio, our DUBNA collaborators for providing us with the ^{14}C target.

- Dr Ricky Smit for the valuable discussions. Thanks making sure that there are no dull moments during the K600 group meetings and during the setting up of experiments. Please make sure I still get those muffin meeting emails.

- Dr Phillip Adsley for the helpful discussions about the peak fitting analysis.

- The people who made sure the experiments went smoothly by taking shifts: Dr Deon Steyn, Dr Zinhle Buthelezi, Dr Siegie Förtsch, Dr Joele Mira, Dr Jacobus van Zyl, Dr Justin Mabiala, Prof John Carter, Dr Maxwell Jingo, Dr Roger Fearick, and Dr Chamunorwa Kureba. I really appreciate your time.

- Dr Lowry Conradie and his accelerator team for providing us with stable beams.

- The "*IT guys*", Lee Pool and Gareth de Vaux, thank you for helping me with all those Linux related problems, specifically the MIDAS related problems. Thanks to you, I now understand basic Linux gibberish.

Last but not least, I would like to give a special thanks to my family. To my parents, if it was not for you I wouldn't be here today. Thank for raising me the way you did and for your never ending support. To my big brother and two young sisters, thank you for keeping up with me all these times you could not get my attention because I was busy chasing protons "*ndia livhuwa*".

This work would have not been possible without the financial support from the National Research Foundation (NRF) through the Professional Development Program (PDP). The author would like to thank the NRF for their financial assistance and iThemba LABS (nuclear physics department) for providing me with all necessary infrastructure to complete this study.

Contents

List of Figures

List of Tables

Chapter 1

Introduction

The nucleus is usually described as a system having a distribution of nucleons i.e. protons and neutrons as illustrated in the simplified diagram shown in Fig. 1.1. In this configuration, nucleons move freely with the forces acting between them being the long-range repulsive Coulomb force and the short-range nuclear force. The nuclear force is generally considered to be isospin independent, i.e. it behaves in a similar way between two protons, or between two neutrons, or between a neutron and a proton [1]. However, strictly speaking, evidence does exist that the nuclear force depends upon the isospin of the two necleons [2].

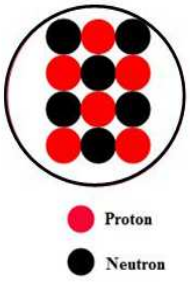

Figure 1.1: The ^{12}C nucleus showing a homogeneous distribution of nucleons.

Although this description is generally accepted, ever since Gamow's theory of α-decay [3] it is also natural to think of nuclei as composed of α-particles,

which are assembled from two protons and two neutrons. This phenomenon is known as α-clustering. It is the process whereby nucleons within a nucleus tend to combine to form a cluster, as illustrated in Fig. 1.2. Such phenomenon is typically observed in α-conjugate nuclei i.e. nuclei that can be broken down into subsets of α-particles, for example ^{8}Be, ^{12}C, and ^{16}O. Over the years it has been postulated that different types of clustering can develop withing the nucleus, for example, the cluster radioactivity, clustering in neutron-rich nuclei, di-neutron clustering, collective clusterization in nuclei and the giant nuclear molecules. A detailed description of these clustering phenomena can be found in Refs. [4, 5].

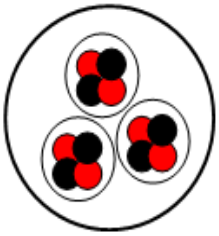

Figure 1.2: An arrangement of three α-particles clusters within the ^{12}C nucleus.

The idea that an α-particle can exist within a nucleus prior to α-decay is strongly supported by some of the structural properties of the α-particle. It is itself a closed shell nucleus, has a high binding energy per nucleon (BE/A = $\sim$7 MeV) and its first excited state lies at E_x = 20.210 MeV above the ground state. Although α-clustering is expected to develop within nuclei, in most nuclei it cannot occur in the ground state. It has been suggested that for cluster structure to develop within the nucleus it must be energetically allowed. This mean that for a nucleus to be separated into its cluster particles, an energy equal to the excess mass difference between the mother nucleus and the clusters must be provided. The energy is defined by

$$E_{\text{th}}[\text{MeV}] = \Delta M_{\text{parent}}[\text{MeV}] - \Delta M_{\text{cluster}}[\text{MeV}], \tag{1.1}$$

where E_{th} is the decay threshold energy (also known as the break-up Q-value), ΔM_{parent} represents the excess mass of the mother nucleus, and $\Delta M_{cluster}$ is the excess mass of the cluster particles. Equation (1.1) implies that the cluster structure would be expected to develop in the excitation energy region close to the decay threshold, E_{th}. In 1968, Ikeda *et al.* [6] used what is commonly referred to as the Ikeda diagram (shown in Fig. 1.3) to illustrate where cluster structures are most likely to occur within different nuclei. They suggested that cluster structures are most expected at an excitation energy which coincides with particular decay thresholds.

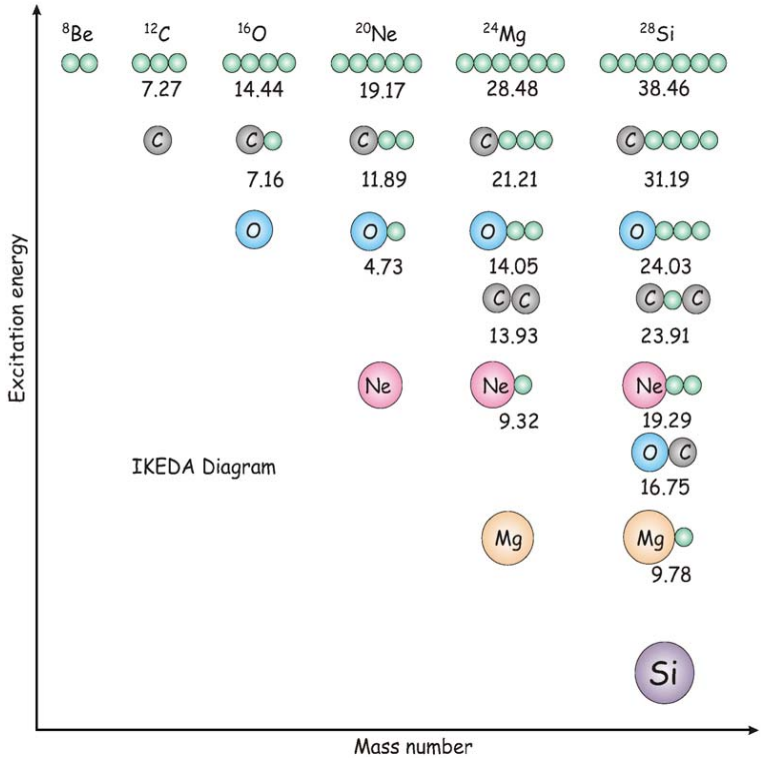

Figure 1.3: The Ikeda diagram showing cluster structures occurring at each decay threshold (in MeV) obtained from Ref. [6].

The α cluster structure in the ^{12}C nucleus is expected at an excitation energy at or higher than the three α-particle decay threshold, as shown in Fig. 1.2. According to Eq. (1.1) the Q-value for this break-up is $\sim$7.27 MeV. Considering these assumptions, one would expect a state which lies in this

region to have a well-developed 3α cluster structure. The configuration of such a state would be interesting to nuclear structure studies. Cluster structure has been identified in the ^{8}Be ground state, which has a well-developed α-α structure [7].

Cluster structures are not only of interest to nuclear structure studies, they are also relevant from a nuclear astrophysics point of view. One famous example is that of Fred Hoyle who studied the synthesis of heavy elements (carbon to nickel) inside stars [8]. He attempted to explain the abundance of carbon in the universe, which is formed through the triple-α process, and suggested that it must not be formed through the ground state but through a specific resonance. He postulated the existence of a $J^{\pi} = 0^{+}$ resonance in ^{12}C close to the threshold of ^{8}Be + α fusion. After the Hoyle's postulation, experimental investigations were performed in order to identify this resonance in ^{12}C. A few years later such a resonance was experimentally confirmed by Cook *et al.* [9] at an excitation energy of 7.654 MeV with $J^{\pi} = 0^{+}$ character as predicted by Hoyle. It was named the "*Hoyle state*" in honour of Fred Hoyle. It is believed that the existence of this specific state is essential for the nucleosynthesis of ^{12}C and other heavy elements such as ^{16}O, ^{20}Ne, ^{24}Mg, *etc.*

From a nuclear structure point of view, the Hoyle state is believed to have a well-developed 3α cluster structure. Since its discovery, the structure of the Hoyle state has been widely investigated both theoretically [10, 11, 12] and experimentally [13, 14, 15, 16]. Its structural properties are, however, still not well understood. To date, several open questions regarding the structural properties of the Hoyle state remain to be answered. Some of the open questions are:

- If the Hoyle state has a well-developed 3α cluster structure, how are the α-particles positioned with respect to each other? Different cluster arrangements have been postulated, as illustrated in Figure 1.4:

  (a) The *linear chain* configuration was postulated by Morinaga in 1956

[17].

(b) In 2001, Tohsaki *et al.* [18] postulated the Hoyle state to be a dilute self-bound gas of bosonic α-particles, similar to a Bose-Einstein condensate (BEC). The Fermionic Molecular Dynamics (FMD) calculations also find the Hoyle state as a gas of dilute α-particles [20].

(c) In 2012, Epelbaum *et al.* [21] calculated the Hoyle state using *ab initio* lattice calculations. They theorized the "*bent-arm*" or obtuse triangular configuration of α-cluster structure of the Hoyle state.

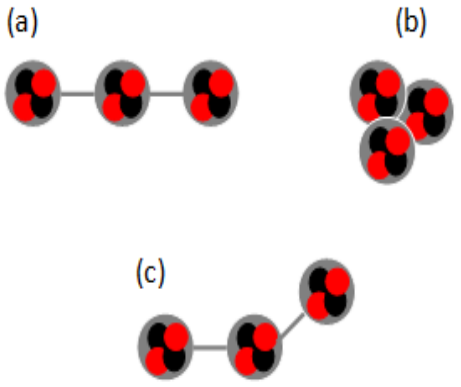

Figure 1.4: Different α-particle arrangements for the Hoyle state in ^{12}C as postulated by different α-cluster models, showing (*a*) a *linear chain*, (*b*) a dilute gas of bosonic α-particles, and (*c*) a "*bent-arm*" or obtuse triangular configuration.

- Another question regarding the structure of the Hoyle state involves the existence of the rotational excitation of the Hoyle state. After suggesting the linear arrangements of α-particles [17], Morinaga also conjectured that it should be possible for this structure to rotate *i.e.*, it should have energy levels with spin and parities $J^{\pi} = 2^{+}$, 4^{+}, 6^{+} *etc.*, built upon it, as shown in Fig. 1.5.

Ever since Morinaga predicted the existence of a rotational band of the Hoyle state there has been numerous investigations aimed at locating the 2^{+} exci-

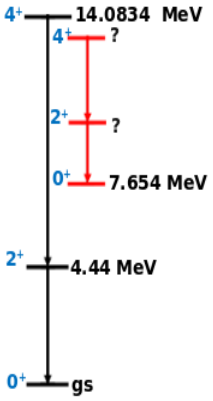

Figure 1.5: Simplified ^{12}C level scheme showing the ground state band up to the 4^+ state. Also shown is the postulated rotational band built upon the Hoyle state (red).

tation of the Hoyle state components both theoretically and experimentally. It is known that one of the key component in understanding the structural properties of the 0^+ state is finding the location of its collective 2^+ excitation.

Several cluster models have been used to predict the location of the 2^+ excitation of the Hoyle state. If the Hoyle state is assumed to be a state in which the α-particles are arranged in a linear chain (as postulated by Morinaga), its 2^+ excitation would lie at $\sim$0.8 MeV above the Hoyle state [22]. Assuming the dilute self-bound gas of bosonic α-particles, BEC calculations locate the 2^+ state at $\sim$1.3 MeV [19] above the Hoyle state. Finally, the FMD calculations [20] locate it at $\sim$2.3 MeV above the Hoyle state.

Experimentally, locating the 2^+ excitation of the Hoyle state has proved to be very difficult. Because of its expected well-developed cluster structure this state should be weakly populated in most reactions. The ^{12}C nucleus itself has proved to be difficult to study since above the α-decay threshold a a variety of states exist, some of which are very broad [23], thus making it difficult to resolve states that overlap. Regardless of these limiting factors, several experimental investigations have reported evidence of its existence using different probes. The first results date back to the work performed by Reynolds *et al.*

in 1970 [24]. They used the ^{11}B(^{3}He,d) reaction to measure the excitation energy spectrum of ^{12}C. In their measurement they claimed evidence of a state at E_x = 11.16 ± 0.05 MeV with a width of Γ = 550 ± 100 keV. From the angular distribution calculations they assigned spin and parity of 2^+ to this state, and they suggested it to be the 2^+ member of the α-cluster band based on the Hoyle state. In 2009, Freer *et al.* [25] reexamined the excited states of ^{12}C using the ^{12}C(^{12}C, 3α)^{12}C reaction at beam energies between 82 and 106 MeV. They also isolated the decays to both the ground state and the excited states of ^{8}Be. The also claimed to have observed the observed evidence for the 11.16 MeV state. However, neither of these findings could conclusively prove the existence of the 2^+ state, and therefore the 11.16 MeV state in ^{12}C is listed in the NNDC database with a question mark [23].

Recently, the search for the 2^+ excitation of the Hoyle state has attracted much attention. In 2004, Itoh *et al.* [26] analyzed cross-section data from the ^{12}C(α,α') inelastic α-particle scattering reaction with a 386 MeV α beam. With a Multipole Decomposition Analysis (MDA) they found evidence for a 2^+ state in the region E_x = 9 - 10 MeV. Such a state would be partially hidden by strong states in the excitation energy region of 9 - 11 MeV. These findings led to several investigations being undertaken to search for the 2^+ state in the E_x = 9 - 10 MeV region. High energy-resolution (p,p') data at beam energies of 66 and 200 MeV [27] acquired at iThemba LABS observed evidence of a broad state with a 2^+ character at E_x = 9.6 ± 1.0 MeV with a width of Γ = 600 ± 100 keV. This state would be hidden underneath the very strong 3^- state at 9.64 MeV. These results were also supported by work conducted by Zimmerman *et al.* [28], where the excited states of ^{12}C were populated using the (p,p') reaction at E_{lab} = 25 MeV. In 2011, Itoh *et al.* [29] presented a refined analysis of their ^{12}C(α,α') study, using both peak-fitting and MDA techniques. They concluded that a 2^+ state with a width of 1.01 ± 0.15 MeV exists at E_x = 9.84 ± 0.06 MeV. In 2012, Freer *et al.* [30] performed a consistent analysis of

the previously published inelastic proton and α scattering data [27, 29]. Both these datasets demonstrated the existence of a 2^+ state in ^{12}C at $E_x = 9.75 \pm 0.15$ MeV with width of $\Gamma = 750 \pm 150$ keV. The most recent identification of the 2^+ state is from the work by Zimmerman *et al.* [31]. They claim to have unambiguously identified a 2^+ state in ^{12}C at $E_x = 10.03 \pm 0.011$ MeV, with total width of $\Gamma = 800 \pm 130$ keV using the ^{12}C(γ,α_0)^{8}Be reaction. The work performed by Rana *et al.* [32] reported interesting features of the 2^+ state. They measured the ^{12}C excitation energy spectrum through inelastic scattering of α-particles from ^{12}C and found a 2^+ state at $E_x = 9.65 \pm 0.02$ with width of $\Gamma = 607 \pm 55$ keV. They reported that this newly found state decays into α-particles by first γ-decaying to the Hoyle state.

From the astrophysics point of view, the 2^+ excitation of the Hoyle state also plays a role in the nucleosynthesis process through helium burning at high temperatures, as experienced in type II supernova. At present the Nuclear Astrophysics Compilation of Reaction Rates (NACRE) [33], which is widely used in astrophysical calculations, locates such a state at $E_x = 9.1$ MeV. The accuracy of the calculated reaction rate depends on the accurate location of this state.

Motivation of this Work

Clearly there is disagreement regarding the exact location of the 2^+ excitation of the Hoyle state in the ^{12}C nucleus, in both the theoretical and experimental domains. Different cluster model theories locate the 2^+ excitation of the Hoyle state in different energy regions. Since cluster models presume the structure of the Hoyle state, positive identification of the 2^+ excitation could help in choosing the cluster model that best describe the structure of the Hoyle state. This can be a good starting point in the search for the Hoyle analogous states in other α-conjugate nuclei.

The majority of experimental investigations have found evidence of this state in the E_x = 9 - 10 MeV region [26, 27, 28, 29, 30, 31]. Table 1.1 shows the summary of the 2^+ states reported to exist around the 10 MeV excitation energy region. There is, however, still the 11.16 MeV state listed in the NNDC database to consider, which is indicated as a 2^+ state. Experimental investigations into the two distinct excitation energy regions is therefore required.

Reaction	E_x [MeV]	Γ [keV]	Ref.
^{12}C(p,p')	9.6 ± 0.01	600 ± 100	[27, 28]
^{12}C(α,α')	9.84 ± 0.06	1010 ± 150	[29]
^{12}C(p,p') & ^{12}C(α,α')	9.75 ± 0.15	750 ± 150	[30]
^{12}C(γ,α_0)^{8}Be	10.03 ± 0.011	800 ± 130	[31]
^{12}C(α,α')	9.65 ± 0.02	607 ± 55	[32]

Table 1.1: Summary of the 2^+ states reported to exist around the 10 MeV excitation energy region.

The work presented in this thesis is twofold. The first part involves the investigation of the existence of the 11.16 MeV state in ^{12}C. This state was first observed in the measurement reported in Ref. [24], with Ref. [25] also claiming to have found evidence of its existence. In the work conducted by Gai *et al.* [34] using the ^{12}C(γ,3α) reaction, they explicitly stated that no evidence of a state at 11.16 MeV was found. In 2010, Kirsebom *et al.* [35] used the ^{11}B(^{3}He,d) reaction at an incident energy of 8.5 MeV to investigate ^{12}C breakup into three α-particles, and no strength for a state at 11.16 MeV was reported. Even though no other investigations have successfully seen the evidence of this state, the question remains whether the 11.16 state is populated in this specific reaction. The only way to provide firm answers regarding its existence is to repeat the measurement performed in Ref. [24]. Thus, this experiment will be reconsidered in the work presented in this thesis by studying the excitation energy spectrum of ^{12}C using the ^{11}B(^{3}He,d) reaction. The measurement was

performed in September 2011 at iThemba LABS, South Africa, at an incident beam energy of $E_{lab} = 44$ MeV, as in the case of the original measurements [24].

The second part of this work focuses on providing further proof of the existence of the 2^+ excitation of the Hoyle state in the $E_x = 9$ - 10 MeV region in ^{12}C. To complete this investigation a complete kinematics measurement study using the ^{14}C$(p,t)^{12}$C$[3\alpha]$ reaction was performed. This measurement was performed at iThemba LABS with a proton beam energy of $E_{lab} = 66$ MeV during October 2012.

Outline

A brief overview of theoretical cluster models developed over the years is given in Chapter 2. Chapter 3 elaborates on the experimental equipment used as well as the experimental methods followed. Data analysis of the ^{11}B$(^3$He$,d)^{12}$C and ^{14}C$(p,t)^{12}$C measurements are respectively given in Chapters 4 and 5. Chapter 6 briefly discusses the theoretical formalism used in interpreting the data. The results are presented in Chapter 7, followed by conclusions and outlook in Chapter 8.

Chapter 2

Theoretical Cluster Models

Despite the success of the nuclear shell model in describing the structure of heavy nuclei, it has been unable to reproduce a number of the low-lying states in light nuclei. As an example, no core shell model calculations fail to reproduce the energy of the Hoyle state in ^{12}C. The failure is usually related to the fact that at this excitation energy region, the structure of the ^{12}C nucleus shifts from the usual shell model picture to the well-developed cluster structure i.e. the nucleus can be described as a composite of different clusters of nucleons. To describe the low-lying states in light nuclei, several clustering theories have been developed. This chapter gives an overview of some of the models developed over the years to study nuclear clustering. Their applications to the study of α-conjugate nuclei are also briefly emphasized.

2.1 Bloch-Brink Alpha Clustering Model

Brink's α-clustering model was introduced during the early stage of clustering considerations [36]. In the Bloch-Brink model, the α-conjugate nucleus is described in terms of N single-particle wave functions, ψ_k. The wave function characterizes the motion of a single nucleon in a 1s harmonic oscillator orbit centered at the point R_k corresponding to the mean position of the center-of-

mass of the k^{th} α-particle [37]:

$$\psi_k = A\ exp\ \left[\frac{-(r-R_k)^2}{2b^2}\right]\ , \tag{2.1}$$

where k runs from 1 to N. The constant A is given by

$$A = \sqrt{\frac{1}{b^3\pi^{\frac{3}{2}}}}\ , \tag{2.2}$$

where b is the harmonic oscillator radius parameter which determines the size of the α-particles. The total wave function is constructed by requiring that each single-particle state should be occupied by an α-particle, thus leading to the $N\alpha$ wave function created using a normalized Slater determinant:

$$\Phi\left(R_1, R_2, ..., R_N\right) = B\mathcal{C}\prod_{k=1}^{N}\psi_k(R)\ , \tag{2.3}$$

where $\mathcal{C}\prod_{k=1}^{N}\psi_k$ is the Slater determinant wave function, $\mathcal{C}$ is an antisymmetrization operator and B is the normalization constant defined in Ref. [37].

This model has been used to calculate the geometrical arrangements and energies of α-chain states in α-conjugate nuclei [22], and especially in ^{12}C [38].

2.2 The Generator Coordinate Method (GCM)

The generator coordinate method (GCM) is the method where the $\alpha + {}^8$Be system is solved with the three-cluster model. To do this, the $\alpha + {}^8$Be system is described by a three-α-particle configuration. This description leads to the introduction of two generator coordinates, one internal to the ^{8}Be nucleus and the other associated with the $\alpha + {}^8$Be relative motion [39].

To use the GCM, the translation-invariant α-particle wave function ϕ_j (where j is the cluster index) constructed in the harmonic oscillator model is considered. The basis function for the 12 nucleon system is given by [39],

$$\Phi(R_1, R_2) = \phi_{c.m.}\mathcal{A}\phi_1\phi_2\phi_3\Gamma(b_1, \rho, R_1)\Gamma(b_2, \rho^{'}, R_2)\ , \tag{2.4}$$

where $\mathcal{A}$ is the antisymmetrization projector, R_1 and R_2 are the generator coordinates, and parameters b_1, b_2, ρ, and $\rho^{'}$ are defined in Ref. [39]. The total wave function of the system is defined by [39]:

$$\Psi^{JM\pi} = \sum_{lL} f_{lL}^{J\pi}(R_1, R_2)\Phi_{lL}^{JM\pi}(R_1, R_2)dR_1dR_2 \ , \tag{2.5}$$

where J is the total angular momentum (M is its projection), L and l are respectively, the orbital momentum and relative orbital momentum of ^{8}Be nucleus, and $\pi = (\text{-}1)^{l+L}$ is the parity. The function $f_{lL}^{J\pi}$ is called the generator function. For ^{12}C bound state wave functions, the coefficients $f_{lL}^{J\pi}$ are deduced from the variational principle. For α + ^{8}Be scattering wave functions, the coefficients are calculated from the R-matrix method.

This method has been used in Ref. [39] to study the ^{8}Be(α,γ)^{12}C reaction in order to model the triple-α reaction, which leads to production of ^{12}C in stars and to calculate the location of the 2_2^+ state in ^{12}C.

2.3 Antisymmetrized Molecular Dynamics (AMD)

The antisymmetrized molecular dynamics (AMD) theory applies to studies of the nuclear structure and the nuclear reaction. It was introduced by Ono *et al.* who developed this method for the study of nuclear reactions [40, 41]. To study the nuclear structure, the AMD framework was extended by Kanada-En$^{'}$yo [42, 43]. In the AMD framework, basis wave functions of the system are given by the Slater determinants. The wave function of the AMD theory is flexible as the nuclear structure can be studied with no need to assume any inert core or cluster. This makes the AMD applicable in studying various cluster structures as well as shell-model-like structures.

In the AMD framework, the wave function of a system is written as a linear

combination of AMD wave functions [44],

$$\Phi = b\Phi_{AMD} + b^{'}\Phi^{'}_{AMD}\cdots \quad . \tag{2.6}$$

An AMD wave function is a Slater determinant of Gaussian wave packets;

$$\Phi_{AMD}(Z) = \frac{1}{\sqrt{A!}}\mathcal{B}\{\psi_1, \psi_2, ..., \psi_A\} \ , \tag{2.7}$$

where ψ_j are the Gaussian wave packets as defined in Ref. [44].

The AMD theory was used by Kanada-En$^{'}$yo [45] to study the structure of the ground and excited states of the ^{12}C nucleus. They employed variational calculations after spin-parity projection in the framework of AMD for the purpose of comparison with the available experimental data. It was found that the calculations systematically reproduce various experimental data, as illustrated in Fig. 2.1 [45].

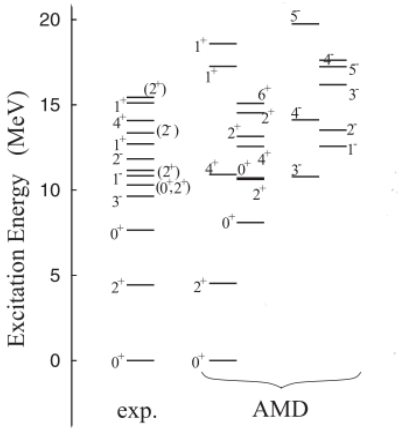

Figure 2.1: Energy levels of the ground and excited states of ^{12}C as obtained from AMD calculations from Ref. [45].

2.4 Fermionic Molecular Dynamics (FMD)

Recently there has been suggestions that the Hoyle state is a dilute self-bound gas of α-particles. To clarify these these suggestions, model such as the fermionic molecular dynamics (FMD) model has been used to investigate

the structural properties of the Hoyle state [46]. FMD is a microscopic and unified approach to both nuclear structure and nuclear reactions. It is similar to AMD but it uses the degrees of freedom of the individual nucleons, such as the centre-of-mass positions, spins and isospins as the fundamental degrees of freedom of the system and uses a fully antisymmetrized wave function to describe the many-body problem. It also includes the tensor force in the interaction. As in AMD, the FMD wave fucntions can describe cluster states as well a shell-model-like configurations.

Recently, the interest in FMD calculations has been growing since they can be used to model cluster states. In Ref. [20], FMD was used to study the structure of the Hoyle state. The FMD results showed that the relative positions of the clusters are correlated, mostly resembling ^{8}Be + α configurations, which suggests that the interpretation of the Hoyle state as being similar to Bose-Einstein condensate must not be taken literally. Using FMD the location of the 2_2^+ state in ^{12}C was also predicted, as shown in Table 2.1.

	Experiment [MeV]	FMD [MeV]	α-cluster [MeV]	BEC [MeV]
$E_x(0_2^+)$	7.654	9.50	7.89	7.73
$E_x(0_3^+)$	(10.3)	11.90	10.33	?
$E_x(2_1^+)$	4.44	5.31	2.56	2.81
$E_x(2_2^+)$	(11.16)	11.83	9.21	9.03

Table 2.1: Excitation energy of ^{12}C for experimental data from Ref. [23] and as predicted by the FMD model [20], α-cluster model and BEC [19].

2.5 Bose-Einstein Condensation (BEC) Model

In 2001, Tohsaki *et al.* [18] proposed a new α-cluster wave function which is of the α-particle condensate type. This wave function was aimed at treating α-cluster states near the α-particle threshold as a dilute self-bound gas of

bosonic α-particles, hence this particular theory is referred to as the Bose-Einstein condensate (BEC) model.

The $N\alpha$ total wave function describing an α-particle Bose condensed state can be written as [18]:

$$\langle \mathbf{r}_1\sigma_1\tau_1.....\mathbf{r}_{4n}\sigma_{4n}\tau_{4n}|\Phi_{n\alpha}\rangle \propto \mathcal{A}\{e^{-\frac{2}{B^2}(\mathbf{X}_1^2+....+\mathbf{X}_n^2)}\phi(\alpha_1)....\phi(\alpha_n)\} \ , \tag{2.8}$$

where B and $\mathbf{X}_i$ are the center-of-mass coordinates of the i^{th} α-cluster α_i, σ_i and τ_i represent the nucleon's spin-isospin at the spatial point $\mathbf{r}$, and $\mathcal{A}$ is the antisymmetrization operator. The internal wave function $\phi(\alpha_i)$, of the α-cluster α_i is defined as

$$\phi(\alpha_i) \propto e^{-\frac{1}{8b^2}} \sum_{m>n}^{4} (\mathbf{r}_{im} - \mathbf{r}_{in})^2. \tag{2.9}$$

The wave function in Eq. (2.8) expresses the state where $n\alpha$ clusters occupy the same $0s$ harmonic oscillator orbit.

In 2003, Funaki *et al.* showed in Ref. [19] that the Hoyle state wave function obtained by solving the full three-body problem of the microscopic 3α-cluster model, is almost completely equivalent to the wave function of the 3α condensed state given by in Eq. (2.8). The results obtained in predicting excitation energy of ^{12}C nucleus are shown in Table 2.1.

2.6 Summary

In terms of describing the Hoyle state, all these models arrive at the same conclusion, namely that the Hoyle state might have a strongly developed cluster structure. This is interesting since the models such as the AMD and the FMD do not make any clustering assumptions but are still able to successfully describe some observed characteristics of the Hoyle state. These models however, predict different geometric arrangements of α-particles. As already stated in Chapter 1, in order to experimentally investigate how the α-particles

are arranged an understanding of the excitation of the Hoyle state is required. Therefore, positively identifying the location of the 2^+ excitation of the Hoyle state will help in both understanding the structure of the Hoyle state and also in the development of the various models used to describe cluster states.

Chapter 3

Experiment

This study was aimed at investigating two candidates for the 2^+ state based on the Hoyle state configuration in ^{12}C. The first candidate is located at an excitation energy E_x = 11.16 MeV, and was supposedly observed in a measurement performed by Reynolds *et al.* [24], using the ^{11}B(^{3}He,d)^{12}C reaction at E_{lab} = 44 MeV. They postulated it to be the 2^+ state built on the Hoyle state. The second candidate was reported repeatedly in recent investigations in the excitation energy region 9 - 10 MeV, and requires further characterization. Two experiments were performed as part of this investigation. The first was the ^{11}B(^{3}He,d)^{12}C measurement which was aimed at providing firm answers regarding the existence of the 11.16 MeV state. It was performed in September 2011 using the high energy resolution K600 magnetic spectrometer. The second was the ^{14}C(p,t)^{12}C complete kinematics measurement performed in October 2012. In the ^{14}C(p,t)^{12}C[α] measurement the tritons were detected in coincidence with α-particles from the decay of the recoiling ^{12}C, using the K600 magnetic spectrometer and silicon detectors. Both experiments were conducted at the iThemba Laboratory for Accelerator Based Sciences (iThemba LABS).

The experimental setups used in these two measurements are discussed in this chapter. In section 3.1 the iThemba LABS facility is discussed. Section

3.2 briefly introduces the target chamber, while the spectrometer and its focal plane detectors are discussed in sections 3.3 and 3.4 respectively. Section 3.5 describes additional equipment used in the second part of this study. The electronic setup, brief discussion of targets used and experimental procedures for both experiments are discussed in sections 3.6, 3.7 and 3.8 respectively.

3.1 The iThemba LABS Facility

The measurements presented in this thesis were performed at iThemba LABS, a multidisciplinary facility situated in the Western Cape, South Africa. This facility provides accelerator-based particle beams which are mainly used for radio-isotope production, proton and neutron therapy, radiation biophysics, and basic research. The basic research conducted at this facility covers topics in nuclear and material sciences. The cornerstone of the facility is the Separated Sector Cyclotron (SSC) accelerator.

Figure 3.1 shows the floor layout of the cyclotron facility. Beams of light or heavy ions are pre-accelerated with one of the two Solid Pole injector Cyclotrons (SPC1 and SPC2)[1] until they reach an energy high enough to be delivered to the SSC. When the intended energy is reached, the beam is steered through the J or K beam line (depending on which injector cyclotron is being used) and injected into the SSC where it is accelerated to the desired final energy. From the SSC the beams are steered along different beam lines and can be delivered to different experimental facilities. For the experiments discussed in this study the beams were delivered to the spectrometer vault through the X, P and S beam lines.

Two different beams were used in the measurements reported in this study. For the (^{3}He,d) measurement a 44 MeV ^{3}He beam was used. The SPC2 injector cyclotron was used to produce the beam with beam intensities between 5 pnA

[1]SPC1 is uniquely used for light ions while the SPC2 is used for both light and heavy ions.

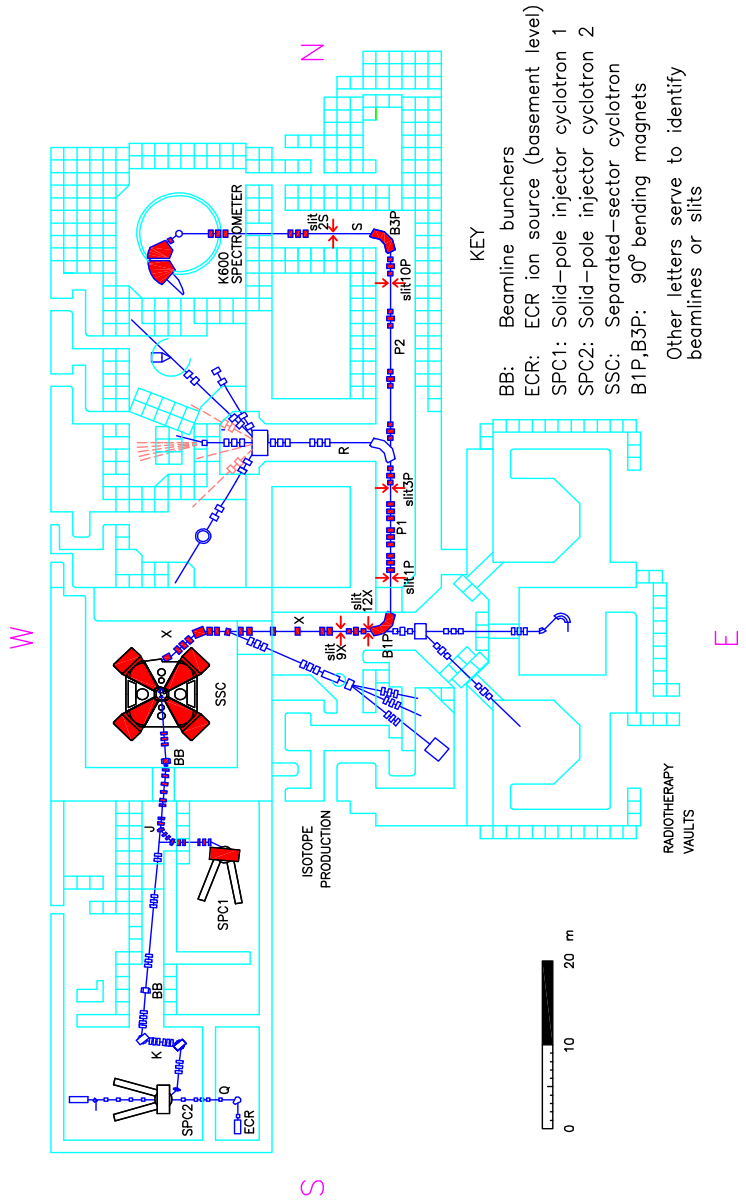

Figure 3.1: The layout of the Separated Sector Cyclotron facility of iThemba LABS.

to 50 pnA. For complete kinematics measurement using the ^{14}C(p,t)^{12}C[3α] reaction a 66 MeV proton beam was used. Unlike the ^{3}He beam, the proton beam was produced using the SPC1 injector with intensities between 10 nA to 100 nA.

3.2 Scattering Chamber

The scattering chamber, also known as the target chamber, connects the end of the S beamline to the entrance of the K600 magnetic spectrometer, and shown in Fig. 3.2. The scattering chamber has a diameter of 524 mm, and is situated at the turning axis of the spectrometer. It houses the target ladder in which a maximum of six targets can be mounted (illustrated in Fig. 3.2(a)), as well as a turntable on which an internal beamstop or detectors can be mounted, depending on the experimental setup of interest. The complete kinematics measurement involved a setup in which an array of silicon detectors were mounted inside the scattering chamber as seen in Fig. 3.2(b). Due to space requirements the removal of the turntable was necessary. A description of the silicon array setup will be discussed later in this chapter.

3.3 K600 Magnetic Spectrometer

The K600 magnetic spectrometer at iThemba LABS is a QDD (quadrupole dipole dipole) magnetic spectrometer, as shown in Fig. 3.3. It has an energy constant, K, equal to 600, and can therefore be used to measure protons up to 600 MeV, or tritons up to 200 MeV. There are five active magnetic elements, namely two dipoles, the quadrupole, and two trim coils (K and H). The two dipole magnets, D1 and D2, allow the momentum dispersion to be varied by varying the ratio of the fields of the two dipole magnets. The quadrupole Q, is used to focus the scattered particles vertically in the focal plane. The K-coil

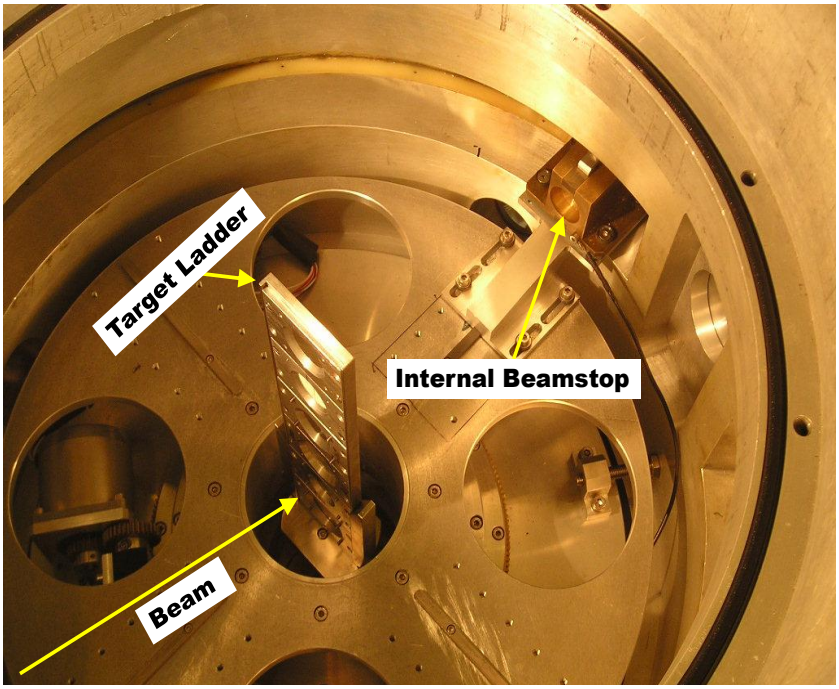

(a)

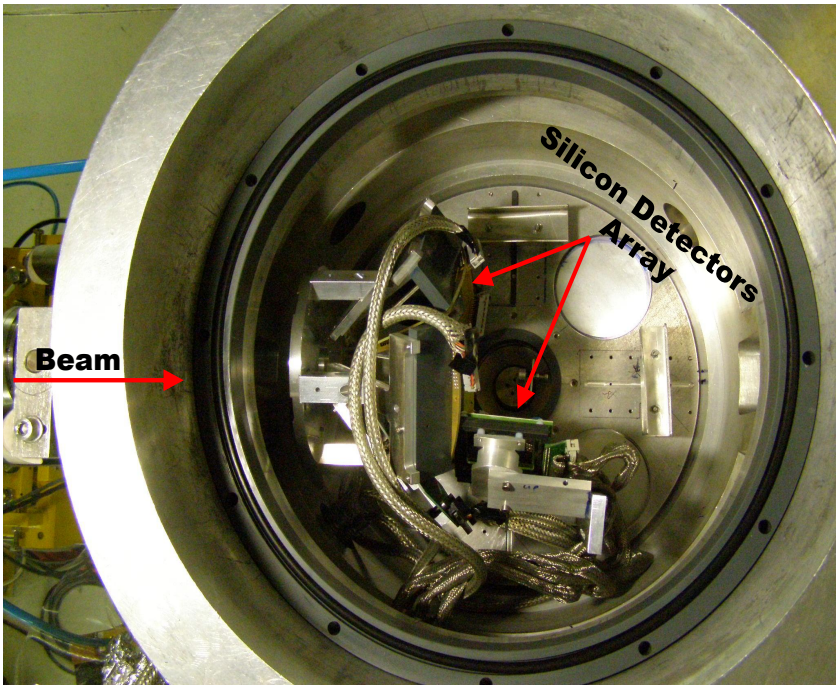

(b)

Figure 3.2: The scattering chamber as used for the two measurements: (a) indicates the target ladder and internal beamstop. (b) shows the placement of the silicon detector array used in the (p,t) measurement.

is a pole face current winding which introduces both a dipole and quadrupole component. It is used to adjust for the first order kinematic variation of the momentum with angle $(x|\theta)$. The H-coil is a pole face current winding that introduces both a dipole and sextupole component, and it is used to correct for $(x|\theta^2)$ aberrations. More detailed specifications on the performance of the K600 magnetic spectrometer can be found in Ref. [47].

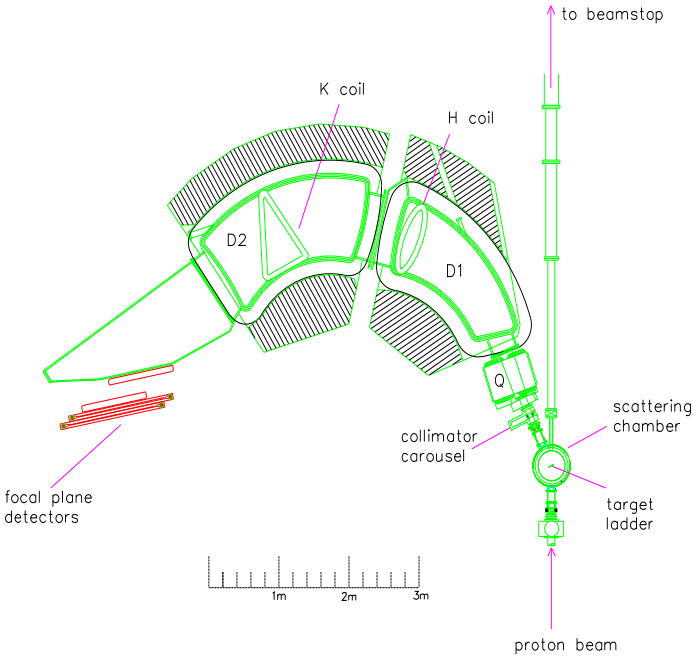

Figure 3.3: A schematic overview of the K600 magnetic spectrometer. Shown also in the figure is the beam pipe used to deliver the non-interacted beam to the beamstop.

A collimator carousel is positioned in front of the quadrupole. The carousel houses six collimators. Behind the second dipole is the focal plane position sensitive detector package. The focal plane detectors can be positioned in one of three dispersion mode positions, to allow measurement in the low, medium or high dispersion modes. For the present measurements the medium dispersion mode was used.

There exist several different beamstop configurations that can be used depending on the angle at which the spectrometer is positioned and the type

of experiment one needs to perform [47]. For the measurements reported in this study an external beamstop/Faraday cup was used. This well shielded Faraday cup is positioned in the concrete wall of the experimental area. It is used for measurements with $\theta_{lab} \geq 21°$. The beam line to the Faraday cup can be seen in Fig. 3.3.

3.4 Focal-Plane Detector Package

As mentioned in the preceding section, the focal plane of the K600 magnetic spectrometer is situated behind the second dipole magnet. The detector system located in the focal plane, as shown in Fig. 3.4, is used for the detection of charged particles. It consists of a pair of drift chambers for position and angle measurements, and plastic scintillation detectors behind the drift chambers for particle identification and fast trigger purposes.

3.4.1 The Original Focal-Plane Detector Package

Until recently, the available position sensitive focal plane detectors consisted solely of three multi-wire drift chambers (MWDC). Two different geometric configurations of these drift chambers are available, namely the vertical drift chamber (VDC) and the horizontal drift chamber (HDC)[2]. The VDCs were used in both measurements reported here to determine the position information along the length of the focal plane, as well as the horizontal angle at which the charged particle traverses the focal plane.

The VDCs were designed and developed at iThemba LABS and they have been in operation since the early 1990's. They consist of two 20 μm thick Al cathode planes placed 16 mm apart. Midway between them lies the signal wire anode plane. To isolate the interior of the VDC from atmosphere, Mylar

[2]The terms VDC and HDC do not relate to the physical orientation of the signal wires, but rather to the fact that in the VDC the main drift direction of electrons is perpendicular to the signal wire plane. In the HDC the electrons drift in the plane of the signal wires.

planes which are 25 μm thick are placed on both sides of the VDC. The volume between the two cathode planes is filled with a gas mixture of 90% Ar 10% CO_2. The signal wire plane consists of 198 signal wires and 199 guard wires (also known as field shaping wires). The signal wires are 20 μm in diameter, spaced 4 mm apart, and made of gold-plated tungsten. The guard wires are interspersed between adjacent signal wires and are 50 μm in diameter, spaced 4 mm apart, and also made of gold-plated tungsten. The main property of guard wires is to provide field shaping around the signal wires. They also define the drift cells associated with each signal wire. The electron drift velocity in the VDCs are of order of 40 - 60 mm/μs section. The 8 mm distance between the cathode and signal wires therefore corresponds to drift times of 133 - 200 ns.

3.4.2 The New Focal-Plane Detector Package

With the development of the zero degree capability of the K600 magnetic spectrometer, there was a need to improve the detection capabilities. To enhance the vertical position resolution, new VDCs were developed at iThemba LABS and have been in operation since 2009. They consist of two wire planes each. In order to determine the angle at which the particles traverse the focal plane, each VDC can accurately determine both the horizontal as well as vertical components of particle tracks in the focal plane. They can operate in both the medium and high dispersion focal planes. One of the new VDCs, in combination with one original VDC, was used for the (^{3}He,d) measurement to allow for possible background identification that has a different y-character than the physics events.

The new drift chambers consist of three high voltage 20 μm thick aluminium cathode planes, separated by 16 mm each. In between them are two anode signal wire planes. The same gas used for the old VDCs is still used to fill the volume between the cathode planes. The two wire planes are referred to as the X wire plane and U wire plane respectively. The wire configuration in the

X wire plane is perpendicular to the scattering plane while in the U wire plane wires are angled 50° with respect to the scattering plane. As in the case of the old VDCs, the new VDC X wire-plane consists of 198 gold-plated tungsten signal-wires, 20 μm in diameter, spaced 4 mm apart. Between the adjacent wires at equal distances are 199 guard wires made of 50 μm diameter gold-plated tungsten. The U wire plane consist of 143 signal wires and 144 guard wires, also spaced 4 mm apart. The typical intrinsic horizontal position and vertical position resolution experienced in the (^{3}He,d) measurement was 0.08 mm and 0.09 mm respectively, which represent the FWHM values calculated using the method in Ref. [49]. The horizontal position resolution in the (p,t) measurement was 0.05 mm (FWHM).

3.4.3 Paddle Scintillation

The detectors used for particle identification and fast timing triggering are the plastic scintillation detectors. They were assembled at iThemba LABS and have been in operation since the early 90's. They were built using BC-408 plastic scintillation material manufactured by Bicron (now Saint Gobain Crystals) [50]. The choice of BC-408, suitable for detecting charged particles, follows from the very short response times, and their principal application is for very short time-of-flight (TOF) measurements [50]. This is one of the requirements in K600 magnetic spectrometer measurements. Because of their geometrical configuration, the plastic scintillators at iThemba LABS are referred to as paddles. They have a surface area of 48" $\times$ 4" and are a fraction of an inch thick. Two of the scintillation detectors available for use are visible in the focal plane detection package shown in Fig. 3.4.

Three scintillation detectors of different thickness are available for use, namely $\frac{1}{8}$", $\frac{1}{4}$" and $\frac{1}{2}$" thick scintillators. The choice of thickness used is based on the energy at which the charged particles leaves the target. If the energy of charged particles is high enough for them to pass through the VDCs and reach

the first paddle with high enough energy to go through it, a second paddle can be used as an E detector. If two paddles are used (which is normally the case), paddle coincidence timing is used for triggering and the particle identification can be achieved through ΔE-E spectra as was the case in Ref [48].

For measurements discussed in this study, energy loss calculations showed that particles of interests (deuterons and tritons) do not have enough energy to exit the first paddle regardless of the thickness. Hence only one $\frac{1}{4}$" paddle was used for triggering purposes, and spectra of deposited energy in the paddle versus TOF were used for particle identification, as shown in Chapters 4 and 5.

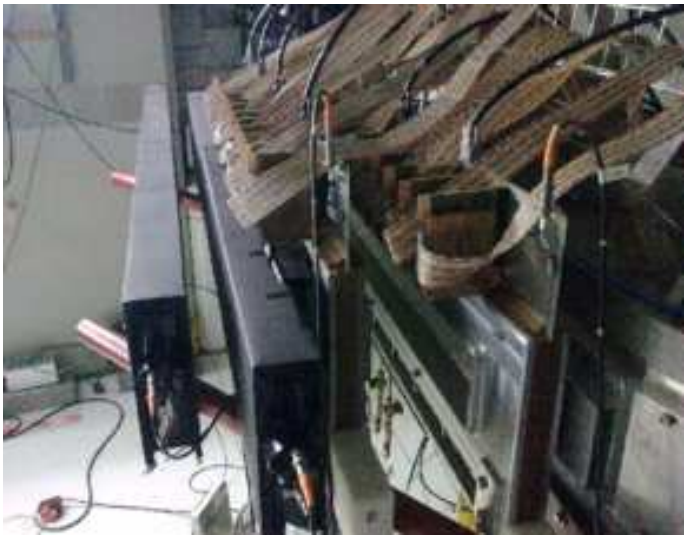

Figure 3.4: The focal plane detector package of the K600 magnetic spectrometer. Two drift chambers and two scintillators are shown.

3.5 Silicon Detectors

Recently, several coincident measurements have been successfully performed using the K600 magnetic spectrometer. For these measurements, the detection capabilities of the spectrometer was extended by including charged particle detectors (e.g. silicon detectors) as well as γ-ray detectors (e.g. HPGe detectors).

For the coincidence measurement performed in this study, an array of silicon detectors was used. The array (see Fig. 3.5) was placed inside the scattering chamber and was used to detect α-particles from the decay of unbound states in ^{12}C excited with the ^{14}C$(p,t)^{12}$C$^{*}[3\alpha]$ reaction. These α-particles were detected in coincidence with tritons observed in the focal plane of the K600 spectrometer.

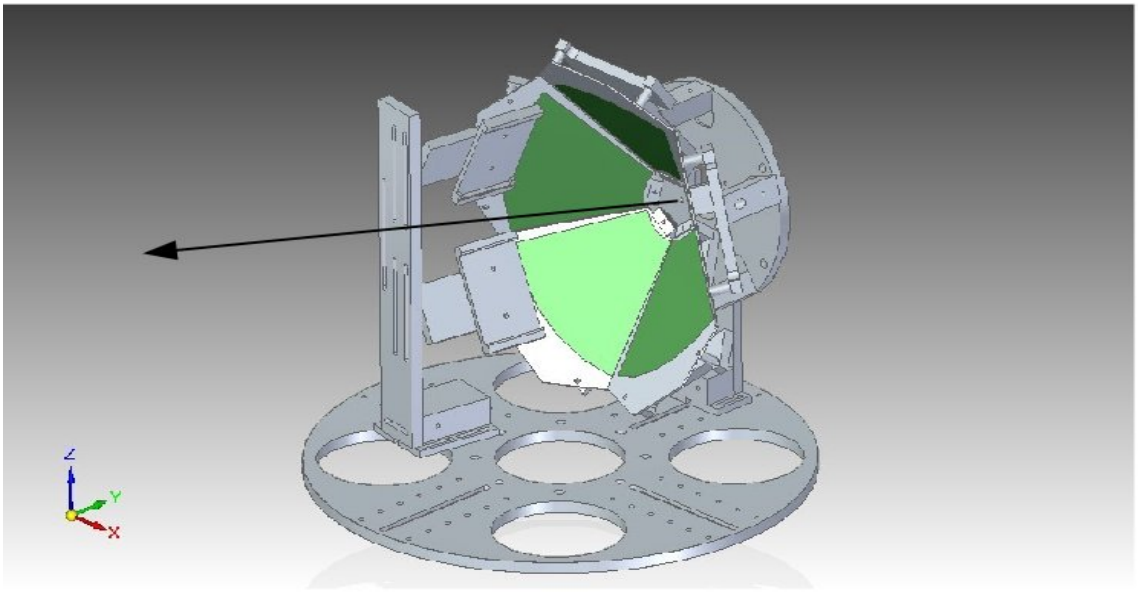

Figure 3.5: Schematic overview of the array of silicon detectors used for a complete kinematics measurement of the decay of the ^{12}C nucleus. Only the mounting plates of the DSSSD silicon detectors are shown. The arrow indictates the direction of the beam.

The array of silicon detectors consisted of two W1 Double-Sided Silicon Strip Detectors (DSSSDs), three YY1 wedge shaped silicon strip detectors (also referred to as the wedge detectors) and one MMM DSSSD 60° wedge detector (also referred to as the TIARA detector), all manufactured by Micron Semiconductor. The W1 detectors used are 300 μm thick, covering an area of (50×50) mm^2. They are double-sided, each side with 16 strips that are 3 mm wide and 50 mm long, as shown in Fig. 3.6(a). Wedge detectors are 1000 μm thick, single-sided consisting of 16 curved strips (rings) each 5 mm wide, while

the TIARA detector is 400 μm thick, double-sided with 16 curved strips each 5 mm wide on the front junction side, and 8 sectors rear ohmic side. These detectors are shown in Figs. 3.6(b).

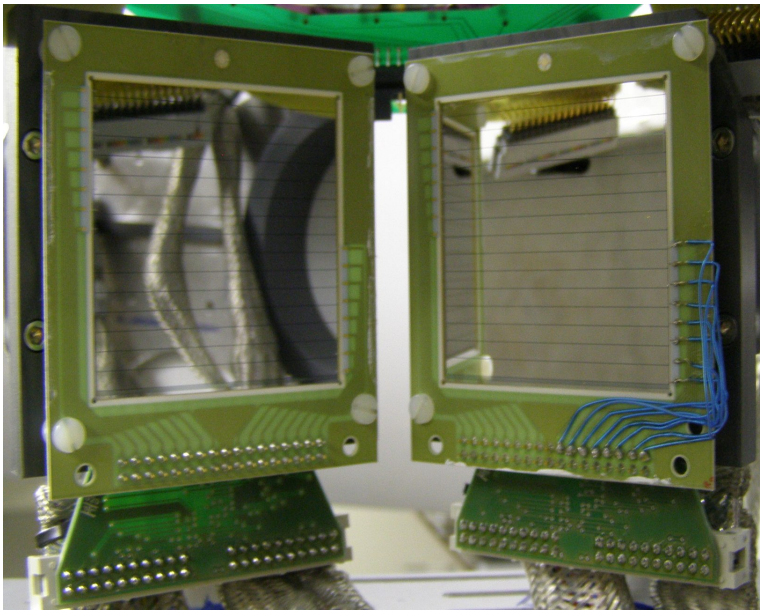

(a)

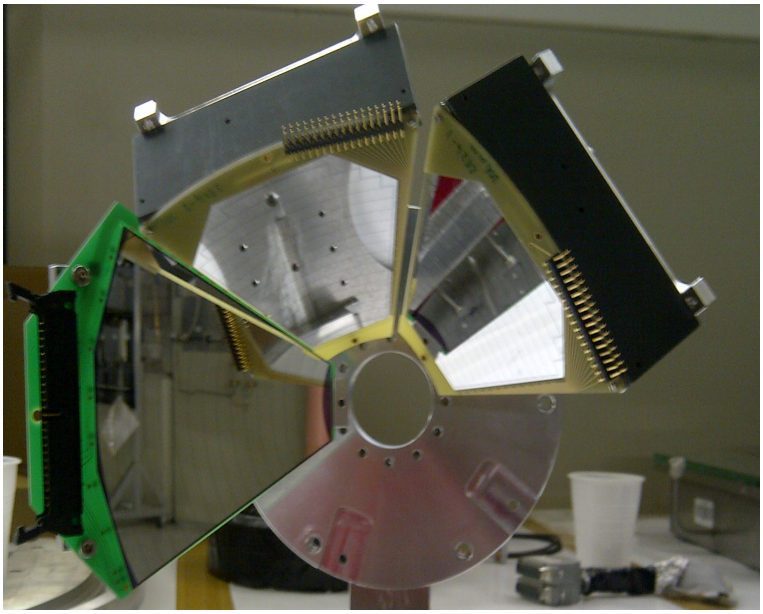

(b)

Figure 3.6: Silicon detectors used in assembling an array for coincident measurement: (a) two W1 DSSSDs and (b) one TIARA and two wedge detectors.

These three different types of silicon detectors were positioned in the array as follows: the wedge detectors and a single TIARA detector were placed at backward angles in a geometry that resembles a lampshade, shown in Figs. 3.5 and 3.7. The lampshade configuration was chosen in order to cover a large angular range: $115^\circ \leq \theta_{lab} \leq 170^\circ$. The lampshade was put upstream of the target ladder since the results from kinematic calculations showed that at the spectrometer angle of $\theta_{lab} = 21^\circ$ the ^{12}C nucleus leaves the target at backwards angles. Hence the α-particles from decaying ^{12}C excited states can be measured at backwards angles. The distance between the center of the lampshade and target was 100 mm. The TIARA was positioned in such a way that the 16 strips were situated in the front, facing the target, while the 8 sectors were situated on the back side of the detector.

In order to increase the angular coverage even further, the two W1 detectors were added to the array. The distance from the middle strip to the center of the target was 80 mm, and they were centered at $\theta = 100^\circ$ and ϕ angles of 45° and 315° respectively. The vertical strips were on the front face of the detector, while the horizontal strips were on the back side of the detector. This arrangement resulted in 256 pixels, each acting as an individual detector.

3.6 Electronics and Data Acquisition System

The data acquisition (DAQ) system of the K600 consists of electronics according to the Nuclear Instrumentation Module (NIM) and Versa Module Europe (VME) standards. The modules are used to convert the electronic signals from the detectors into digital data which can be processed by the Maximum Integrated Data Acquisition System (MIDAS) computer software which was developed at the Paul Scherrer Institute (PSI) and TRIUMF [51, 52]. The NIM electronics for the K600 trigger as well as all VME electronics were on

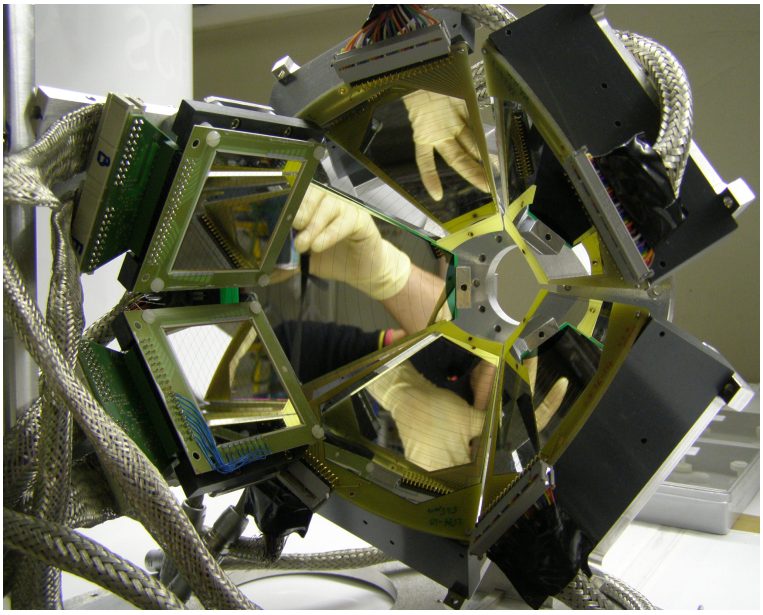

Figure 3.7: The assembled array of silicon detectors used for coincidence measurements before it was placed inside the scattering chamber.

the K600 platform, while NIM electronics for the silicon detectors were housed in a separate electronics tower close to the scattering chamber.

Figure 3.8 provides an overview of the trigger electronics for the K600. The signal processing works as follows: when a charged particle enters the paddle, light is generated and transmitted to both ends of the paddle and collected by photomultiplier tubes (PMT's). Time information of the signals from the PMT's is extracted using constant-fraction discriminators (CFD) and sent to a mean-timer. The mean-timer generates the signal of a mean arrival time of the two input signals. This signal is then used as a time reference and trigger signal in all the Time-to-Digital Converter (TDC) units, and also initiates the DAQ readout through the CAEN model V792 QDC gate signal. It is also used as a start for TOF measurements, while the signal from the cyclotron's RF serves as a stop signal. The TDC digitizes the time difference between the trigger signal and the RF signal. The TDC's in use in the K600 magnetic spectrometer DAQ are the 128 channel CAEN model V1190A TDC [53].

When the particle traverses the drift chambers, signal wires conduct the in-

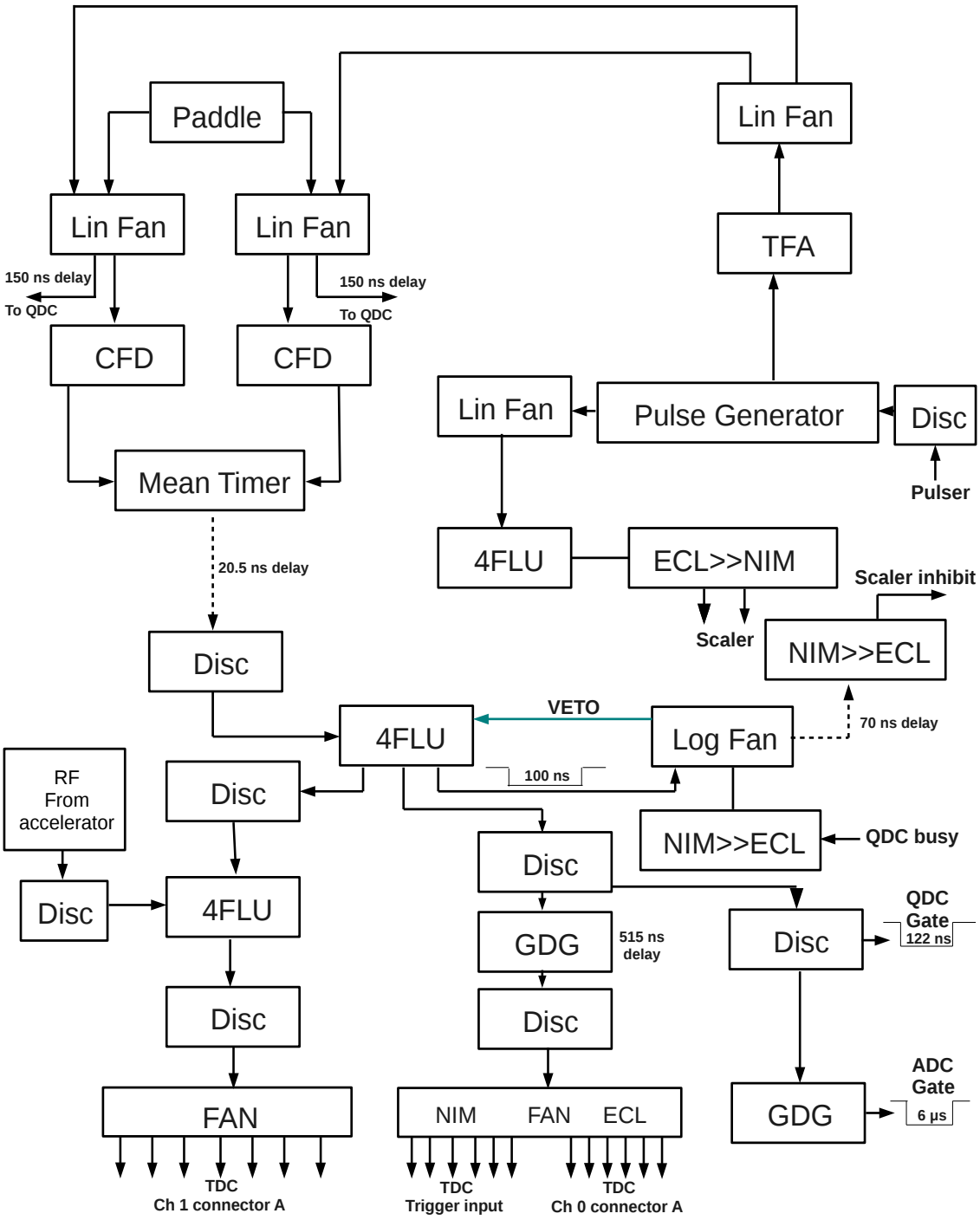

Figure 3.8: Schematic of the timing electronics used for the K600 magnetic spectrometer trigger.

duced signals to Technoland preamplifiers for amplification and discrimination. The amplified signals are transported to the TDCs using 34-way twisted-pair ribbon cables. A total of 7 TDC modules are used in order to accommodate all VDC wire signals. The time difference between signals from the signal wires and delayed trigger signals from the paddle is used in the process of determining drift times.

Figure 3.9 shows how the signals from the silicon detectors were processed in the ^{14}C(p,t) measurement. When the particle hits the silicon detector the signal is produced and sent to the preamplifiers for amplifications. Mesytec model MPR 32-channel preamplifiers were used in processing the silicon detectors signals. These preamplifiers provide very fast recovery from large signals and precise spectroscopy of very small signals. They were specifically developed for reading out silicon strip detectors [54].

These preamplifiers were placed just outside the scattering chamber to be in close proximity to the detector in order to reduce the capacitance of the input connections and noise pick-up. The 19 pin LEMO vacuum feedthroughs (LEMO SGJ.2B.319.CLLSV) were used to connect cables from the silicon detectors to the preamplifiers. From the preamplifiers, the signal was sent to CAEN model N568B 16-channel spectroscopy amplifiers using ribbon cables. In the amplifiers, signals are split into two types of signals, namely fast output signals, which are used to extract time information of the signal, and slow signals (also known as the spectroscopy signal) used for energy determination. The fast signals were passed through discriminators where the signal above the threshold was passed on to the TDCs. The slow spectroscopy signal was sent to the CAEN model V785 Analog-to-Digital Converters (ADC) VME module where the pulse height was digitized. Ribbon cables were used for transportation of signals to the TDCs and ADCs. The triggering for the coincidence measurement was such that the silicon detectors were operated in a slave mode and the K600 was used as the master trigger. This means that

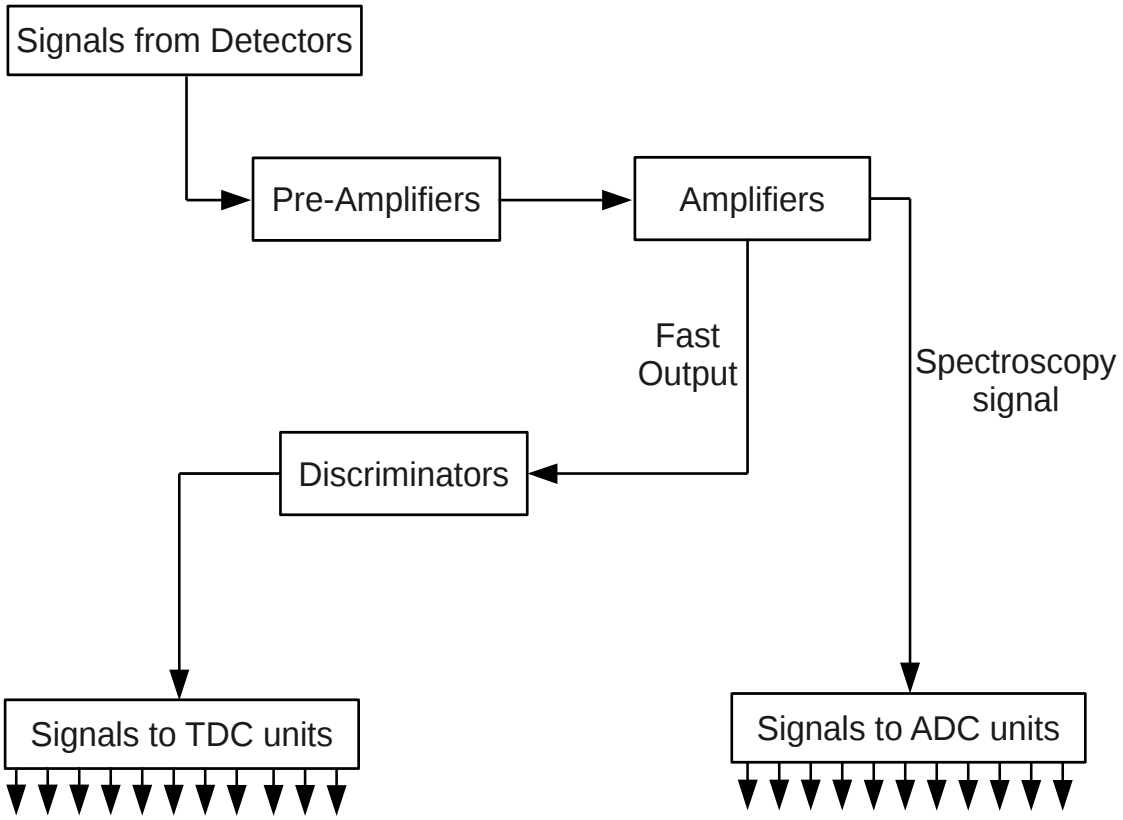

Figure 3.9: Schematic of the electronics chain used for the silicon detectors.

for each event recorded by the K600, the maximum pulse height within a 6 μs ADC time window was digitized for all ADC channels, yielding both K600 only and K600 events in coincidence with silicon detectors events.

The silicon detectors were biased using the NHQ 202M FAST ComTec High Voltage power supplies. The W1 detectors required +35 V applied to the front (ohmic) strips, the wedge detectors required -100 V and -40 V was supplied to the rings (junction side) of the TIARA detector.

3.7 Targets

In the original ^{11}B(^{3}He,d)^{12}C measurement of Reynolds *et al.* [24], it was stated that the ^{11}B target used was a self supporting enriched ^{11}B target. However, no further details were supplied. In the present measurement the ^{11}B target used is a self supporting ^{11}B foil with a total areal density of 395 μg/cm^2, made of 98% enriched pure material. The target was manufactured at iThemba LABS using electron heating and vacuum evaporation methods [55]. Also manufactured using this method was a natural boron target foil which was used to investigate the possibility of remnant ^{10}B present in the enriched material. The natural boron target was self supporting and 600 μg/cm^2 thick.

An Elastic Recoil Detection Analysis (ERDA) was performed on the enriched ^{11}B target to determine the extent of contaminants in the target. It was found that the target contained approximately 212 μg/cm^2 of ^{11}B as well as strong ^{16}O contamination of approximately 170 μg/cm^2, and, to a lesser extent, ^{12}C with a thickness of approximately 6 μg/cm^2. Weak ^{14}N contamination, approximately 7 μg/cm^2, was also measured. Nitrogen is believed to be found in Boron Nitrite (BN) compounds formed with the residual gas during the vacuum evaporation process. Carbon and Oxygen are from atmosphere since the evaporation process was not performed under vacuum. To investigate the effect of these contaminants in the region of interest, measurements on a

Li_2CO_3 target were performed. See Chapter 7 for more details.

For the $^{14}C(p,t)^{12}C$ measurements the ^{14}C target used was manufactured at the Joint Institute for Nuclear Research (JINR), Dubna, Russia. This enriched target was self-supporting and 300 $\mu g/cm^2$ thick, containing 80% ^{14}C and 20% ^{12}C. Other impurities on the target includes Ta, as Tantalum foil was used in the production of the target, as well as Oxygen, Hydrogen, Nitrogen and Chromium [56].

3.8 Experimental Procedures

With the discussion of the experimental setup now complete, the procedures followed when performing measurements reported in this study will now be discussed. The next two subsections deal with the experimental procedures followed in the (^{3}He,d) and (p,t) measurements.

3.8.1 (^{3}He,d) Reaction

For this measurement, the focal plane consisted of one original VDC, one new VDC and one $\frac{1}{4}$" paddle scintillation detector, resulting in a XXU wire-plane configuration. At the start of the experiment, five different targets were mounted on the target ladder, namely an empty frame target used for halo optimization, a ZnS target (viewer) used for positioning the beam on target, a Li_2CO_3 target for contaminants investigations, a natural Boron (600 $\mu g/cm^2$) target also for contaminant investigations as well as spectrometer resolution optimization, and the 98% enriched ^{11}B target (395 $\mu g/cm^2$) for data taking. The target ladder was then placed inside the scattering chamber (see Fig. 3.2(a)) and the scattering chamber was evacuated to a pressure of $P \sim 10^{-5}$ mbar. The spectrometer was moved to the desired laboratory angle. K600 magnet currents were then set to the appropriate deuteron fieldset values obtained from the computer program SPEXCIT.

To start the measurements, the 44 MeV ^{3}He beam was positioned in the center of the target. This is achieved with the use of the ZnS target. During this process the beam spot on the target is monitored with a camera positioned at one of the perspex ports of the scattering chamber. The beam spot was considered adequate when it was positioned at the center of the target, having a diameter of about 3 mm. Beam halo, secondary particles originating from scattering events in the beam-line, was investigated using the empty frame. For this particular measurement the beam halo was very low, as the count rate with beam on the empty frame target was only a few Hz. The low background is because of the low beam energy (resulting in a stable beam and clean extraction in the SSC), the large differences in rigidity between deuterons and beam particles, as well as the fact that the external beamstop was used.

Once a low beam halo count rate was confirmed the process of spectrometer kinematic optimization was started. This process required remotely adjusting the currents of the K and H-coils to ensure as little as possible angular dependence of the position of any particular state in the focal plane. Such an improvement in the resolution was determined from the two dimensional spectrum of deuteron emission angle versus the horizontal focal plane position. To speed up the optimization process, the thicker ^{nat}B target was used for spectrometer kinematic optimization. The ground state of ^{11}C from the ^{10}B(^{3}He,d)^{11}C reaction lies in the region of interest, and there is minimal mass difference between ^{11}C and ^{12}C. The online resolution of 77 keV (FWHM) for achromatic beam was considered suitable enough for this measurement.

At this point, the process of data taking began. The enriched Boron target was used for data acqusition. A typical experimental run lasted an hour. An empty target measurement was performed after every 5 runs to monitor the beam halo. Several runs for the investigation of contaminants were also performed using the Li_2CO_3 and natural boron targets. The experiment was completed over the course of one weekend and three different laboratory angles

were covered, namely $\theta_{lab} = 25°$, 30° and 35°.

3.8.2 (p,t) Reaction

Two original VDCs were used in this measurement, along with a $\frac{1}{4}$" paddle scintillation detector. The silicon detector array was put inside the scattering chamber together with the necessary cabling. For beam alignment, beam halo tuning, spectrometer resolution optimization and the silicon detectors testing, a target ladder was mounted with the following targets: a viewer (ZnS), an empty frame, ^{197}Au (220 μg/cm^2), natural carbon (1 mg/cm^2) and natural carbon (220 μg/cm^2). It should be noted that at this stage the ^{14}C target was not positioned on the target ladder. This was a precautionary measure to ensure the safety of the target before the actual measurement commences. Once the target ladder was placed inside the scattering chamber the scattering chamber was evacuated to a pressure of $P \sim 10^{-5}$ mbar. The spectrometer was then positioned at $\theta_{lab} = 21°$.

The 66 MeV proton beam was positioned in the center of the target using the ZnS viewer. Similar to the (^{3}He,d) reaction measurement, the beam alignment process was completed when the beam spot diameter at the center of the viewer was about 3 mm. The target was changed to ^{197}Au to perform spectrometer kinematic optimization using the ^{197}Au(p,p') elastic scattering reaction. This was achieved by varying currents of the H- and K-coils while investigating the improvements through the two dimensional spectrum of proton TOF versus the horizontal focal plane position. The resolution was further improved by performing the dispersion matching procedure. This procedure involves different beam optics in the P and S beamlines in order for an energy dispersive beam to be delivered to the target. This was followed by fine adjustments to beamline quadrupole magnets currents and beam slits along the beam-line. More in-depth discussion of the dispersion matching process can be found in Ref. [47]. The energy resolution achieved in this process was 29

keV (FWHM) for elastic proton scattering.

It should be noted that up to this point the silicon detectors were switched off to avoid damage through excessive particle flux that may result during the beam alignment and resolution optimization processes. Once the required bias voltage were supplied to the silicon detectors, they were tested with the beam on the thin ^{12}C target. The count rates on the silicon detectors were monitored using ORTEC model 449-2 rate-meters situated in the data room in order to establish discriminator threshold values. The beam halo was also investigated with the use of the empty frame target. The count rate was found to be below 4 Hz, which was considered good enough to perform the measurement.

The next step was to change the K600 magnetic settings to observe tritons. Only at this point was the ^{14}C target placed on the target ladder. The new ladder had the following targets: a viewer, ^{14}C (300 μg/cm^2) and an empty frame. At this point the real data taking could commence. The processes discussed above were performed at the beginning of each weekend. The experiment was performed on four consecutive weekends.

A typical experimental run lasted for two hours. Periodic measurements with the empty target frame were used to monitor the beam halo. During data acquisition the count rates on the silicon detectors were monitored in order to avoid damage through very high particle rates. The very high count rates on the silicon detectors could also lead to random coincidence events (see section 5.5). Thus, the count rates needed to be kept low through out the experiment. The count rate on silicon detectors were kept below 2 kHz per channel on average.

The silicon detectors were calibrated before and after the experiment using an α emitting ^{228}Th radioactive source. The source was put on the target ladder inside the scattering chamber, which was evacuated to the pressure of $P \sim 10^{-5}$ mbar.

Chapter 4

Data Analysis : (^{3}He,d)

With the discussion of the experimental setup and procedures completed in the previous chapter, the data analysis of the experimental data of the singles ^{11}B(^{3}He,d)^{12}C measurement can now be discussed. As mentioned before the aim of this measurement was to investigate the existence of the 11.16 MeV state in the ^{12}C nucleus, and if it is found to study its 2^+ character. The existence of this state was first claimed in the measurements performed in the 70's by Reynolds *et al.* [24], with Ref. [25] also claiming to have found proof of its evidence. It was postulated to be a candidate of the 2^+ excitation of the Hoyle state. This chapter reports on data analysis performed for the (^{3}He,d) measurement.

4.1 Data Extraction

The raw data in the form of event files, created by the MIDAS data acquisition (DAQ) system, can be converted into ROOT files [57] and analyzed offline. The offline event-by-event analysis is performed using the code *f-plane.c* developed at iThemba LABS using the C++ programming language. Figure 4.1 presents the flow chart of how *f-plane.c* extracts information during the offline analysis for every recorded event.

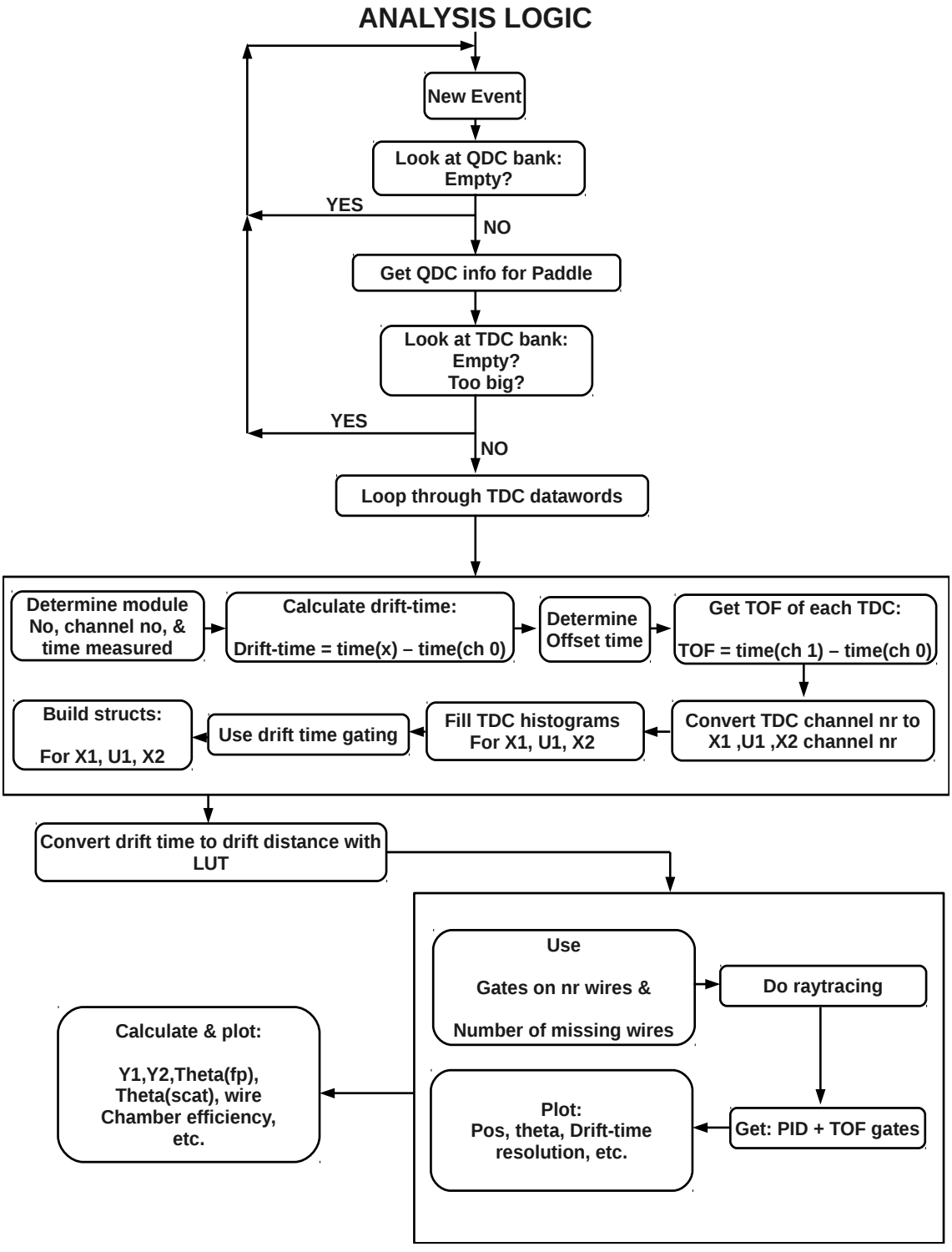

Figure 4.1: Flow diagram for the event-by-event offline analysis.

4.2 Particle Identification

The first step in the offline analysis involves the identification of particles detected in the focal plane detectors. Figure 4.2 shows the two-dimensional spectrum of the TOF against the energy deposited by the charged particles in the scintillation detector. It can be seen that two different types of charged particles were transported to the focal plane during this measurement, illustrated by the two blobs labeled A and B.

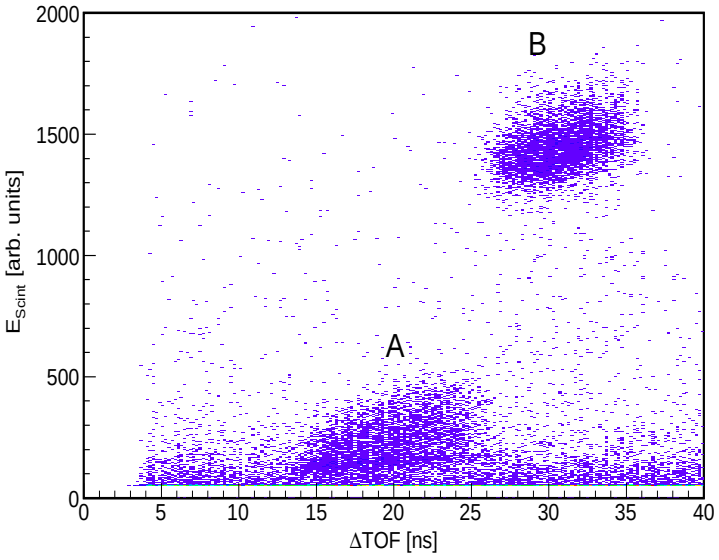

Figure 4.2: A particle identification spectrum of the pulse height in the scintillator versus relative TOF measurements. A and B show that two different types of charged particles were detected in the focal plane during the experiment.

TOF calculations were performed to determine which particles represent these blobs. The calculations were performed for charged particles which are most likely to make it to the focal plane based on their rigidity, shown in Table 4.1. Column 1 represents the particle of interest and column 2 corresponds to values of minimum and maximum energy for the charged particles in a given deuteron magnetic field set. Column 3 represents the K value range (see Appendix A for the determination of energy and K-value range). Based on the

obtained energy values, it can be concluded that only deuterons and tritons can be detected. Column 4 corresponds to the relative TOF range calculated using the energy range given in column 2.

The TOF calculations were performed using the equation,

$$TOF = \frac{d}{v}, \tag{4.1}$$

where d is the flight path of the particle in the K600 spectrometer (8.14 m on average) and v is its velocity. The velocity of the particle is calculated relativistically, using the equation

$$v = c \cdot \sqrt{1 - \left(\frac{M}{E_{total}}\right)^2}, \tag{4.2}$$

where c is the speed of light, $M = mc^2$ represents the rest mass energy and $E_{total} = M + E_{kinetic}$. For a 44 MeV ^{3}He beam, the time interval between different beam packets from the cyclotron is 41.5 ns. Therefore, without pulse selection, the measurable TOF range is 41.5 ns. In column 4 of Table 4.1, it is seen that the TOF of all particles exceeded this value. Therefore it is in principle possible for particles with different TOFs to be detected at the same time if they come from different beam packets. Calculations were performed to determine where the TOF region of each particle would fall when overlapping TOF regions are taken into account. Column 5 of Table 4.1 shows the resulting times, which fortunately remain unique.

Since rigidity calculations showed that only deuterons and tritons can reach the focal plane, due to the limited kinetic energy available, one can use the calculated TOF from column 5 to plot the theoretical TOF spectrum, shown in Fig. 4.3. The Y axis represents the energy deposited by the particles into the scintillation detector. This was calculated using the program ELOSS [58] for the particles entering the scintillation detector. It should be noted that, the energy loss calculations take into account the various materials that the particles traverse in the focal plane before reaching the scintillators.

Comparing Fig. 4.2 with Fig. 4.3, it can be seen that particles A and B can be assigned to tritons and deuterons respectively. All further analysis reported in this chapter, unless otherwise stated, was performed with a software gate selecting the deuterons locus.

Particle	E range [MeV]	K range [u.MeV.c^{-2}]	TOF range [ns]	Wrapped TOF range [ns]
d	40.80 - 49.20	82.54 - 99.09	120.8 - 131.9	25.80 - 36.90
p	81.90 - 98.32	82.54 - 99.09	63.80 - 69.10	10.30 - 15.60
t	27.37 - 32.85	82.54 - 99.09	178.98 - 195.8	0.98 - 17.80
^{3}He	109.5 - 131.4	82.54 - 99.09	91.78 - 100.0	5.00 - 38.28
^{4}He	82.48 - 99.03	82.54 - 99.09	120.49 - 131.5	25.49 - 36.50

Table 4.1: TOF and K-value calculations for the magnetic field chosen to detect deuterons. Column 3 shows the calculated K-value for the particle of interest. The TOF range in column 4 corresponds to minimum and maximum estimated TOFs based on minimum and maximum energies in column 2. Column 5 shows the TOF ranges which should be measured with the overlapping of time measurement from beam packet time structure taken into account.

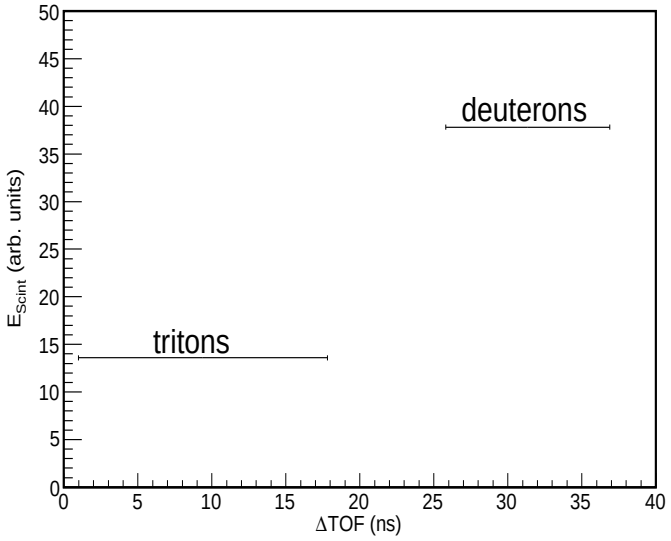

Figure 4.3: The calculated PID spectrum for tritons and deuterons.

4.3 VDC Position Determination

The position at which the particle traverses the X1 wire-plane is referred to as the *focal-plane position*. For all valid VDC events, the focal-plane position is determined. A valid VDC event is defined as an event where, among other requirements, there must be coincidence between the scintillator and the wire chamber, and at least 3 and fewer than 9 signal wires registered a hit. A further requirement for a valid event is that the drift times should fall within a specified range, as illustrated in Fig. 4.4. In order to determine an accurate focal plane position, accurate drift time measurements are required. Once the drift times are known the drift length, the distance from the signal wire to the position where the particle passed through the drift cell, can be determined.

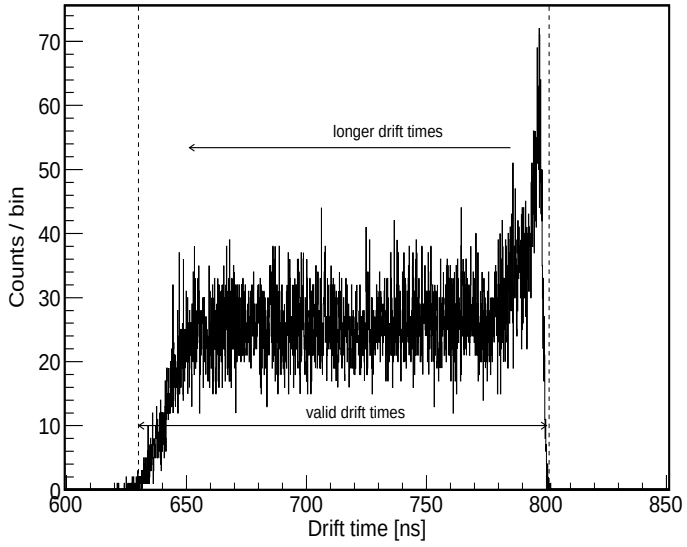

Figure 4.4: The drift time spectrum for the X1 wire-plane.

One of the new VDC was utilized in the present measurement which has a X-U wire chamber configuration. This configuration makes it possible to measure the vertical position (Y) information in addition to the horizontal position (X) information. With the Y-position information, the additional gate can be applied in order to further remove background from data. This is

done by choosing events which fall between Y1 = -25 mm and Y1 = -25 mm as illustrated in Fig. 4.5.

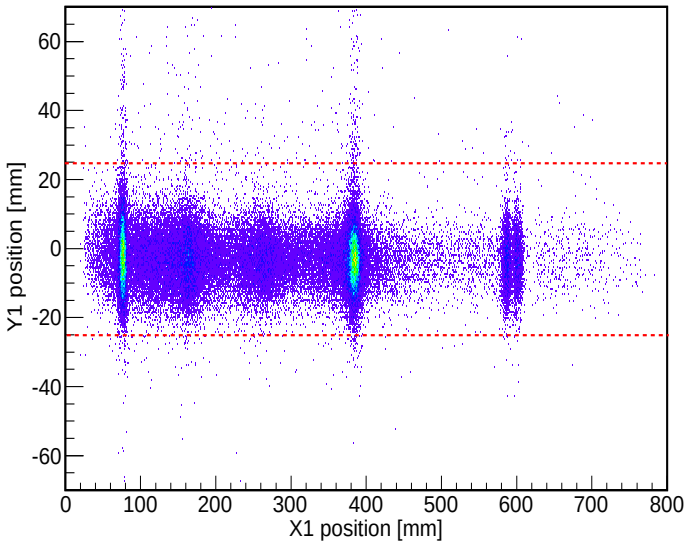

Figure 4.5: A 2D spectrum of the vertical position Y as a function of the horizontal position X. Most of the valid reaction events are choosen between -25 and +25 mm.

Determination of Drift Times

The determination of accurate drift times is achieved in a few steps. This is due to different time offsets of different preamplifier channels, the differences in cable length between the VDC preamplifiers and the TDCs, as well as the way the TDC was designed. The TDC trigger input was not designed to have a high time resolution, and is only used to help define a time window for the so-called *Trigger Matching Mode* [53]. In order for accurate times to be measured a copy of the trigger signal is supplied to the first channel of each TDC. Accurate drift times are therefore determined by taking the time difference between any particular TDC channel and the first TDC channel, which is a copy of the paddle trigger signal:

$$drifttime(i) = time(trigger) - time(i),$$

where i denotes the TDC channel number. To correct for different time offsets due to differences in the response of different preamplifiers channels, as well as slight differences in cable lengths, an offset correction was implemented [47]. Differences between channels on the order of several nanoseconds were corrected in this way. The corrected time is referred to as the *offset_time* in the analyzer code:

$$offset\_time(i) = drifttime(i) - offset(i).$$

Figure 4.4 shows an average drift time spectrum for all signal wires of the X1 wire-plane. The peak from the the drift time spectrum indicates the region next to signal wires where the electric field lines are quasiradial. In this region electrons will have faster drift velocities resulting into shorter drift times. The plateau region indicates the region next to the guard wires where there is uniform electric field with parallel electric fields lines. For a more in-depth discussion refer to Refs. [49, 59].

Mapping wire number to TDC channel

The table used in the software to map the TDC channel number to the wire numbers of the different wire-planes is shown in Table 4.2. For this measurement one original VDC and one new VDC were used. This resulted in the XXU wireplane configuration.

Lookup Table

Once the offsets have been set a lookup table (LUT) is generated. The LUT is used in determining the drift length corresponding to drift time. Figure 4.6 shows a typical LUT spectrum, generated by integrating the drift times according to the integral-time-spectrum method discussed in Ref. [60].

Wire-plane	Preamplifier number	Signal wires	Preamplifiers channels	TDC number	TDC connector	TDC channels	DAQ channels
X1	1	1 - 8	9 - 16	1	A2	24 - 31	0 - 7
	2	9 - 24	17 - 32	1	B1	32 - 47	8 - 23
	3	25 - 40	33 - 48	1	B2	48 - 63	24 - 39
	4	41 - 56	49 - 64	1	C1	64 - 79	40 - 55
	5	57 - 72	65 - 80	1	C2	80 - 95	56 - 71
	6	73 - 88	81 - 96	1	D1	96 - 111	72 - 87
	7	89 - 104	97 - 112	1	D2	112 - 127	88 - 103
	8	105 - 120	113 - 128	2	A2	144 - 159	104 - 119
	9	121 - 136	129 - 144	2	B1	160 - 175	120 - 135
	10	137 - 152	145 - 160	2	B2	176 - 191	136 - 151
	11	153 - 168	161 - 176	2	C1	192 - 207	152 - 167
	12	169 - 184	177 - 192	2	C2	208 - 223	168 - 183
	13	185 - 198	193 - 206	2	D1	224 - 237	184 - 197
X2	1	16 - 1	1 - 16	4	B1	32 - 47	515 - 500
	2	32 - 17	17 - 32	4	B2	48 - 63	531 - 516
	3	48 - 33	33 - 48	4	C1	64 - 79	547 - 532
	4	64 - 49	49 - 64	4	C2	80 - 95	563 - 548
	5	80 - 65	65 - 80	4	D1	96 - 111	579 - 564
	6	96 - 81	81 - 96	4	D2	112 - 127	595 - 580
	7	112 - 97	97 - 112	5	A2	16 - 31	611 - 596
	8	128 - 113	113 - 128	5	B1	32 - 47	627 - 612
	9	144 - 129	129 - 144	5	B2	48 - 63	643 - 628
	10	60 - 145	145 - 160	5	C1	64 - 79	659 - 644
	11	176 - 161	161 - 176	5	C2	80 - 95	675 - 660
	12	192 - 177	177 - 192	5	D1	96 - 111	691 - 676
	13	198 - 193	193 - 198	5	D2	112 - 117	697 - 692
U2	1	1 - 16	1 - 16	6	A2	16 - 31	800 - 815
	2	17 - 32	17 - 32	6	B1	32 - 47	816 - 831
	3	33 - 48	33 - 48	6	B2	48 - 63	832 - 847
	4	49 - 64	49 - 64	6	C1	64 - 79	848 - 863
	5	65 - 80	65 - 80	6	C2	80 - 95	864 - 879
	6	81 - 96	81 - 96	6	D1	96 - 111	880 - 895
	7	97 - 112	97 - 112	6	D2	112 - 127	896 - 911
	8	113 - 128	113 - 128	7	A2	16 - 31	912 - 927
	9	129 - 143	129 - 143	7	B1	32 - 46	928 - 942

Table 4.2: Mapping wire number to TDC channel for one original VDC and one new VDC in a XXU configuration, as used in the (^{3}He,d) measurement.

Determination of Drift Lengths

After determining the drift times, the drift lengths are determined using knowledge about drift velocities implicit in the LUT. Drift times measured for individual wires are translated into drift lengths with the help of the LUT. Figure 4.7 shows a typical drift length spectrum. The peak at 0 mm resulted from electronic noise, and is ignored in the ray-tracing procedure used to determine the focal plane position.

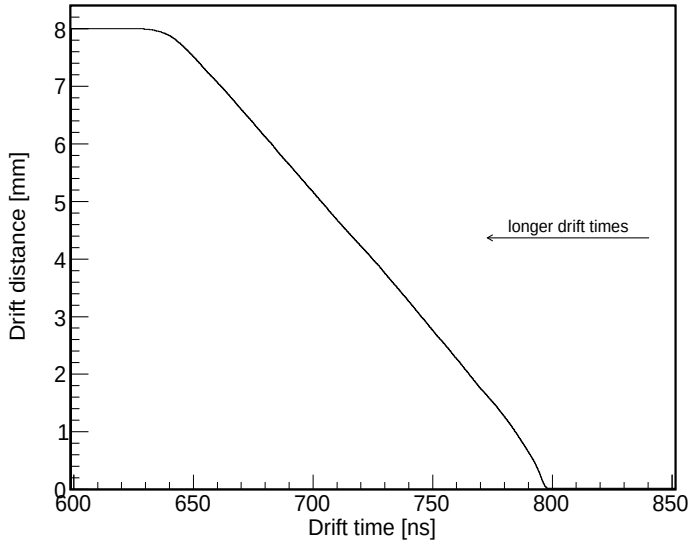

Figure 4.6: A typical lookup table relating drift times to drift lengths.

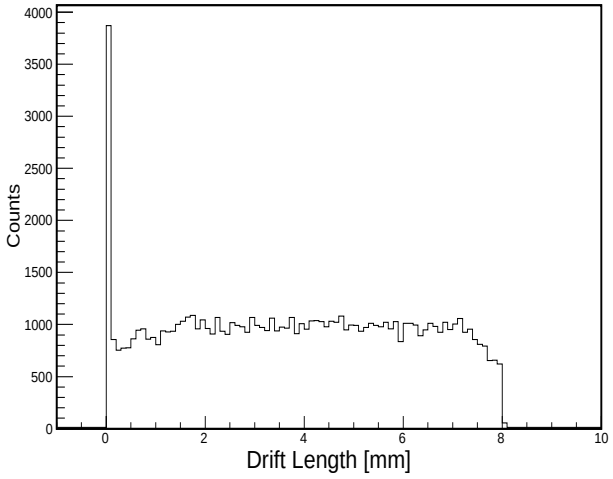

Figure 4.7: A typical drift length spectrum for the X1 the wire-plane.

4.4 VDC Position Resolution

Figure 4.8 shows a schematic overview of a wire-plane where three wires are triggered by a particle traversing the VDC. The drift length accuracy estimated from the consistency of three drift lengths, d_{i-1}, d_i and d_{i+1}, is represented by Δ, which is the quantity:

$$\Delta = \frac{\mid d_{i+1} - d_{i-1} \mid}{2} - d_i \ , \tag{4.3}$$

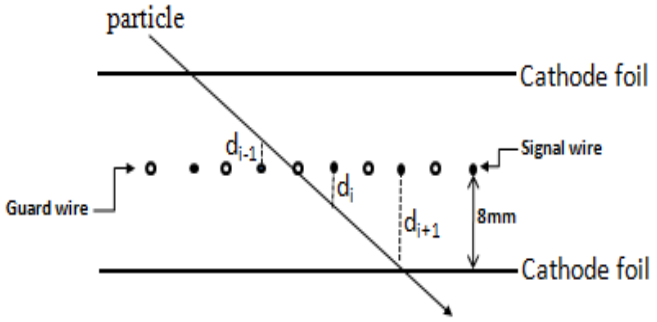

Figure 4.8: Schematic overview of the trajectory of a charged particle traversing the VDC.

In an ideal measurement, it is obvious this quantity should be zero. In reality Δ should a distribution centered around zero. However, it is often found that Δ plotted as a function of $b - integer(b)$, where b represents the focal plane position, is a step-function, as shown in Fig. 4.9(a). This is due to incorrect drift time measurements, which can be the result of delays in the trigger signal that serves as a common stop for the determination of drift times. The incorrect drift times leads to uncertainty in the drift-length determination via the lookup table. These uncertainties translates to fluctuations in the value of the spatial resolution. The fluctuations can be corrected by properly shifting the lookup table hence correcting the drift times. An example of

spatial resolution Δ is shown in Fig. 4.9 showing how properly shifting the lookup table can resolve the resolution fluctuations. Figure 4.9(a) shows the 2D resolution plot of Δ as a function of $b - integer(b)$. The variable b is the actual position on the wire-plane where the particle passed through, and $integer(b)$ is the nearest signal wire position. Figure 4.9(b) shows the corresponding projection of events on the Δ axis. Figures 4.9(c) and 4.9(d) respectively show the 2D and 1D spectra for a properly shifted lookup table.

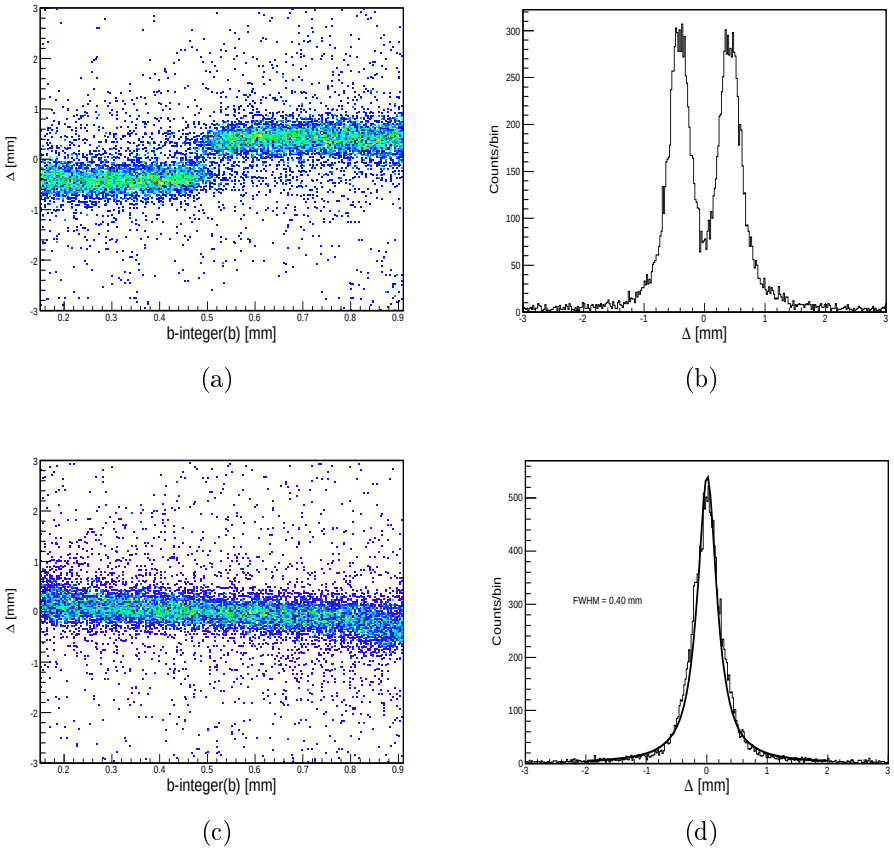

Figure 4.9: Position resolution plots for deuterons of Δ (b, d), and the two-dimensional of Δ vs. $b - integer(b)$ (a, c), for different LUT offsets.

4.5 VDC Efficiency

The efficiency of the drift chamber ϵ, is an indication of its ability to detect charged particles traversing the focal plane. A poor value of efficiency during the experimental run can be an indication of problems with gas flow or problems with the TDC functionality. The efficiency is given by the product of the geometrical efficiency (ϵ_g) and the intrinsic efficiency (ϵ_i) parameters [47],

$$\epsilon = \epsilon_g \cdot \epsilon_i. \tag{4.4}$$

It has been determined that for the K600 magnetic spectrometer, the geometrical efficiency can be assumed to be 100% [47]. The intrinsic efficiency on the other hand can be defined as

$$\epsilon = \frac{N_{valid}}{N_{tot}}, \tag{4.5}$$

where N_{tot} denotes the total number of PID selected events recorded in the focal-plane of the spectrometer. The quantity N_{valid} denotes the number of valid events recorded, as discussed in sec 4.3. For the measurements reported in this thesis, it was assumed that the scintillation detector has 100% detection efficiency. The original VDC was operated with an average efficiency of ∼97% while the new VDC had average efficiencies of ∼96% and ∼95% for the X-wireplane and U-wireplane respectively.

4.6 The Focal Plane Position Spectrum

The focal plane position is determined with a ray-tracing algorithm which determines the crossing point in the wire-plane by employing a least squares fit of straight lines through the valid (wire; drift distance) coordinates. Figure 4.10 shows the focal plane position spectrum obtained for the ^{11}B(^{3}He,d)^{12}C reaction for measurement performed at $\theta_{lab} = 30°$. The kinetic energy of particles decreases from right to left in the focal plane position spectrum,

hence the higher excited states of the recoil nucleus are situated on the left of the spectrum.

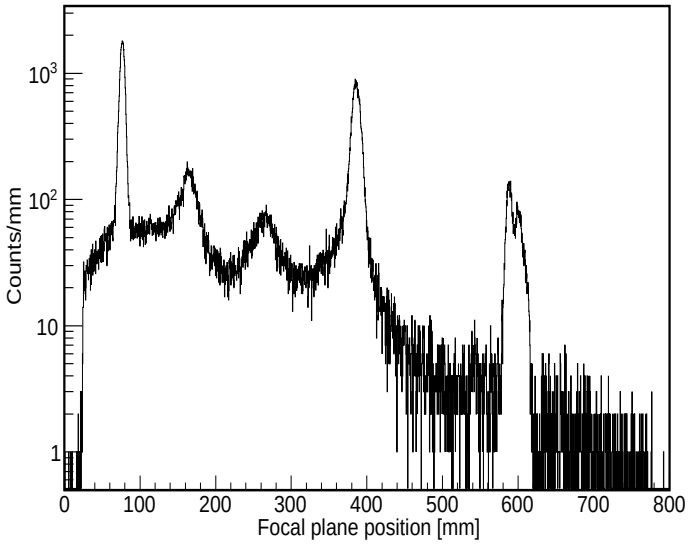

Figure 4.10: The focal plane position spectrum for the ^{11}B(^{3}He,d)^{12}C measurement at $\theta_{lab} = 30°$.

4.7 Improving Energy Resolution

It is well known that the energy resolution obtained during the online analysis can be improved further during offline data analysis. A lineshape correction is used to correct the data for the remaining optical and kinematical abberations not corrected with the K and H-coils [61]. This section reports on offline energy resolution improvements performed for the $\theta_{lab} = 25°$ measurement. It should be noted that this process was also performed for the $\theta_{lab} = 30°$ and 35° measurements.

Figure 4.11 shows spectra of the deuteron emission angle against focal plane position. Two states shown are the ^{12}C Hoyle state situated at 620 mm and the ^{11}C ground state situated at 685 mm. Figure 4.11(a) shows the spectrum before the lineshape correction. From the figure it can been seen that the peaks

obtained in the projection to the position spectrum will yield broad peaks in the focal plane position. tFig. 4.11(b) shows the effect of the corrections on the peaks. The resolution improvement is more visible in the one-dimensional focal-plane position spectrum shown in Fig. 4.12. The black line represents the data before the correction, with an energy resolution of the Hoyle state peak (indicated with an arrow) at 77 keV (FWHM). After the corrections the energy resolution has been improved to 63 keV, which shows that lineshape correction can improve resolution by as much as 14 keV.

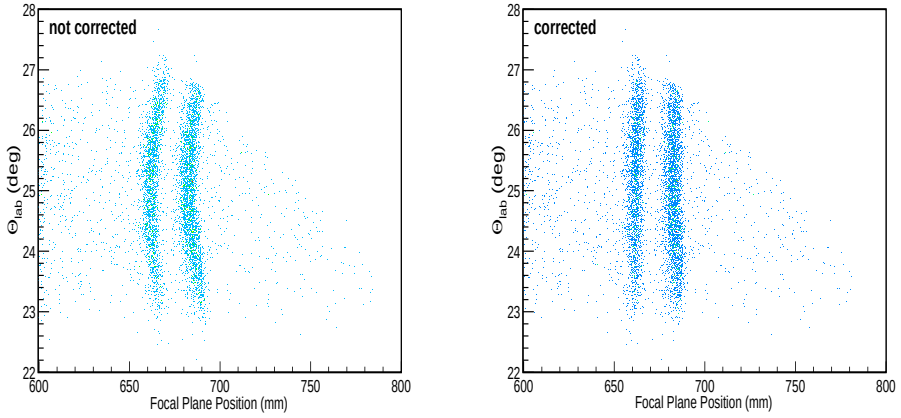

(a) (b)

Figure 4.11: The two dimensional plot of deuteron emission angle versus the focal-plane position spectrum, before (a) and after (b) the lineshape correction was applied.

4.8 Energy Calibration

Focal plane position spectra, shown in Fig. 4.10, must be transformed into the excitation energy spectra of the excited nucleus of interest. Since the ^{12}C nucleus has several precisely known peaks in the region of interest, the reaction ^{11}B(^{3}He,d)^{12}C was used both for measurement and for calibration purposes.

From Ref. [60] it follows that there is a quadratic relationship between particle momentum and the position at which the particle traverses the focal

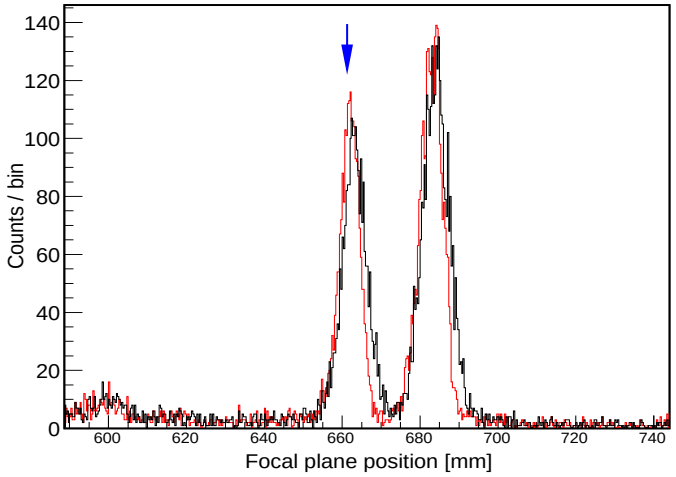

Figure 4.12: The one dimensional focal-plane position spectrum shown before (black) and after (red) lineshape correction. This resulted in an resolution improvement of 14 keV. The Hoyle state is indicated by the arrow.

plane. The relationship is given as,

$$pc = aX_F{}^2 + bX_F + d \ , \tag{4.6}$$

where pc represents the particle's momentum in MeV, X_F is the focal-plane position and a, b and d are fitting parameters. Relativistically, the relationship between the ejectile's momentum and the recoil excitation energy is such that it is reasonable to also use a quadratic relationship between the recoil excitation energy and the focal-plane position. Then

$$E_x = eX_F{}^2 + fX_F + g \ , \tag{4.7}$$

where e, f and g are fitting parameters. Knowing the focal-plane position at which the accurately known excitation states of ^{12}C are situated, one can use Eq. (4.7) to obtain the parameters through the quadratic fit shown in Fig. 4.13.

The fitting parameters obtained for measurement at $\theta_{lab} = 25°$, $30°$ and $35°$ are shown in Table 4.3.

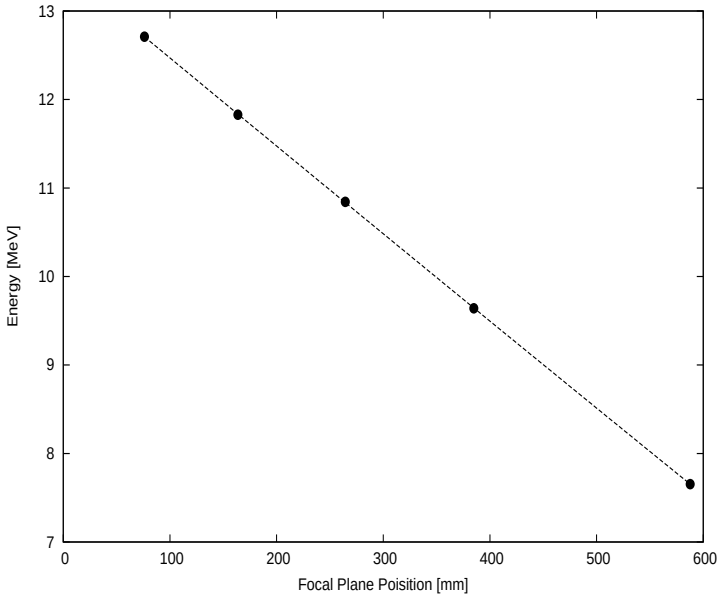

Figure 4.13: Second order polynomial fit of excitation energy as a function of focal-plane position (X_{FP}) for several known states of ^{12}C.

Laboratory Angle	e	f	g
25°	2.51096×10^{-7}	-0.00999193	14.1584
30°	2.03743×10^{-7}	-0.01001410	13.4689
35°	3.63471×10^{-7}	-0.00984894	13.9452

Table 4.3: Calibration parameters of the K600 for the three measurement at different laboratory angles.

^{12}C state [MeV]	Focal Plane Position [mm]
12.71	76.16
11.828	163.73
10.844	264.39
9.641	384.85
7.654	587.76

Table 4.4: Focal plane position calibration data used to calibrate the 35° measurement.

Table 4.4 shows the ^{12}C states used in the calibration as well as their corresponding focal plane positions.

Chapter 5

Data Analysis : (p,t)

This chapter describes the data analysis for the complete kinematics measurement. In this measurement the K600 magnetic spectrometer focal plane detection package was complemented with the silicon detectors in the scattering chamber. Before discussing the analysis procedure, the silicon detector gain matching procedure as well as energy calibration are first discussed in section 5.1. Section 5.2 discusses the analysis tools used, in section 5.3 the analysis for singles events is discussed, and in section 5.4 the background investigation is presented. Finally, the coincidence event analysis is presented in section 5.5.

5.1 Silicon Detector Gain Matching and Calibration

Prior to the experiment, the output of the CAEN N568 amplifier channels were aligned in a gain matching procedure. To do this the silicon array was placed inside the scattering chamber. To allow free movement of α-particles, the scattering chamber was pumped down to the vacuum pressure of $P \sim 10^{-5}$ mbar. The geometry of the detectors resembled that used during the experiment, as shown in Fig. 3.7. The signal processing was as seen in Fig. 3.9. A ^{228}Th

α-source was mounted on the target ladder and placed inside the scattering chamber facing towards the detector array. The gain matching procedure was performed by controlling the amplifier settings remotely through the use of the CAEN A1301 PCI card. A bash script was written to control the amplifier parameters such as global offset, course gain, fine gain, pole zero and shaping time. These were changed until the α peaks appeared at the desired position in the ADC. The gain matching process resulted in the dynamical range of the ADCs covering the α-particles energies ranging from 0 MeV to 10 MeV[3]. This is illustrated in Fig. 5.1 where several α peaks from the decay of ^{228}Th and its daughter nuclei are shown.

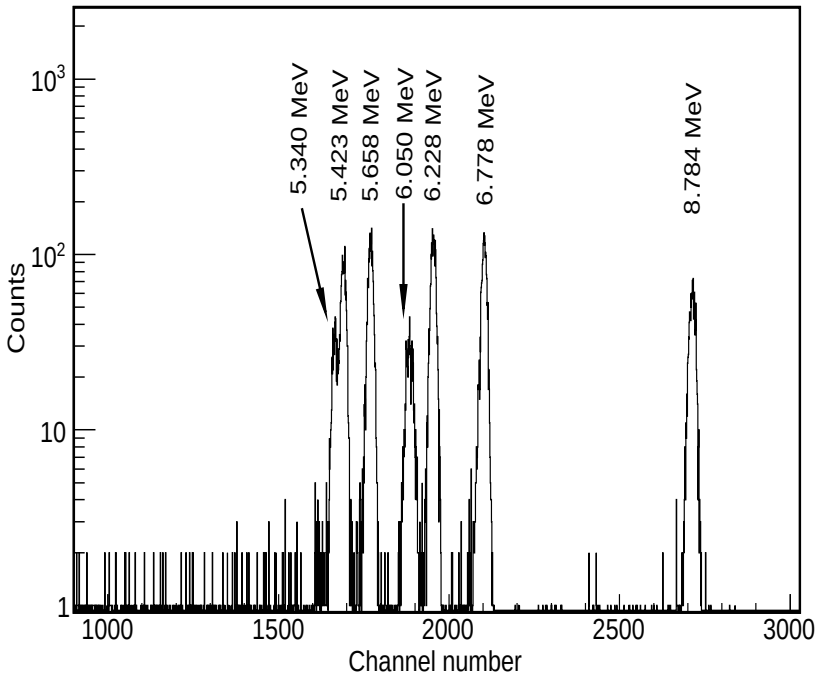

Figure 5.1: A typical ADC spectrum for a ^{228}Th source. The α-energies are indicated in MeV.

After the gain matching procedure, data were recorded for silicon detector calibration purposes. Calibration entailed identifying the channel at which

[3]The expected energies of the α-particles in the excitation energy of interest ranges from 1 MeV to 4 MeV.

different α peaks are located in the ADC spectrum shown in Fig. 5.1. In order to identify the peaks one need to know ^{228}Th decay chain. The ^{228}Th nucleus can decay to ^{224}Ra by emitting α-particles with four different energies, 5.423 MeV (72%), 5.340 MeV (27%), 5.210 MeV (0.4%) and 5.176 MeV (0.23%) [62]. The ^{224}Ra nucleus then α-decays to the ^{220}Rn by emitting α-particles with two different energies 5.685 MeV (94.49%) and 5.448 MeV (5.1%) [63]. The ^{220}Rn nucleus decays to the ^{216}Po through emission of 6.288 MeV (99.9%) and 5.747 MeV (0.1%) α-particles [64], thereafter the ^{216}Po emits 6.778 MeV (100%) α-particles to decay to ^{212}Pb [65]. From there the β^- decay of ^{212}Pb and ^{212}Bi respectively lead to ^{212}Po [66, 67]. Finally ^{212}Po emits 8.784 MeV (64%) α-particles to decay to the stable ^{208}Pb [68].

After identification of the α peaks, a Gaussian fit is performed in order to obtain the peak centroids. Using the peak's energy and ADC channel at which the peak is situated, a linear fit can be generated to obtain the calibration coefficients of each strip, as shown in Fig. 5.2. In the figure the slope and offset parameters for the linear fit are provided. The slope and offset parameters obtained for each strip were used during the offline data analysis in order to convert the ADC channel into particle energy.

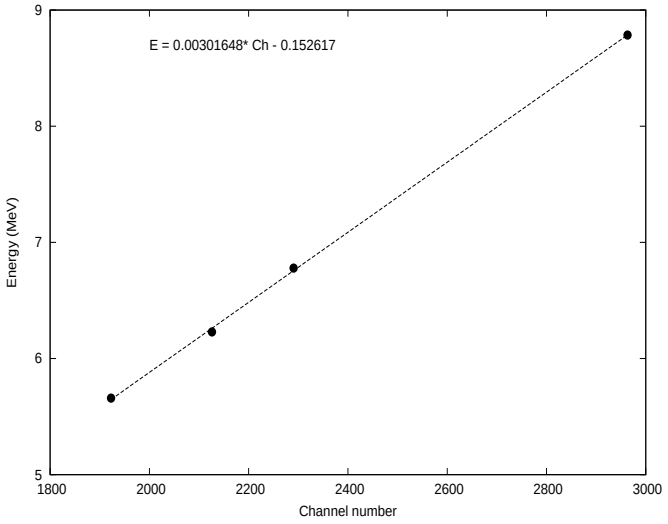

Figure 5.2: A typical linear calibration curve used for an individual silicon strip.

5.2 Analysis Tools

The triggering mode for the complete kinematics measurement was operated with the spectrometer as master trigger while the silicon detectors were operated in slave mode. This means whenever the K600 records an event, pulse height information within a 6 μs time window is registered for all channels in the ADCs. This led to two types of events being acquired for this measurement, i.e. singles events (triton only events) and the coincidence events (events where there is valid coincidence between spectrometer and silicon detectors).

To aid the analysis of the coincidence events, the offline analysis software codes *f-plane.c* and *SimSort* (discussed in Appendix D) were utilized. All relevant K600 focal plane parameters as well as the raw ADC data (and associated TDC data) were passed from *f-plane.c* to *SimSort*. Using *SimSort*, coincidence events between tritons and one, two, or three particles detected with the silicon detectors could then be extracted. The type of coincidence event required is defined by the user in the input file. For analysis performed in this study, three types of events were considered, namely the singles, doubles (coincidence of tritons with one particles) and triples (coincidence of tritons with two particles).

5.3 Focal Plane Singles Spectrum

This section presents the analysis procedure followed for singles events, the method followed is similar to the one discussed in Chapter 4.

5.3.1 Particle Identification

The first step in offline data analysis always involves identifying the particles detected during the experiment. The aim of the present measurement was to investigate the coincidence of tritons detected in the spectrometer focal

plane with the charged particles detected with the Silicon array. The tritons in the focal plane should be uniquely identified. The method used for particle identification is similar to the one explained in Chapter 4.

Figure 5.3 shows the two dimensional plot of the relative TOF of particles against the energy deposited by the particles in the paddle detector. In the figure it is visible that only one type of charged particle was transported to the focal plane for the magnetic field of interest. Because the fields were set for tritons these particles could be uniquely identified as tritons. For further analysis, a software gate, as indicated in the figure, was applied.

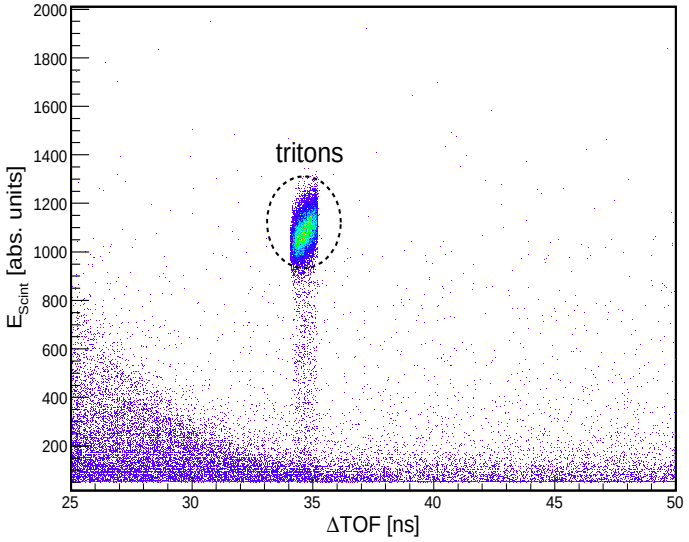

Figure 5.3: A particle identification spectrum of the pulse height in the scintillator versus relative TOF measurements showing the triton locus circled.

5.3.2 VDC Position Determination

The determination of the focal-plane position followed in this section resembles that presented in section 4.3. The focal plane detection package used in this measurement differed from the one used in (^{3}He,d) measurement. For this measurement, two original VDC's were used. This resulted in an XX wireplane

configuration. Table 5.1 shows how the software maps wire number to TDC channel for such a configuration.

Wire-plane	Preamplifier number	Signal wires	Preamplifiers channels	TDC number	TDC connector	TDC channels	DAQ channels
X1	1	1 - 8	9 - 16	1	A2	24 - 31	0 - 7
	2	9 - 24	17 - 32	1	B1	32 - 47	8 - 23
	3	25 - 40	33 - 48	1	B2	48 - 63	24 - 39
	4	41 - 56	49 - 64	1	C1	64 - 79	40 - 55
	5	57 - 72	65 - 80	1	C2	80 - 95	56 - 71
	6	73 - 88	81 - 96	1	D1	96 - 111	72 - 87
	7	89 - 104	97 - 112	1	D2	112 - 127	88 - 103
	8	105 - 120	113 - 128	2	A2	144 - 159	104 - 119
	9	121 - 136	129 - 144	2	B1	160 - 175	120 - 135
	10	137 - 152	145 - 160	2	B2	176 - 191	136 - 151
	11	153 - 168	161 - 176	2	C1	192 - 207	152 - 167
	12	169 - 184	177 - 192	2	C2	208 - 223	168 - 183
	13	185 - 198	193 - 206	2	D1	224 - 237	184 - 197
X2	1	16 - 1	1 - 16	4	B1	32 - 47	500 - 515
	2	32 - 17	17 - 32	4	B2	48 - 63	516 - 531
	3	48 - 33	33 - 48	4	C1	64 - 79	532 - 547
	4	64 - 49	49 - 64	4	C2	80 - 95	548 - 563
	5	80 - 65	65 - 80	4	D1	96 - 111	564 - 579
	6	96 - 81	81 - 96	4	D2	112 - 127	580 - 595
	7	112 - 97	97 - 112	5	A2	16 - 31	596 - 611
	8	128 - 113	113 - 128	5	B1	32 - 47	612 - 627
	9	144 - 129	129 - 144	5	B2	48 - 63	628 - 643
	10	60 - 145	145 - 160	5	C1	64 - 79	644 - 659
	11	176 - 161	161 - 176	5	C2	80 - 95	660 - 675
	12	192 - 177	177 - 192	5	D1	96 - 111	676 - 691
	13	198 - 193	193 - 198	5	D2	112 - 117	692 - 697

Table 5.1: Mapping wire number to TDC channel for two original VDC's in an XX configuration, as used in the (p,t) measurement.

Figure 5.4(a) shows an average drift times spectrum while Fig. 5.4(b) presents the LUT relating the drift times to drift lengths for the X1 wire-plane. The position resolution Δ was calculated using Eq. (4.3). As in the (^{3}He,d) measurement, the measured resolution can be optimized offline by adjusting the global shift in the lookup table. Figure 5.5 shows an example of the optimized position resolution.

The efficiency ϵ of the drift chamber is also calculated using Eq. (4.4). It is also assumed that the scintillation detector has 100% efficiency in this

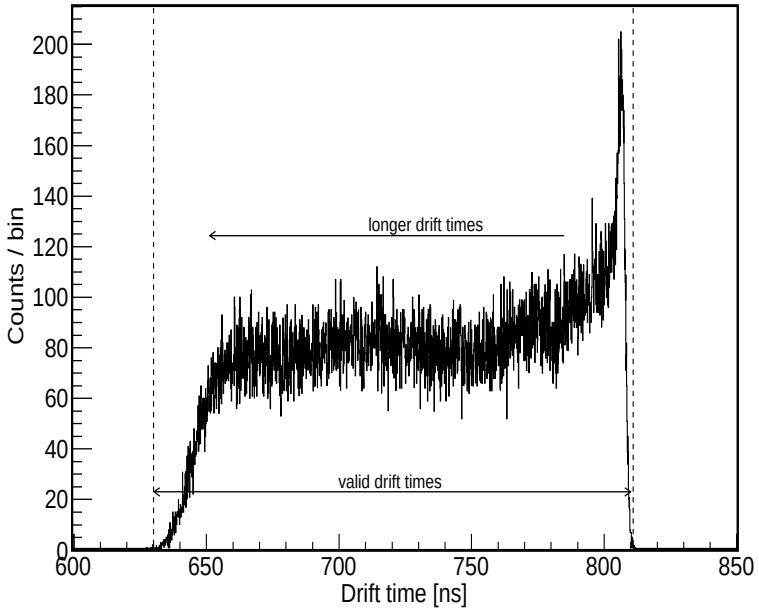

(a)

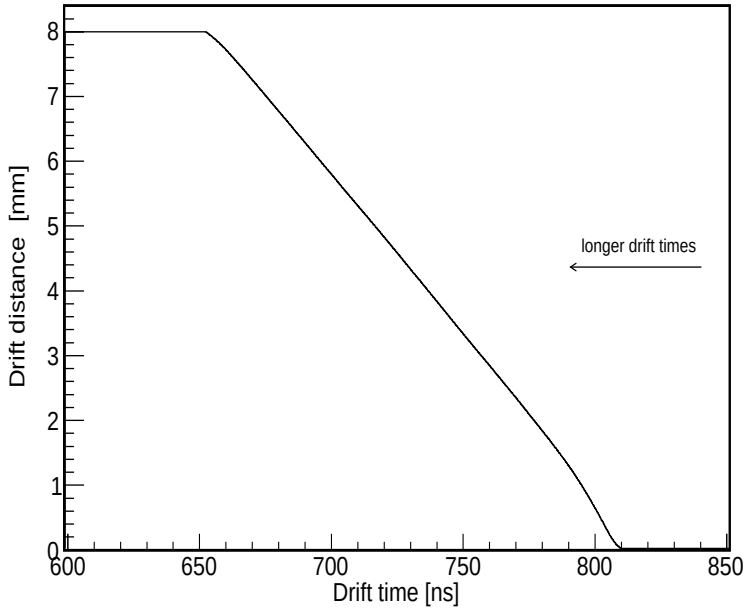

(b)

Figure 5.4: The typical spectra for the (a) drift time and (b) LUT for the X1 wire-plane.

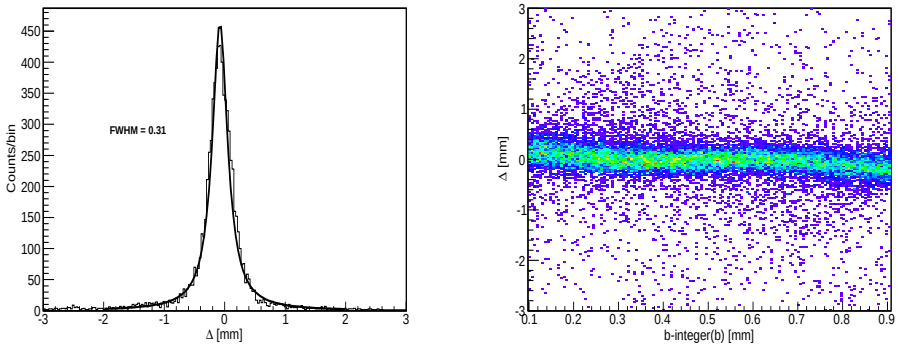

(a) (b)

Figure 5.5: Position resolution plot for tritons of Δ (a) with FWHM indicated, and the two-dimensional spectrum (b) of Δ vs. $b - integer(b)$.

measurement. The first VDC was operated with an average efficiency of ∼97% while the second VDC was operated with an average efficiency of ∼96%.

5.3.3 The focal Plane Position Spectrum

The ray-tracing algorithm discussed in section 4.6 is also responsible for determining the focal plane position. Figure 5.6 shows focal plane position spectra obtained for the (p,t) measurement for two different tritons magnetic field. Figure 5.6 shows the spectrum for a 52 MeV tritons magnetic field (top) covering the ^{12}C excitation energy region between 6 - 15.3 MeV and for a 50.3 MeV triton magnetic field (bottom) covering the ^{12}C excitation energy region between 8 - 17 MeV.

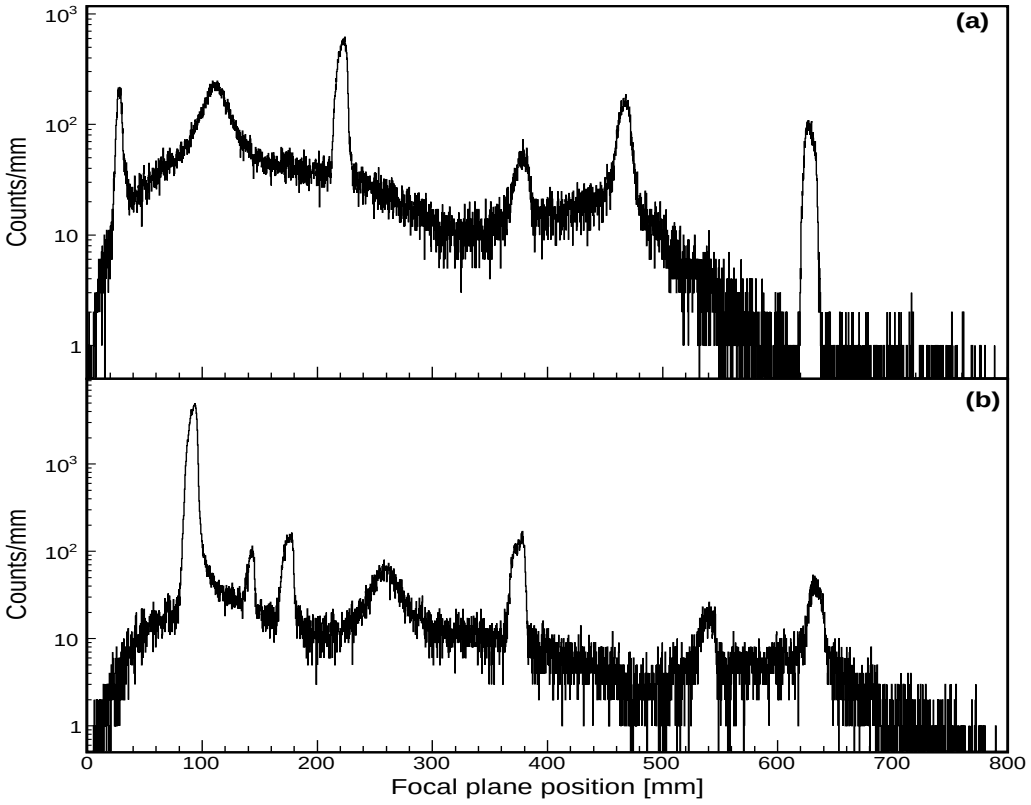

Figure 5.6: The focal plane position spectra for (a) 52 MeV and (b) 50.3 MeV triton magnetic field setting for the (p,t) measurement on ^{14}C.

5.3.4 Improving Energy Resolution

The energy resolution for the Hoyle state in the focal plane position spectrum shown in Fig. 5.6(a) is 104 keV (FWHM). As mentioned in Chapter 4, the energy resolution can be improved during the offline analysis using the lineshape correction technique. In contrast with the analysis performed for the (^{3}He,d) measurement, the energy resolution improvement in the current analysis was achieved using the TOF of tritons against focal plane position spectrum, shown in Fig. 5.7. Shown in the figure is the Hoyle state for ^{12}C. This emphasizes the different analyzing techniques that can be adopted in the energy resolution improvement during the offline analysis. In Fig. 5.7 the relative TOF has been shifted to cover the range between -60 ns and 60 ns in order to have a zero as reference point. Figure 5.7(a) shows the spectrum before the lineshape

correction has been performed. It can be seen that the locus is sloped forward, the energy resolution of this locus is 104 keV. Figure 5.7(b) shows the spectrum after the correction has been performed and the locus appears to be straight. The energy resolution after the lineshape correction is 28 keV, thus the resolution has improved by as much as 76 keV.

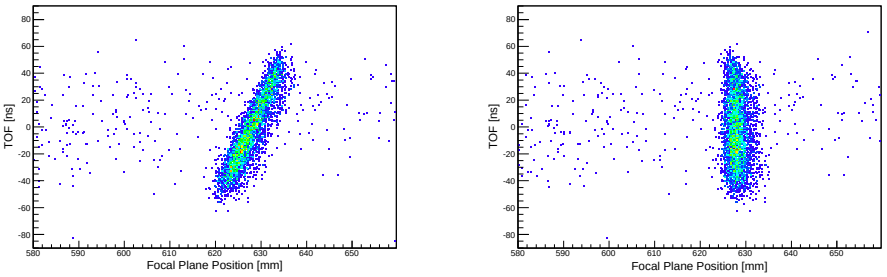

(a) (b)

Figure 5.7: Two-dimensional plots of relative TOF of tritons versus the focal plane position, before (a) and after (b) the lineshape correction has been performed.

5.3.5 K600 Energy Calibration

In order to obtain the ^{12}C excitation energy spectrum, the focal plane position spectrum shown in Fig. 5.6 needs to be converted into an excitation energy spectrum. The principle underlying the energy calibration of the K600 magnetic spectrometer has been given previously in section 4.8. Precisely known states in ^{12}C were used in the calibration process. Table 5.2 shows the ^{12}C states used and their corresponding focal plane position obtained by fitting peaks using the Gaussian function.

^{12}C state [MeV]	Focal Plane Position [mm]
16.105	94.69
15.110	177.11
14.083	260.98
12.71	376.65
9.641	632.63

Table 5.2: Focal plane position calibration data used to calibrate the (p,t) measurement.

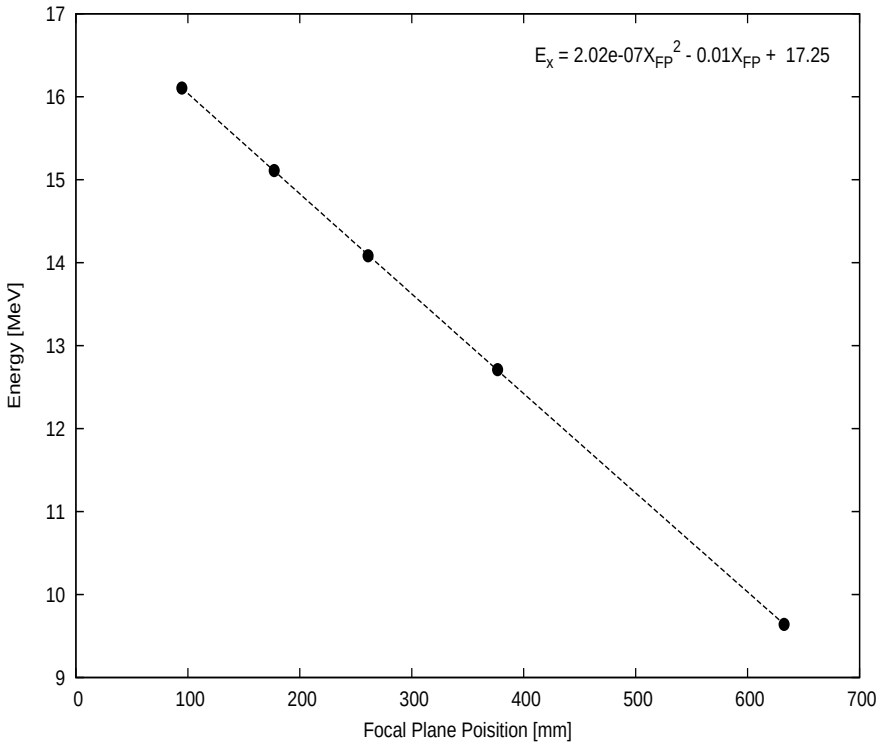

Figure 5.8: Second order polynomial fit of excitation energy as a function of focal-plane position (X_{FP}) for several known states of ^{12}C. The quadratic equation obtained is also shown.

5.4 Background Investigation

It was already emphasized in section 3.8.2 that because protons and tritons have different rigidity, the effect of beam halo is expected to be minimal in the present measurement. There are, however, contaminants in the target (see section 3.7). The (p,t) reaction on these nuclei may lead to population

of states in the region of interest. Characterization of the ^{14}C target showed trace quantities of Hydrogen, Carbon, Nitrogen, Oxygen, Chromium as well as Tantalum [56]. Kinematics calculations for the stable isotopes of these contaminants were performed to see if they would interfere in the excitation energy region of interest.

Table 5.3 shows the reactions investigated as well as their respective ground state Q-values. It is expected that the most prominent peaks from these reactions should be the ground states. Thus, no excited states were investigated. Also shown in column 4 are the anticipated triton energies of the ground states. The energies at which the peaks are expected in the ^{12}C excitation energy spectrum are shown in column 5. Negative energy values indicate that the reaction Q-value exclude the reaction to have its ground state in ^{12}C excitation energy spectrum. Figure 5.9 shows a simplified ^{12}C excitation energy spectrum showing several known ^{12}C levels from the ground state to 16.105 MeV (black). Also shown are lines (red) illustrating where the ground states from the different contaminants are expected. It is evident that none of these contaminants are expected to populate a ground state at the energy region of interest, i.e. $E_x \sim 10$ MeV. Only the ^{11}C ground state is the contaminant in the close proximity, i.e 10.75 MeV. The other state in this region is from ^{50}Cr$(p,t)^{48}$Cr reaction which is expected at $E_x \sim 8.57$ MeV. If populated, this state can be easily spotted as it will appear as a slopped locus in the 2D spectrum of TOF versus the focal plane position because of the mass difference between ^{14}C and ^{50}Cr nuclei. Furthermore, the excited states of ^{13}C nucleus are very narrow states [23] and could not be confused with the broad states in the 10 MeV excitation energy region in ^{12}C.

Target	Reaction	Q-value [MeV]	Triton energy [MeV]	Projected ^{12}C E_x [MeV]
Carbon	^{14}C$(p,t)^{12}$C	-4.641	58.05	0
	^{13}C$(p,t)^{11}$C	-15.19	48.27	10.75
	^{12}C$(p,t)^{10}$C	-23.36	40.63	19.07
Oxygen	^{16}O$(p,t)^{14}$O	-20.40	43.93	15.49
	^{17}O$(p,t)^{15}$O	-11.33	52.49	6.14
	^{18}O$(p,t)^{16}$O	-3.706	59.68	-1.80
Nitrogen	^{14}N$(p,t)^{12}$N	-22.14	42.07	17.49
	^{15}N$(p,t)^{13}$N	-12.90	50.73	8.07
Chromium	^{50}Cr$(p,t)^{48}$Cr	-15.10	50.27	8.57
	^{52}Cr$(p,t)^{50}$Cr	-12.82	52.52	6.11
	^{53}Cr$(p,t)^{51}$Cr	-11.50	53.83	4.66
	^{54}Cr$(p,t)^{52}$Cr	-9.176	56.12	2.15
Tantalum	^{180}Ta$(p,t)^{178}$Ta	-6.063	59.70	-1.83
	^{181}Ta$(p,t)^{179}$Ta	-5.739	60.03	-2.18

Table 5.3: Calculated Q-values as well as the triton ejectile energies for the ground state from different anticipated contaminant reactions. Shown in column 5 are the energies at which these ground states are expected to appear in the ^{12}C excitation energy spectrum. All calculations were performed for a beam energy of E_{lab} = 66 MeV and laboratory angle of $\theta_{lab} = 21°$.

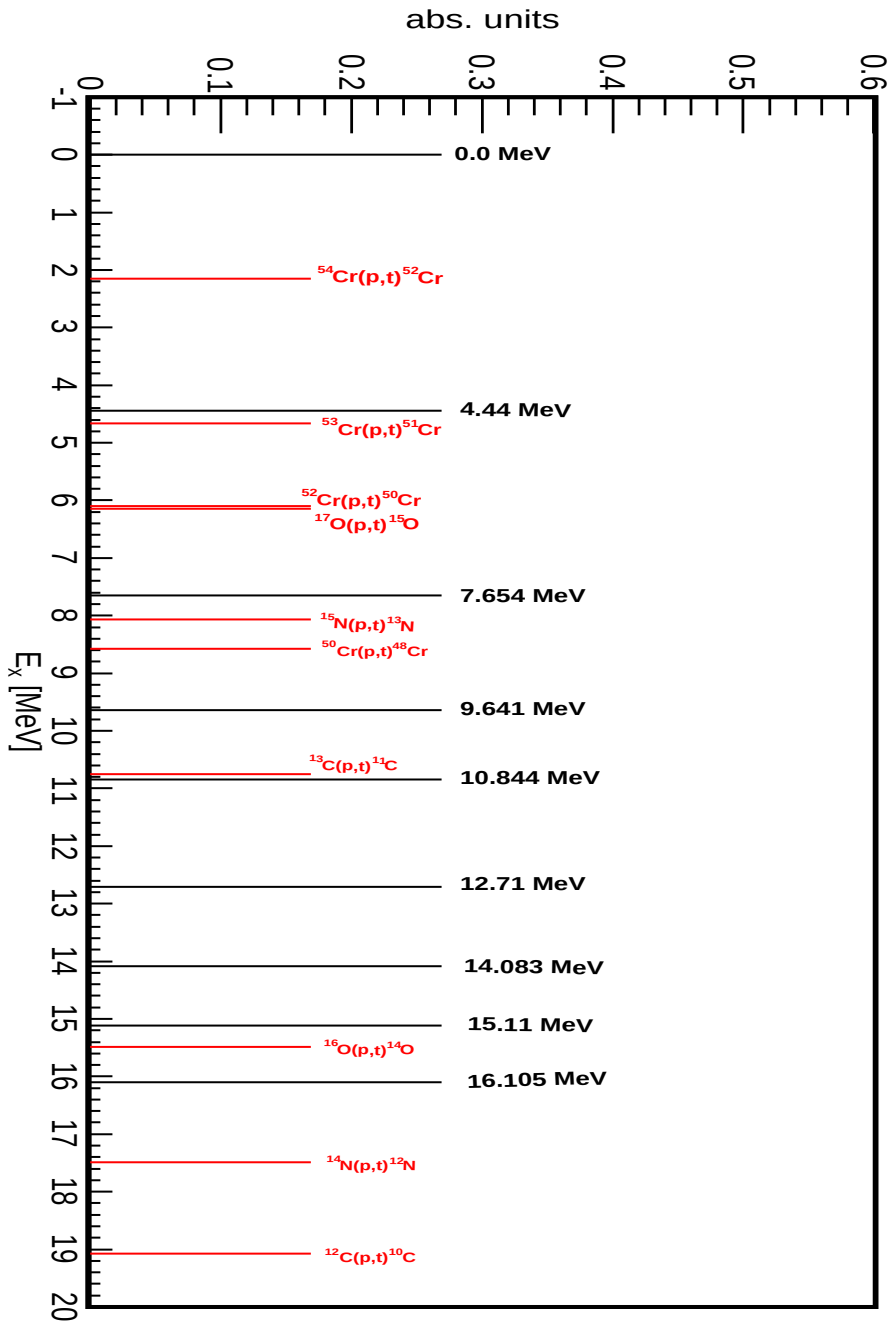

Figure 5.9: Illustration of the ^{12}C excitation energy spectrum showing the location of ground states of several contaminants.

5.5 Spectrometer-Silicon Coincidence

With singles event analysis completed, the coincidence events could be taken into account. Including coincidence information makes it possible to characterize the decay properties of the populated states in the ^{12}C nucleus. In order to extract coincidence events, the suitable types of coincidence needed to be chosen. Thereafter, a number of conditions are placed on the data. This section discusses the conditions imposed as well as how the events were chosen based on the efficiency.

5.5.1 Background Reduction Techniques

Since the spectrometer was used as the master trigger, with the silicon detectors in a slave mode, data were recorded for the silicon detectors for every event. It is therefore possible for the silicon detectors to record background events in coincidence with tritons leading to random coincidences. Random coincidences are events of which particles originating from different reactions are detected in the same time window and recorded as events from the same reaction. Events resulting from the same reaction are referred to as true coincidences. The random coincidences can be caused by different scenarios:

- Elastically scattered protons from the beam.
- Compton scattering of γ-rays. Almost all ^{12}C excited states are open to γ-decay (the 4.44 MeV state decays 100% through γ emission). As a result it is possible that γ-rays emitted by the decaying states can be detected in coincidence with the tritons resulting in coincidence events.
- β-decay background. Any reaction that leads to the activation of neutrons could result in a β-decay. The neutron activation can happen in the target material or any material in the chamber (if the beam is not properly aligned on the target).

- Electronic noise and other events from different beam packets.

Several techniques were employed in order to reduce the effects of random coincidence events on true coincidence events.

Silicon Detectors Strips Low-Energy Cutoff

Firstly, in order to take out the low energy background as well as the electronic noise during the data analysis, lower limits are enforced for the ADC data of each detector strip. The cutoff is properly chosen for each strip to cut away the majority of the low energy background, electronic noise and pedestal values. The pedestal comes from a voltage offset added at the ADC level. Figure 5.10 shows an uncalibrated ADC spectrum for a single strip. From the figure it is visible that below ADC channel 300 the information is dominated by the pedestal. In order to clean out the data for this particular strip, the cutoff should be applied at ADC channel 300 in the analyzing software, as indicated with the dashed line.

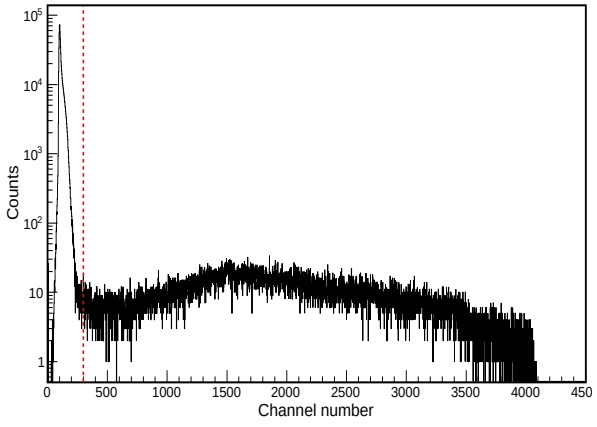

Figure 5.10: Uncalibrated ADC spectrum for a single silicon strip before the low energy cutoff (low energy cutoff shown with red dashed line) was applied.

Timing Spectra

The coincidence events are recorded within a TDC time window of 2 μs. As already emphasized, it is possible that within this time range, events recorded by the silicon array can also be due to random coincidences. In order to perform analysis for only true coincidences, efforts were made to reduce the contribution of random coincidences by applying a gate on the true coincidence events in the TDC spectrum as shown in Fig. 5.11. This time gate will remove nearly all random coincidences, mainly the events from different beam packets. A quick estimate showed that after this procedure there will still be roughly $\sim$8% random coincidences.

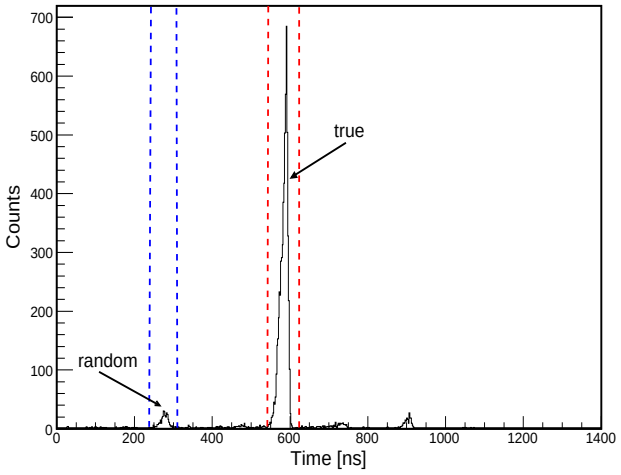

Figure 5.11: A typical time spectrum showing how gates can be applied in order to reduce the effects of random coincidence (blue) from real coincidences (red).

An illustration of how applying the time gate would affect the random coincidence to real coincidence ratio is shown in Figs. 5.12 and 5.13, where the focal plane position spectra for singles events and three different coincidence events are shown[4]. Figure 5.12 shows spectra produced with no time gate imposed on the data whereas the spectra shown in Fig. 5.13 was produced with

[4]Since two different triton field sets were covered in the present measurement, only one field set data were considered in these spectra which represents only half of the data.

the time gate imposed. In the figures peaks that belong to ^{12}C are indicated. Also indicated with arrows are the peaks are the contaminant peaks, namely the ground states of ^{11}C and ^{14}O.

It is expected that for coincidence events the strength of these contaminant peaks should weaken with an increase in the number of coincidence particles imposed by the analysis software. This is because these peaks result from the detection of tritons in coincidence with only the recoiling ^{11}C or ^{14}O nuclei. Hence, these peaks are expected to be strong specifically in the double coincidence events. However, for triple and quadruple coincidence events, the presence of these peaks will be resulting from random coincidence events where a triton was detected in coincidence with ^{11}C or ^{14}O nuclei and one or two randomly detected particles for triple and quadruple coincidence events respectively. Therefore, by imposing the timing gate one would expect the strength of these peaks in triples and quadruples to decrease drastically. This is evident in Fig. 5.13. The presence of the contaminants in these spectra is due to the 8% random coincidence remained after the time gate has been applied.

5.5.2 Silicon Detectors Detection Efficiency

The experimental detection efficiency ϵ_{sil}, the ability of the detection system to detect α-particles in coincidence with the tritons, was optimized using Monte Carlo simulations. The simulations were performed during the preparation of the experiment using the *SimSort* code. The code allows for the reaction and number of particles detected to be simulated in the excitation energy region of interest. The geometrical orientation of the detectors can be varied while investigating the detection efficiency. The best setup is chosen when the best possible efficiency is obtained. The code calculates efficiency as follows,

$$\epsilon_{sil} = 100 \times \frac{Number\ \ of\ \ Entries}{Number\ \ of\ \ generated\ \ events}\ , \tag{5.1}$$

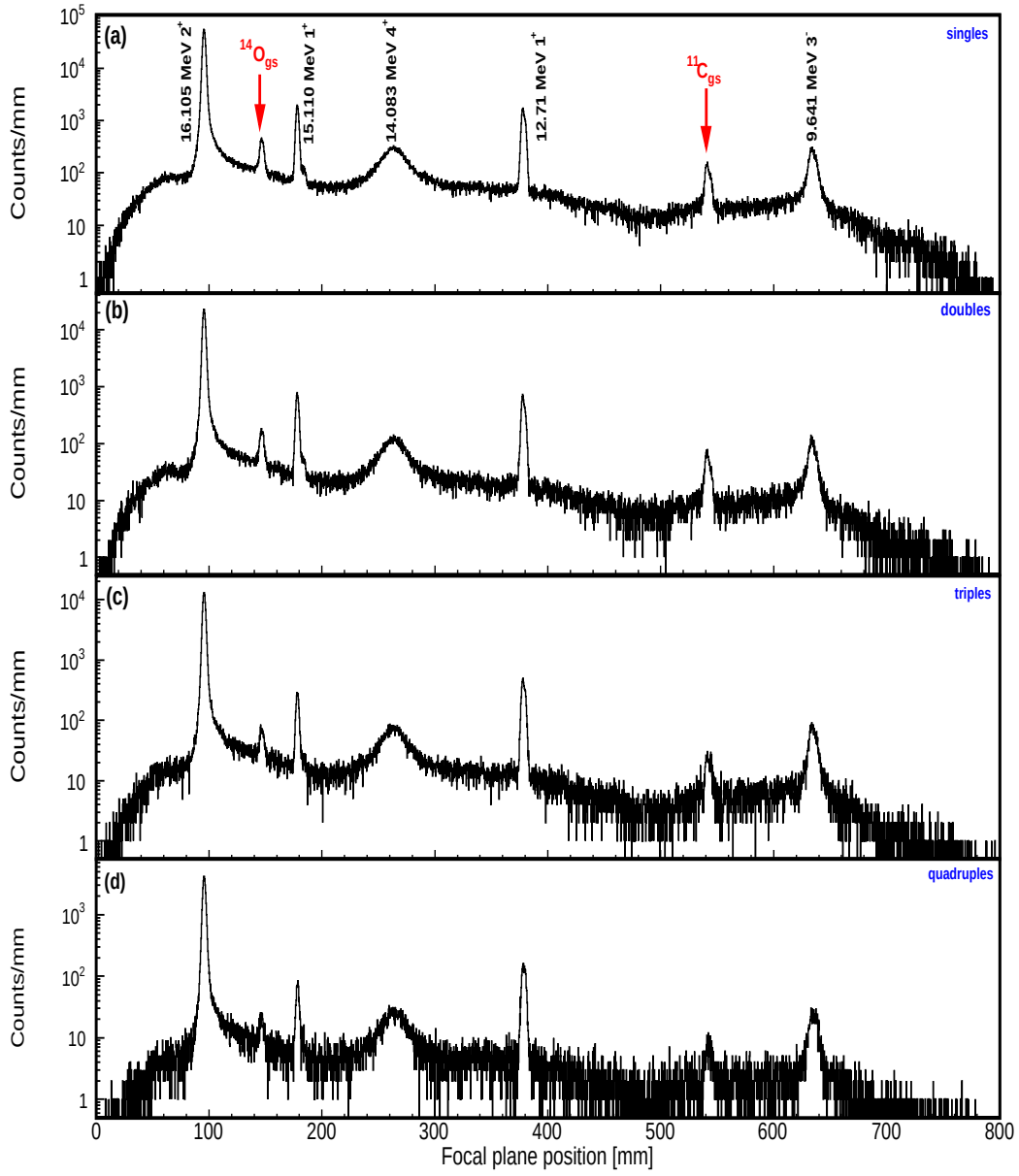

Figure 5.12: The focal plane position spectra for K600 only events (a) as well as different types of coincidences indicates (c - d). The coincidence events spectra were generated with no time gate applied.

where *Number of Entries* denotes number of events required to complete the simulation and *Number of generated events*, denotes number of events generated by *SimSort* in order to complete the simulation. Different types of coincidence can be simulated. For this measurement, three types of coincidence were simulated, namely double coincidence (events where a triton and

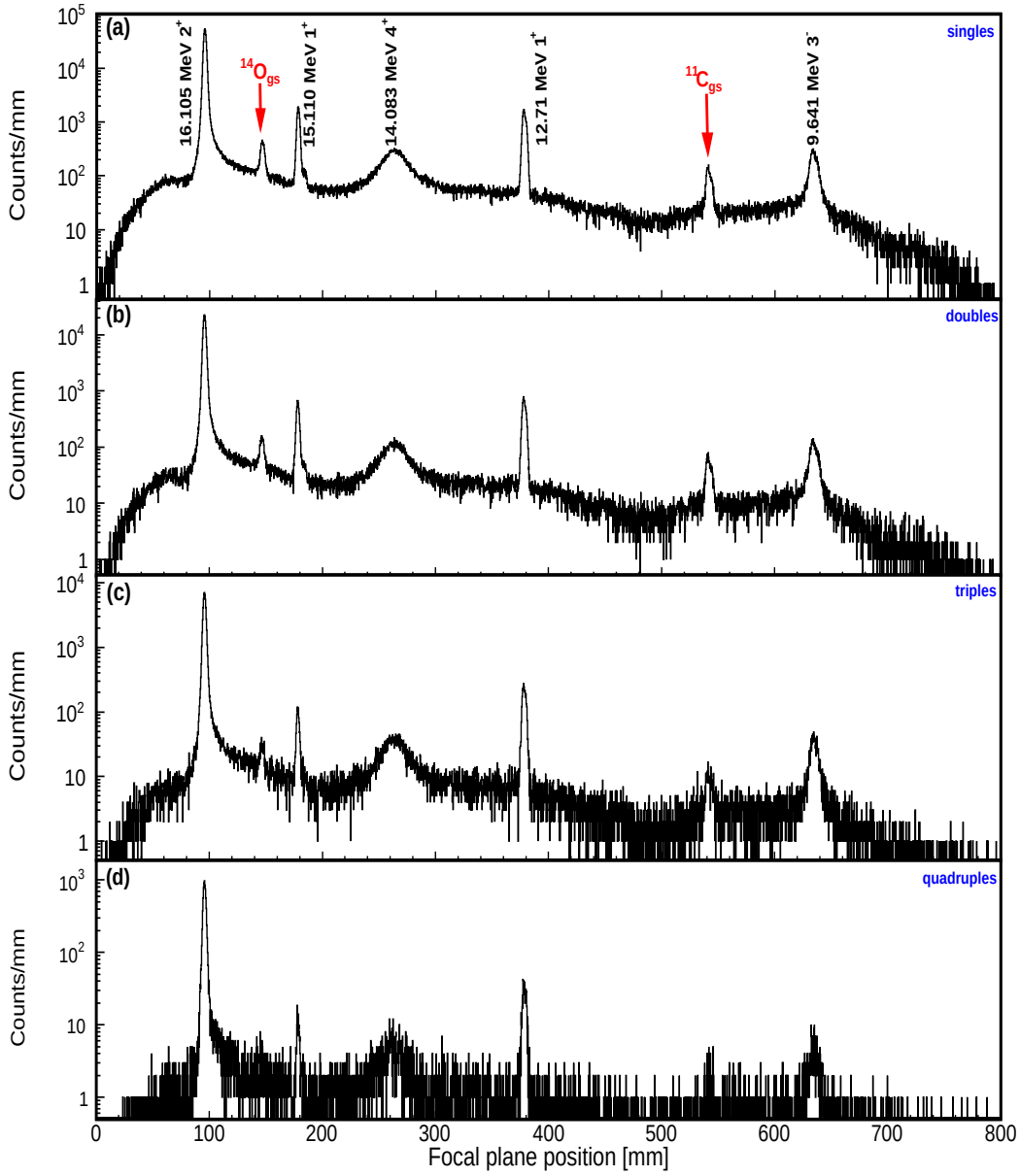

Figure 5.13: The focal plane position spectra for K600 only events (a) as well as different types of coincidences indicates (c - d). For coincidence events spectra were generated with the time gate imposed to data (see text).

one α-particle in coincidence are recorded), triple coincidence (events where a triton and two α-particles in coincidence are recorded), and quadruples coincidence (events where a triton and three α-particles in coincidence are recorded). For the final setup the double, triple, and quadruple coincidence events detection efficiency in the 10 MeV excitation energy region were, 33%, 14%, and 3%

respectively.

From efficiency values represented above, it is evident that the detection efficiency for four particles in coincidence is low compared to the other configurations. Therefore, the double and triple coincidence events were used in the analysis performed in the present study. Assuming that the particle(s) detected in the silicon array are α-particle(s), the physical information of the missing particle can be calculated using momentum and energy conservation.

5.5.3 The Total Final State Kinetic Energy Spectrum (TKE)

In the measurement performed in this study, the energies of α-particles originating from the decay of excited ^{12}C nuclei did not have enough energy to punch through the silicon detectors. For this reason the standard $\Delta E - E$ identification method could not be employed. Other methods were therefore employed. One such method uses the total final state kinetic energy (E_{TKE}) spectrum, as discussed below.

The code *SimSort* (see appendix D) was used to reconstruct the missing particle using energy and momentum conservation. When the information about the missing particle is obtained, the total final state kinetic energy is calculated. For the analysis performed in this study, there are 4 particles in the final state, namely the triton and three α-particles from the decaying ^{12}C nucleus. For this event the total final state kinetic energy of all the particles is calculated as follows;

$$E_{TKE} = E_{beam} + Q_{reaction} + Q_{break-up} \ , \tag{5.2}$$

where, E_{beam} is the beam energy (66 MeV), $Q_{reaction}$ in the primary reaction Q-value, and $Q_{break-up}$ is the Q-value of the ^{12}C break up into three α-particles. The calculated Q-values are -4.64 MeV and -7.35 MeV for reaction and breakup respectively. This leads to a value of $E_{TKE} = 54.08$ MeV. An E_{TKE} spectrum

from double coincidence events is shown in Fig. 5.14. This spectrum was obtained by summing the energies of the final state particles. Several peaks resulting from other different decay modes can be seen. The peak on the right hand side is consistent with the E_{TKE} of events with four particles in the final state. By gating on the peak, as shown with the red dashed lines, only events in which the ^{12}C exclusively decay into three α-particles are selected. By applying this gate, events where only alpha particle(s) were detected in the silicon detectors can be selected. It should also be noted that this method can also reduce the effects of random coincidence in the real coincidence peak.

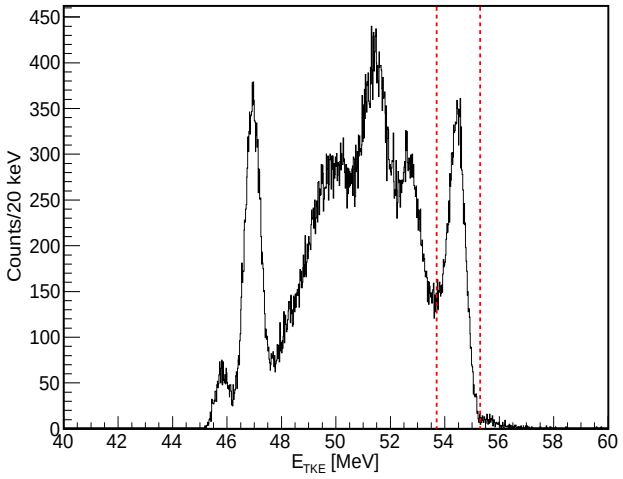

Figure 5.14: Experimental total final state kinetic energy spectrum. The isolated peak represents events of which the excited recoil ^{12}C nucleus exclusively decays into three α-particles through ^{8}Be$_{gs}$ decay channel.

It is expected that imposing both time and E_{TKE} gates would minimize the random coincidence to real coincidence events ratio. This is because by applying the E_{TKE} gate one explicitly chose events which the excited ^{12}C nucleus decay via α emission. This will get rid of all other decay modes and random coincidence which remained after imposing the time gate. Hence, the contaminants peaks are expected to vanish after imposing the E_{TKE} gate. This is illustrated in Fig. 5.15.

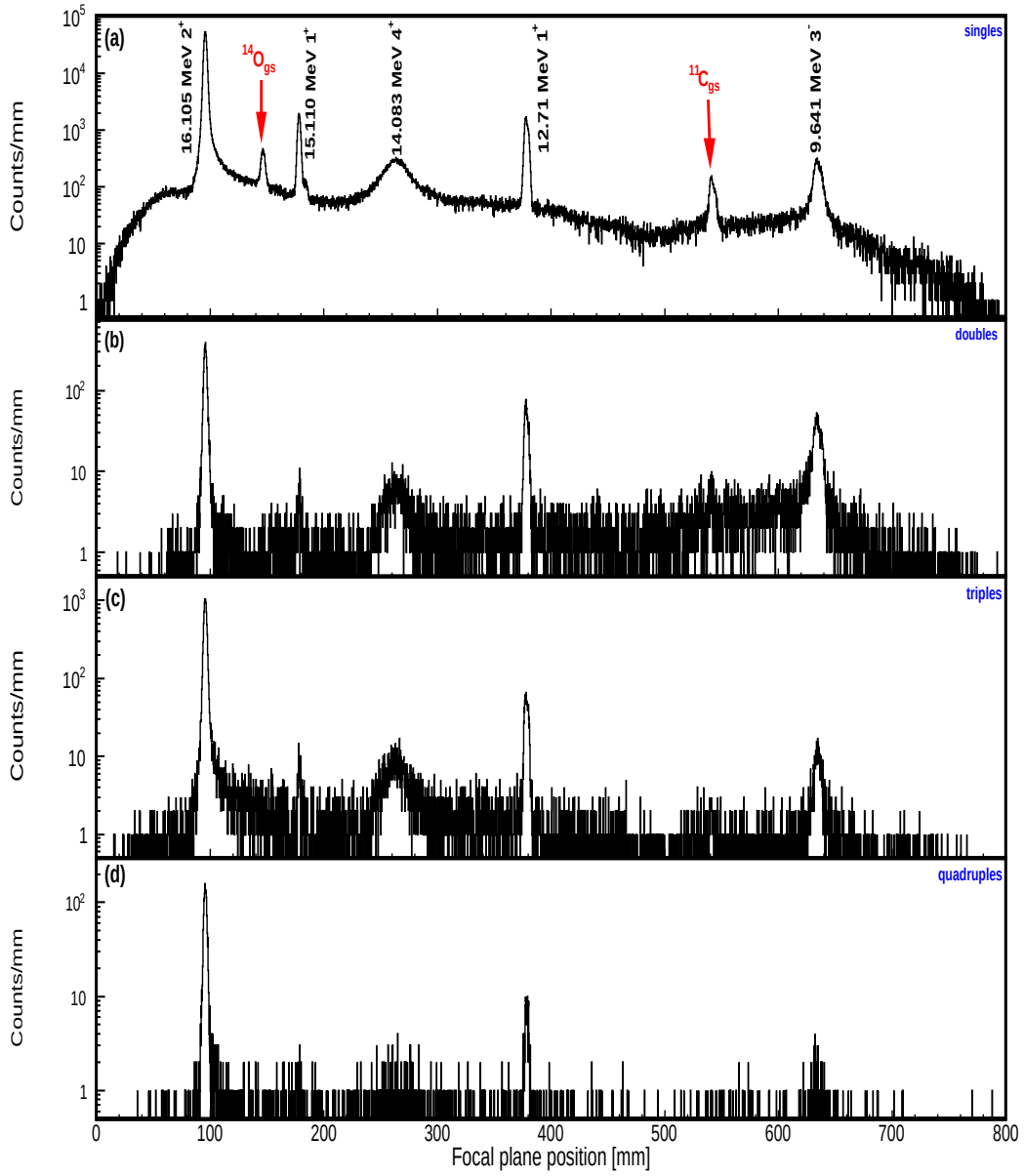

Figure 5.15: The focal plane position spectra for K600 only events (a) as well as different types of coincidences indicates (c - d). For coincidence events spectra were generated with both time and E_{TKE} gates imposed to data.

5.5.4 Determining the Relative Energy $E_{\alpha\alpha}$ between α-particles

Having selected the required events, the information about how the excited ^{12}C nucleus decayed can be obtained. Since the ^{12}C states to be investigated in this study may break up via α-particles, it is necessary to obtain information about

the intermediate ^{8}Be nucleus. Intermediate nuclei are nuclei that subsequently decays prior to the final state. For the ^{14}C$(p,t)^{12}$C$[3\alpha]$ reaction, the excited ^{12}C nucleus can decay into three α-particles through two different decay paths, namely the sequential and the direct (also known as democratic) decay, as illustrated in Fig. 5.16. The sequential decay, however, happens in two ways, namely the decay through the ^{8}Be$_{gs}$ or through the ^{8}Be first 2^{+} excited state. If the decay happens sequentially, information about the intermediate ^{8}Be nucleus is required in order to distinguish the two decay channels.

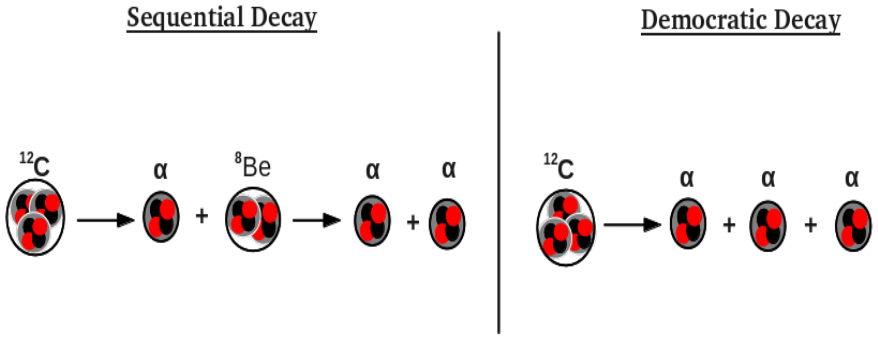

Figure 5.16: Schematic view of possible α-decay modes of the excited ^{12}C nucleus, namely sequential and democratic decay.

To construct information about the ^{8}Be nucleus, *SimSort* uses information obtained from the detected and the reconstructed missing particle. Suppose the sequential decay happens as follows: $^{12}\mathrm{C} \longrightarrow \alpha_1 + {}^{8}\mathrm{Be} \longrightarrow \alpha_2 + \alpha_3$. The index 1 denotes the first emitted α-particle while 2 and 3 denote the α-particles from the decaying ^{8}Be nucleus. To obtain the energy information of the ^{8}Be nucleus before it subsequently decays into α-particles, the relative energy between α_2 and α_3 can be calculated. This is illustrated in Fig. 5.17 where the spectrum for α-α relative energy for double coincidence events is shown. Different features are revealed from the figure. The narrow peak at $E_{\alpha_2\alpha_3} = 92$ keV (Q-value of ^{8}Be breakup) corresponds to breakup via the ^{8}Be$_{gs}$.

The broad bump above 0.2 MeV can represent several contributions: breakup through the $J^{\pi} = 2^{+}$ first excited state in ^{8}Be, breakup via the the democratic decay as well as decay through the ghost anomaly of the ^{8}Be ground state. A ghost anomaly refers to an anomalous peak that is associated with a level which exist close to a threshold, and that is well separated from other levels of the same spin and parity. In the description of such a state (see Chapter 6) the numerator in the resonance amplitude equation is increasing more rapidly than the denominator. The in-depth description of the ghost anomaly phenomenon can be found in Ref. [69, 70, 71]. Also included in the broad bump can be events resulting from the mis-reconstruction of the missing particles of the ground state decay mode[5]. The fact that the two break-up paths cannot be distinguished, i.e. the sequential via the ^{8}Be$_{2^{+}}$ and the democratic decay, is associated with the fact that the 2^{+} resonance in ^{8}Be has a very short lifetime. In Ref. [35], it was also pointed out that for low-lying states one could not simply separate the two decay paths.

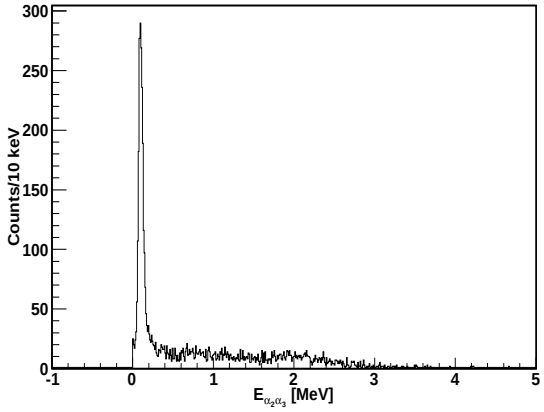

Figure 5.17: α-α relative energy ($E_{\alpha_1\alpha_2}$) spectrum for double coincidence events showing how one can obtain information about the intermediate ^{8}Be nucleus.

[5]The mis-reconstruction events are the results of the low angular resolution of the silicon detectors used. This leads to mis-reconstruction of the missing particle information. Simulations showed that only ∼3% of ground state events will affect other decay modes.

5.5.4.1 Monte Carlo Simulations Using *SimSort* Code

To better understand the experimental results obtained for the present measurement, the *SimSort* code was used to perform Monte Carlo simulations in the excitation energy region of interest. The simulated data can be used for quantitative comparison of experimental results to theory.

Using *SimSort*, one can simulate different decay channels. The user can define the exact nature of the breakup path for the purpose of the simulation: the excited state populated in ^{12}C and the decay path that it is expected to follow. *SimSort* assumes an isotropic center-of-mass (c.m.) distribution for each state [73].

In order to ascertain that the simulation performed mimicked the experimental measurement, the geometry of the detection setup used for simulation resembled the one used during the actual experimental measurement. The code also contained details of the calibration coefficients, detection threshold, the expected energy resolution, energy loss in the target, etc. Simulated and experimental data are saved in identical structures, i.e. ROOT files. This makes it possible to perform identical analysis in the two data sets. Thus, all gates applied to the real data were also applied to the simulated data.

The simulations were performed for doubles and triples and only the $^{8}\mathrm{Be}_{gs}$ decay channel was considered. The results of the simulated data will be presented in section 7.2.2.2.

Chapter 6

Theoretical Formalism

Different theoretical frameworks were used to interpret the experimental results obtained in the present study. In the procedure performed to fit the obtained excitation energy spectra, some resonance lineshapes were not reproduced using the normal distributions such as Gaussian and Lorentzian functions. This is due to the effects of the centrifugal barrier which affect the formation and decay of these resonances [74]. Thus, the penetrability factor needs to be accounted for in the definition of these resonance distribution functions. These effects are expected to be strong near the decay threshold for $l \neq 0$ resonances [75], where l is the angular momentum of the resonance. More detailed clarification on how the centrifugal barrier affect the resonance's decay width, lineshape, and production amplitudes can be found in Refs [75, 76]. In order to generate these resonances, a suitable model which takes the penetrability into account was employed. For this purpose the one-channel R-matrix theory was used. The formulation used is discussed in section 6.1.

Since the aim of the complete kinematics measurement was to locate the 2^+ excitation of Hoyle state, efforts were made to investigate the angular distribution of the reaction of interest. This is done in order to investigate laboratory angles which favor the enhancement of 2^+ states compared to other states. To calculate the angular distributions, the coupled-channels Born approximation

(CCBA) method was used. Section 6.2 is aimed at providing the formulation used in these calculations.

6.1 Single Channel R-Matrix Theory

The R-matrix theory was first introduced by Thomas and Lane in the 1950s [77], and it has been successfully used to study resonance excitations in nuclear reactions. In nuclear reactions that proceed via the formation of a compound nucleus, R-matrix theory can be used to extract information of the states populated in the compound nucleus.

Since its inception, different types of the R-matrix were introduced and successfully used to study distinct types of nuclear reactions. In depth description of different types of R-matrix and their applications can be found in Ref. [78]. As already mentioned, in the present study the single channel R-matrix theory is used to generate near α-decay threshold resonances.

The experiments described within this thesis involves the transfer reactions of that have the form:

$$A + a \rightarrow b + B \; ; \qquad B \rightarrow C + c \; . \tag{6.1}$$

In the reaction denoted above, the compound nucleus is formed in a state unstable to particle decay, thus it can decay into two products as denoted by $B \rightarrow C + c$ notation. From the one-channel R-matrix definition of Ref. [77], the resonance amplitude $f(E)$ can be calculated as:

$$f(E) \;\; = \;\; \mathcal{K} \frac{\Gamma_c}{(E_{res} - E - \Delta)^2 + \Gamma_c^2/4} \; , \tag{6.2}$$

where E_{res} is the resonance energy, and E the energy in the center-of-mass and $\mathcal{K}$ is a normalization constant. The resonance width is defined as:

$$\Gamma_c \;\; = \;\; 2P_l(E)\gamma_c^2 \; , \tag{6.3}$$

where $P_l(E)$ is the barrier penetrability factor for the given orbital angular momentum l. The reduced width amplitude γ_c^2 is the Wigner limit defined as,

$$\gamma_c = \sqrt{\frac{3\hbar}{2\mu a_c^2}}\ , \tag{6.4}$$

where a_c is the channel radius and μ is the reduced mass. The level shift Δ is given by,

$$\Delta = \gamma_c^2(S_l(E) - \mathcal{H})\ , \tag{6.5}$$

where $S(E)$ is the shift function for the given orbital angular momentum l, and $\mathcal{H}$ is the boundary condition defined as value of $S_l(E_{res})$, where

$$S_l(E) = \frac{\rho(FF^{'} + GG^{'})}{F^2 + G^2}. \tag{6.6}$$

where $\rho = kR$ and F, G, $F^{'}$, and $G^{'}$ are respectively the regular and irregular Coulomb wave functions and their derivatives, respectively.

In the present study, the structure of the ^{12}C nucleus were investigated using the ^{11}B(^{3}He,d) and ^{14}C(p,t) reactions. Above the α-decay threshold the excited ^{12}C nucleus is open to α emission. Here the states to be generated with Eq. (6.2) are supposed to decay sequentially via the $^{12}\mathrm{C} \rightarrow {}^{8}\mathrm{Be} + \alpha$ channel. These states are the 9.641 MeV 3^- and the 2^+ state (its location is varied until best fit is obtained).

Figure 6.1 shows the typical 3^- (black) and 2^+ (red) states generated using Eq. (6.2) as was the case in Ref [27, 30]. The 3^- state was generated with E_x = 9.641 MeV and the 2^+ resonance is used is the one reported in Ref [30], which is located at E_x = 9.75 MeV. For the 3^- state we use l = 3 and the reduced width amplitude used is 25% of the Wigner limit while for the the 2^+ state l = 2 and the reduced width amplitude was set to equal to the Wigner limit. The channel radius was set to R = $1.34(8^{\frac{1}{3}} + 4^{\frac{1}{3}})\ fm$ for both states. The asymmetric shapes of these resonances are due to the effect of both Coulomb and centrifugal barriers.

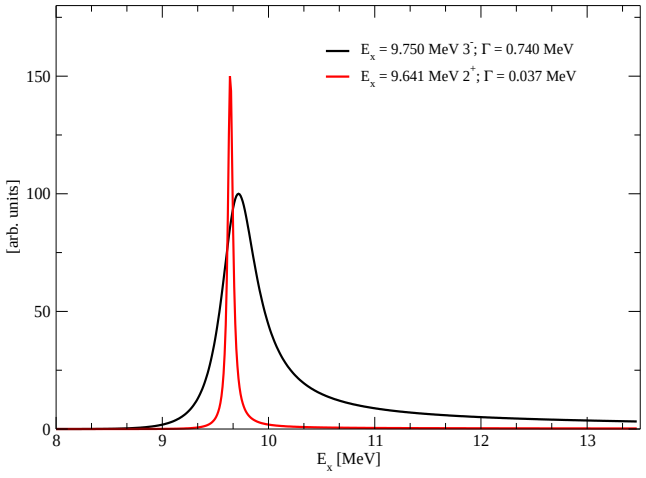

Figure 6.1: R-matrix generated resonances for the 9.641 MeV 3^- state (red) and the assumed 9.750 MeV 2^+ state in ^{12}C nucleus.

6.2 Coupled-Channels Born Approximation

To calculate the angular distribution in the complete kinematics measurement, the coupled-channels Born approximation (CCBA) method was used. Together with the distorted wave Born approximation (DWBA), the CCBA method is most frequently used to interpret and analyze the direct reactions data.

In the study of direct reactions, two-nucleon transfer is significantly more complicated than single-nucleon transfer. The underlying mechanism can be more complicated: two-step sequential transfer can contribute in addition to the direct path, therefore the DWBA eventually becomes an inappropriate model to use. To handle these scenarios, the DWBA approach needs to be extended to the CCBA model. The CCBA allows the two-step transfer approach including inelastic excitation of target, projectile or residual nuclei, as depicted in Fig.6.2. Shown in the figure are the possible transitions for an A(a,c)C reaction assumed to proceed through a two-step process A(a,b)B(b,c)C as well as the coupling between levels (indicated with red arrows). The CCBA model encapsulates the DWBA model and Couple-Channel (CC) equations. The

complete detailed formalism underlying these models are given in Ref. [79].

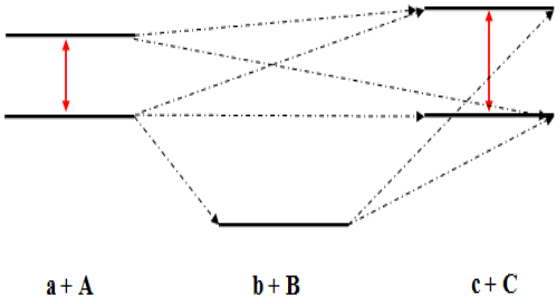

Figure 6.2: A schematic representation of the multi-step process showing the simplified CCBA coupling scheme to handle the A(a,c)C reaction.

In the CCBA calculations, the differential cross section for any A(a,c)C reaction has the DWBA form [79]:

$$\frac{d\sigma_{\beta\alpha}}{d\Omega} = \frac{\mu_\alpha \mu_\beta}{(2\pi\hbar^2)^2}\frac{k_\beta}{k_\alpha}\sum_{M_A M_C m_a m_c} |T^{CCBA}_{M_A M_C m_a m_c}(\mathbf{k}_\beta, \mathbf{k}_\alpha)|^2 \ , \tag{6.7}$$

where $\beta = a$ + A and $\alpha = c$ + C represent the entrance and exit partition respectively, μ is the reduced mass and k is the wave number for the partition. The mass of the target nucleus, residual nucleus, projectile and ejectile are respectively denoted as, M_A, M_C, m_a and m_c. The CCBA transition amplitude has the form [79],

$$T^{CCBA} = \sum_{\beta\alpha} \langle \chi^{(-)}_\beta \psi_\beta | U | \chi^{(+)}_\alpha \psi_\alpha \rangle \ , \tag{6.8}$$

where $\chi^{(-)}$ and $\chi^{(+)}$ represent the distorted waves and ψ_β and ψ_α are respectively the entrance and exit partition wave functions. The complex optical model potential $U(r)$ represents the particle-nucleus interaction and is defined as:

$$U(r) = V(r) + iW(r) \ , \tag{6.9}$$

where the real part potential is responsible for scattering and the imaginary part stands for the absorption. The standard form of the potential is as follows:

[80]:

$$U(r) = U_C(r) + U_R(r) + iW(r) + U_{so}(r) \ , \tag{6.10}$$

where,

$$\begin{aligned} U_C(r) &= \frac{zZe^2}{2R}[3 - \frac{r^2}{R^2}] \ , \qquad r \leq R \ , \\ &= \frac{zZe^2}{r} \ , \qquad r \geq R \ , \text{ is the Coulomb potential,} \end{aligned}$$

$$U_R = -V_R f_R(r) \ , \text{ is the real central volume potential of the depth } V_R,$$

$$W = 4a_i W_D \frac{df_i(r)}{dr} \ , \text{ is the imaginary central surface potential of the depth } W_D,$$

$$U_{so} = \left(\frac{\hbar}{m_\pi C}\right)^2 V_{so} \frac{1}{r} \frac{df_{so}}{dr} l \cdot s \ , \text{ is the surface spin-orbit potential of the depth } V_{so},$$

$$f_R(r) = \left[1 + exp\left(\frac{r - R_x}{a_x}\right)\right]^{-1} \ , \text{ is a Saxon-Woods form factor.}$$

The radii of the nuclei used in these equations are given as,

$$R = rA^{1/3} \ . \tag{6.11}$$

To investigate the angular distribution of the outgoing triton from the ^{14}C$(p,t)^{12}$C reaction, the cross sections were calculated using the FRESCO code [81]. Fresco is a coupled-channels nuclear reaction code, written by Ian Thompson. It can also be used in analyzing nuclear reactions in terms of the DWBA method.

In the present work, only two states in ^{12}C nucleus are considered, the angular distribution to the $J^\pi = 2^+$ 4.44 MeV state and the $J^\pi = 0^+$ 7.654 MeV state. This is done in order to compare the cross sections of these states with respect to the center-of-mass angles.

To improve the calculations, the CCBA method was utilized in the present study to recalculate the triton angular distribution of the ^{14}C$(p,t)^{12}$C reaction

at a proton beam energy of $E_{lab} = 40.3$ MeV. Secondly, the calculations for $E_{lab} = 66$ MeV are performed.

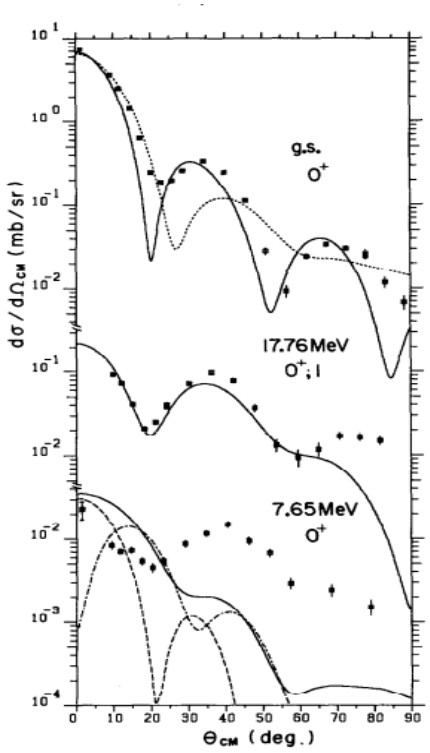

Figure 6.3: Angular distributions for the ^{14}C$(p,t)^{12}$C reaction leading to $J^{\pi} = 0^{+}$ states in ^{12}C, from Ref. [82]. From the bottom angular distribution it is visible that the calculations failed to reproduce the experimental measured cross sections.

The following ingredients are required to perform these calculations:

- Scattering potentials for $p + {}^{14}$C, $d + {}^{13}$C and $t + {}^{12}$C at appropriate energies.
- Binding potentials for $p + n$, $d + n$, $n + {}^{13}$C, ^{12}C $+ n$ and ^{12}C $+ 2n$.
- Spectroscopic amplitudes for different overlaps as shown in Fig 6.4.

In the CBBA calculations the following steps were included: two-step transfer reactions through the ^{14}C$(p,d)^{13}$C$_{gs}$ and ^{14}C$(p,d)^{13}$C$_{3/2^-}$ levels, coupling between ^{14}C 0^+_1 and 2^+_1 (and its re-orientation) states and the coupling between ^{12}C 0^+_1, 2^+_1 (and its re-orientation) and 0^+_2 states. Figure 6.4 gives the

detailed CCBA schematic view of all the processes included in the calculations.

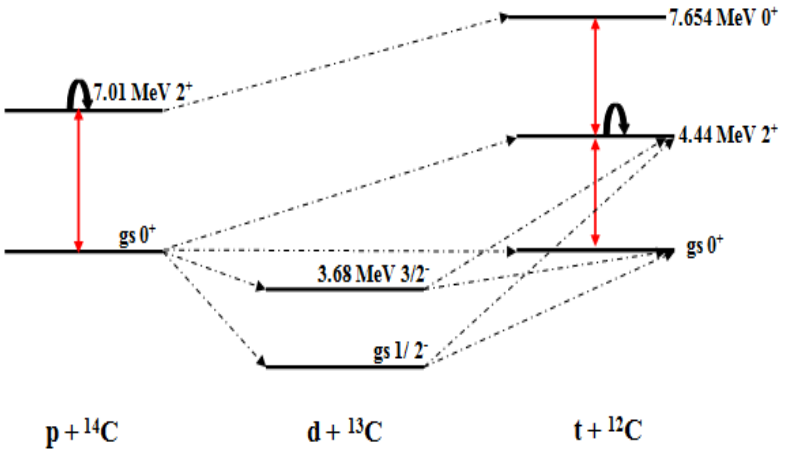

Figure 6.4: A schematic representation of multi-step process showing the simplified CCBA coupling scheme for the ^{14}C(p,t)^{12}C reaction. Red arrows represent the coupling between the states.

The scattering potentials used for the entrance and exit channels are the global potentials obtained using different methods. For the p + ^{14}C scattering, the potentials were obtained using the method described by Koning *et al.* [85]. For the d + ^{13}C scattering potentials, method from Daehnick *et al.* [86] was used, and for the t + ^{12}C scattering the Pang global potential [87] was used. Table 6.1 lists the potential parameters used for the 40.3 MeV calculations. The $2n$ form factors were calculated using the Bayman-Kallio method [88] from ^{13}C + n form factors using binding potentials and weights given in Ref. [82] and assuming binding energies half those of the final ^{12}C + $2n$ states. The spectroscopic amplitudes used for the overlaps were obtained from Ref. [89].

Figure 6.5 shows cross sections for the $J^{\pi} = 2^{+}$ 4.44 MeV (top panel) and the $J^{\pi} = 0^{+}$ 7.654 MeV (bottom panel) states for $E_{lab} = 40.3$ MeV calculations. The solid line represents the CCBA calculations whereas the experimental data points are represented by solid circles. From the figure, it is evident

System	V_R	r_R	W_R	a_R	W_D	r_D	a_D	V_{so}	r_{so}	W_{so}	a_{so}	r_C
$p + {}^{14}C$	43.2	1.14	4.39	0.68	6.01	1.30	0.53	4.91	0.92	-0.26	0.59	1.48
$d + {}^{13}C$	81.25	1.17	1.64	0.771	11.51	1.325	0.663	3.1355	1.07			1.30
$t + {}^{12}C$	113.9	1.09	3.38	0.83	15.00	1.26	0.819					1.29

Table 6.1: Global potential parameters used for the $^{14}C(p,t)^{12}C$ reaction cross section calculations for E_{lab} = 40.3 MeV. Depths, radii and diffuseness parameters are in MeV, fm, and fm, respectively.

that the CCBA calculations reproduce experimental cross sections better than the DWBA calculations performed in Ref. [82]. No enhancement factor was required to improve the calculations and its shape resembles the measured cross section. There is also obvious improvement in the calculation of the 0^+ 7.654 MeV state. As already mentioned in Chapter 1, this state is believed to have a well-developed α-cluster structure. The well reproduced experimental results may point out that perhaps the CCBA method can be used successfully to calculate the angular distribution of the cluster states.

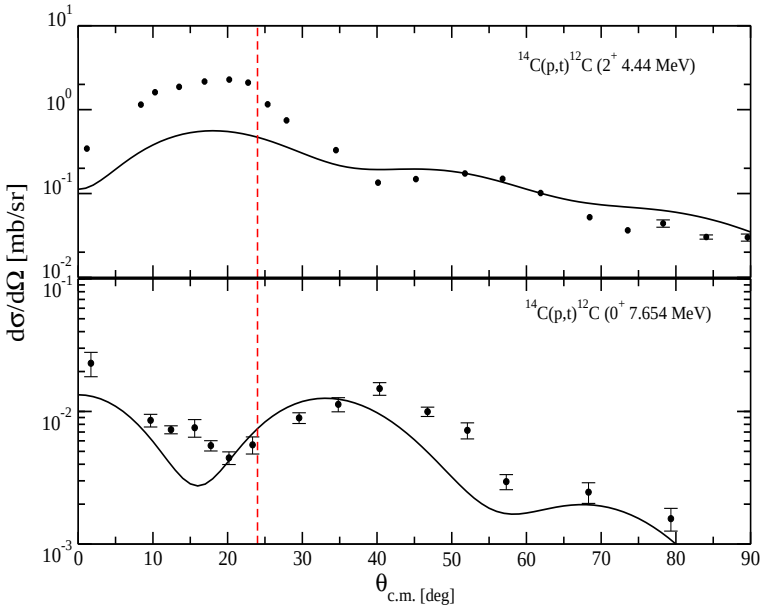

Figure 6.5: Angular distributions for the $^{14}C(p,t)^{12}C$ reaction leading to the 2^+ 4.44 MeV (top panel) and the 0^+ 7.654 MeV (bottom panel) states in ^{12}C for E_{lab} = 40.3 MeV calculations. The curves show the CCBA calculations and the the solid circles represent the measures cross section. The red dashed lines represent $\theta_{c.m.} \sim 24°$ which corresponds to $\theta_{lab} \sim 21°$ (see text).

With the CCBA method succeeding in reproducing the measured cross section for the E_{lab} = 40.3 beam energy, it was concluded that this method can be used successfully to calculate the angular distribution of tritons from the ^{14}C$(p,t)^{12}$C reaction for any beam energy. Therefore, the same method was utilized to calculate the angular distribution for the measurement performed with beam energy of E_{lab} = 66 MeV.

To perform these calculations similar ingredients used for the E_{lab} = 40.3 MeV calculations were used. With only the global potentials are expected to be different. Table 6.2 lists the potential parameters used for the E_{lab} = 66 MeV calculations. Figure 6.6 shows the cross sections for the $J^{\pi} = 2^{+}$ 4.44 MeV (top panel) and the $J^{\pi} = 0^{+}$ 7.654 MeV (bottom panel) states for E_{lab} = 66 MeV calculations. No measured cross sections are available for this energy, thus, only calculations are shown.

System	V_R	r_R	W_R	a_R	W_D	r_D	a_D	V_{so}	r_{so}	W_{so}	a_{so}	r_C
p + ^{14}C	35.11	1.14	7.36	0.68	6.01	3.54	0.53	4.43	0.92	-0.55	0.59	1.48
d + ^{13}C	74.05	1.17	4.69	0.818	9.181	1.325	0.663	2.7335	1.07			1.30
t + ^{12}C	110.	1.09	3.42	0.83	17.22	1.26	0.84					1.29

Table 6.2: Global potential parameters used for the ^{14}C$(p,t)^{12}$C reaction cross sections calculation for 66 MeV. Depths, radius and diffuseness parameters are in MeV, fm, and fm, respectively.

As already mentioned, the aim of the angular distribution calculations for the 0^{+} and 2^{+} states was to investigate how the population of these states vary with the center-of-mass angles. Thereafter, the angle at which the cross section to the 2^{+} state is higher compared to the 0^{+} state would be chosen. This was done in order to perform the measurement at an laboratory angle that enhances the population of the 2^{+} states while suppressing the population of the 0^{+} states. In Figs. 6.5 and 6.6, the suitable angle to achieve this goal lies at the center-of-mass angle of $\theta_{c.m.} \sim 15°$, which corresponds to the laboratory angle of $\theta_{lab} \sim 13°$. The measurement at this laboratory angle could not be performed due to the fact that one of the requirements of this measurement

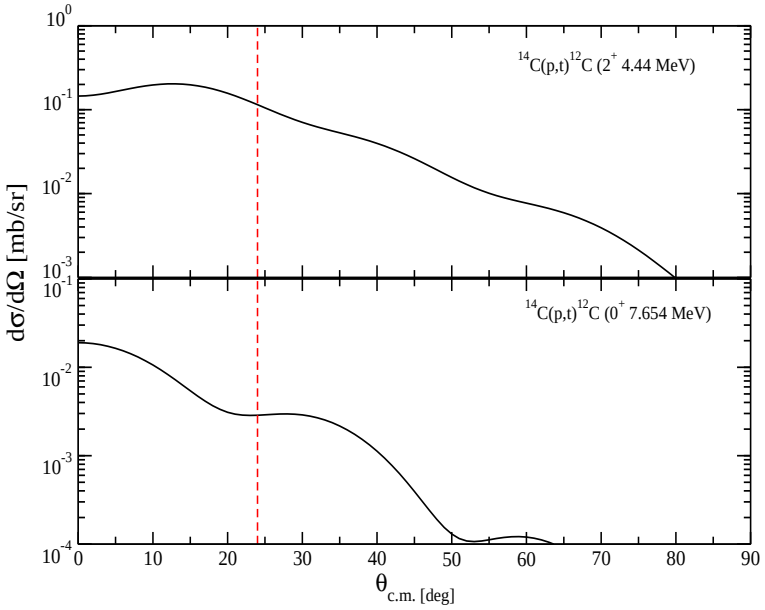

Figure 6.6: Angular distributions for the ^{14}C(p,t)^{12}C reaction leading to the 2^+ 4.44 MeV (top panel) and the 0^+ 7.654 MeV (top panel) states in ^{12}C for 66 MeV calculations. The curves show the CCBA calculations. The red dashed lines represent $\theta_{c.m.} \sim 24°$ which corresponds to $\theta_{lab} \sim 21°$ (see text).

was to perform a low background measurement. This requirement could be achieved by using the external beamstop. It has been already emphasized that the external beamstop can only be used in measurement performed at laboratory angles of $\theta_{lab} \geq 21°$. As a result another angle needed to be chosen. Thus, the measurement was performed at laboratory angle of $\theta_{lab} = 21°$ which corresponds to center-of-mass angle of $\theta_{c.m.} \sim 24°$, indicated by red dashed lines in Figs. 6.5 and 6.6. At this angle it expected that the effects of 0^+ states in the excitation energy region of interest will be minimized. Therefore, the signatures of the 2^+ state if populated could be observed.

Chapter 7

Results and Discussions

This chapter is dedicated to the presentation of the results of both ^{11}B(^{3}He,d)^{12}C and ^{14}C(p,t)^{12}C reactions.

7.1 (^{3}He,d) reaction

The primary goal of the (^{3}He,d) measurement was to investigate the existence of the 11.16 MeV state in ^{12}C. In the following sections, results are presented for the (^{3}He,d) measurement followed by a discussion thereof.

7.1.1 Excitation Energy of ^{12}C

The ^{12}C excitation energy spectrum from the ^{11}B(^{3}He,d)^{12}C reaction was extracted from the focal plane position spectrum using the calibration process described in section 4.8. Figure 7.1 shows the ^{12}C excitation energy spectra measured at three different laboratory angles, namely $\theta_{lab} = 25°$, $\theta_{lab} = 30°$ and $\theta_{lab} = 35°$. From the three laboratory angle measurements, it can be seen that there is a deep valley in the region where the 11.16 MeV state is expected. No clearly defined peak was seen in the original measurement [24], only a broad flat region with strength almost equal to the 10.84 MeV state was observed. The broad structure seen was interpreted to be a $J^{\pi} = 2^{+}$ state in ^{12}C located

at 11.16 MeV. Though the present measurement mirrored the experimental conditions reported in Ref. [24], the current dataset does not reveal any state at 11.16 MeV.

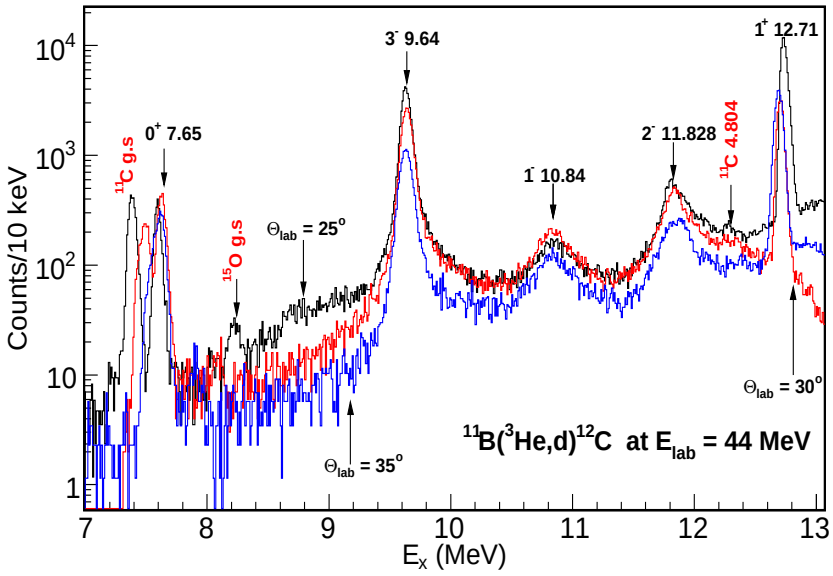

Figure 7.1: Excitation energy spectra for the ^{11}B(^{3}He,d)^{12}C reaction at laboratory emission angles of $\theta_{lab} = 25°$ (black), $\theta_{lab} = 30°$ (red) and $\theta_{lab} = 35°$ (blue).

7.1.2 Different Techniques to Investigate the Existence of the 11.16 MeV State

From Fig. 7.1 it is seen that the excitation energy spectra for all the laboratory angle measurements show no apparent evidence of the 11.16 MeV state. In further careful attempts to locate a state at 11.16 MeV, different techniques were employed in the present dataset.

The first technique involves a closer inspection of the ^{12}C excitation energy spectra around the 11 MeV region. The same technique was applied in Ref. [24], where several energy spectra of deuterons in the 11 MeV region were shown for different center-of-mass angles. These spectra showed an increase in strength of the reported 11.16 MeV state with an increase in center-of-mass

angles. The broad structure was seen in spectra for center-of-mass angles between $\theta_{lab} = 25°$ and $\theta_{lab} = 35°$. This was associated with the fact that the cross section of the populated 10.84 MeV state is low at these angles, while a 2^+ 11.16 MeV state is expected to be at its maximum [24]. Figure 7.2 shows the deuteron energy spectrum in the 11 MeV region for $\theta_{lab} = 25°$. This angle corresponds to the centre of mass angle $\theta_{cm} = 30°$ and it is at this angle where the clearest signature of the 11.16 MeV state was claimed in the original measurement (see Fig. 3 and Fig. 4, in Ref. [24]). This deuteron energy spectrum can be compared directly with the results in Ref. [24]. For the present dataset, the region where the 11.16 MeV state should be located, indicated with an arrow (red), a deep valley is visible adding to the conclusion that there is no 11.16 MeV state in ^{12}C.

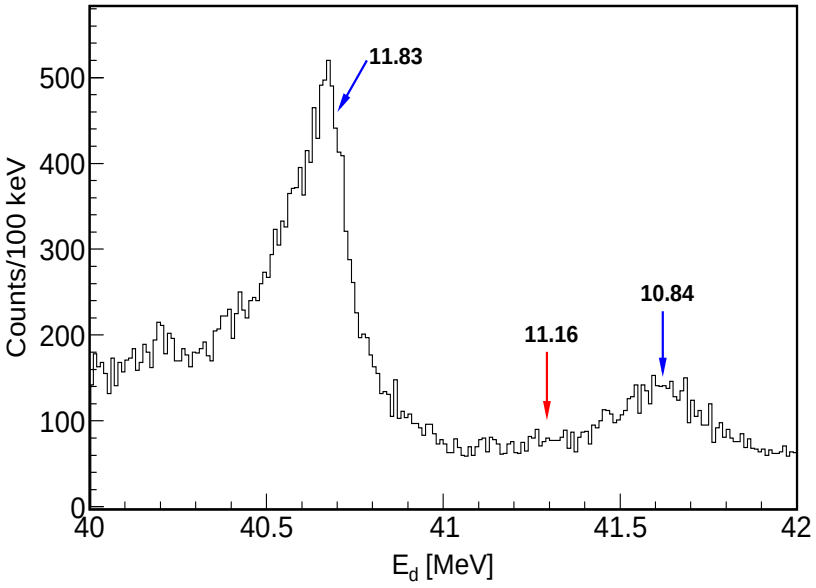

Figure 7.2: Energy spectrum of deuterons in the ^{12}C excitation energy region close to 11 MeV, for measurement performed at $\theta_{lab} = 25°$.

Another technique involves using the capabilities of modern equipment to yield not only focal plane position, but also angular information. Figure 7.3 shows the two-dimensional plot of deuteron emission angle versus ^{12}C excitation energy. Here, the spectrometer ion optics and data analysis lineshape

corrections have been optimized so that the ^{11}B(^{3}He,d)^{12}C reaction appears as vertical loci, while states from (^{3}He,d) reactions from target contaminants appear as sloped loci. The contaminant loci are either sloped right or left, depending on the relative mass being more or less than ^{12}C. The (^{3}He,d) reaction on heavier target nuclei (e.g. ^{14}N and ^{16}O) slopes forward, and conversely for lighter target nuclei (e.g. ^{10}B) slopes backward. The projection of this spectrum onto the horizontal axis yields the one-dimensional excitation energy spectrum of the data at $\theta_{lab} = 25°$, such as the one seen in Fig. 7.1. The overview given above can assist in determining whether the peak seen in one-dimensional spectrum belongs to the nucleus of interest or if it originates from a contaminant. A good example of a target contaminant peak comes from the ^{14}N(^{3}He,d)^{15}O reaction leading to the ^{15}O ground state, which appears at an excitation energy of 8.3 MeV in Fig. 7.1 and can be seen in Fig. 7.3 to be a locus with a slope. In the 11.16 MeV region in Fig. 7.3, no locus can be seen in this region stressing the fact that no state in this region was populated either from ^{11}B(^{3}He,d)^{12}C or other (^{3}He,d) reactions from target contaminants in this dataset.

Since the techniques employed are only of a visual nature, which is only qualitative, a quantitative analysis was required in order to arrive at a final conclusion. The single channel R-matrix formalism (discussed in Chapter 6) was used to analyze aspects of the present (^{3}He,d) dataset, for laboratory angle $\theta_{lab} = 30°$ measurements. To produce the overall fit, information about the known populated states are used. If the overall fit does not reproduce the data, it can be assumed that the missing strength is due to states believed to exist in the region where the fit to data fails.

Figure 7.4 shows a ^{12}C excitation energy spectrum for the $\theta_{lab} = 30°$ measurement. In the figure the peaks at 10.84 MeV and 11.83 MeV were fitted with a Lorentzian lineshape, with $\Gamma = 315$ keV and $\Gamma = 260$ keV, respectively. The peak at 9.641 MeV was generated using the R-matrix formalism. This state

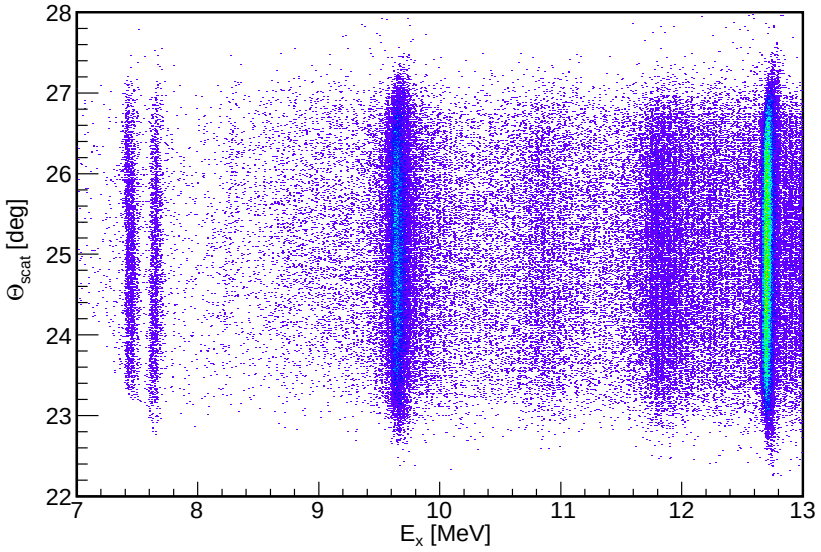

Figure 7.3: Two-dimensional plot of the deuteron emission angle against ^{12}C excitation energy measured at $\theta_{lab} = 25°$.

has a narrow width (34 keV) which is very much less than 63 keV energy resolution obtained in the present measurement. Its width was convoluted with the 63 keV experimental energy resolution. The dashed red curve in Fig. 7.4 shows the overall fit produced using the precisely known states which were populated in the present measurement, namely the 9.641 MeV 3^-, 10.84 MeV 1^- and 11.828 MeV 2^- states in ^{12}C. Their widths were obtained from Ref. [23] and are shown in Table 7.1. It expected that in the present measurement the population of the broad 0^+ state(s) in the 10 MeV excitation energy region must be very weak. Hence, these states were not included in the fit. The weak population of these state was also experienced in the measurement performed in Ref. [16]. Although it was not explicitly stated, no strength of the 0^+ state(s) was observed. The blue curve represents the estimated background. It can be seen the 11 MeV excitation energy region that the fit reproduces the experimental data very well. No additional strength was needed in this region for the fit to reproduce the data. This stresses the conclusion that the state at $E_x = 11.16$ MeV reported in the original measurement does not exist.

The 10 MeV region, however, shows a deficit when including only the 3^-, 1^- and 2^- sates (dashed red curve). Very interestingly, it is within this excitation energy region where previous measurements have reported the existence of the 2^+ excitation of Hoyle state in ^{12}C. Efforts were made in the present analysis to add the 2^+ strength in this region. The 2^+ resonance peak at $E_x \sim 9.7$ MeV with width of $\Gamma \sim 600$ keV was generated from R-matrix calculations. With this strength added the fit could reproduce the experimental data, consistently with previous measurements using various reactions. This gives additional confirmation of the existence of the 2^+ excitation of the Hoyle state believed to lie in the 9 - 10 MeV excitation energy region.

$\mathbf{E}_x$ [MeV]	$\mathbf{J}^\pi$	Γ [keV]
9.641	3^-	63
9.7	2^+	600
10.84	1^-	315
11.83	2^-	260

Table 7.1: Widths and resonance energies used for producing the overall fit.

7.1.3 Contaminants Investigation

With the techniques presented in the preceding section showing no evidence of a state at 11.16 MeV in ^{12}C, the question arises if the state observed in the original measurements may be attributed to contaminants. In Ref. [90], William explicitly stated that to produce the contaminant free enriched boron targets is not straight forward. Hence, one would expected the target to have traces of several contaminant nuclei. As mentioned in Chapter 3, two different targets were used to investigate possible contamination, namely a ^{10}B and a Li_2CO_3 target. Measurements were performed using these targets and were also analyzed using the procedures presented in Chapter 4. Excitation energy spectra were produced with software gates applied for deuterons.

Figure 7.5 shows a summary of ^{12}C equivalent excitation energy spectra populated in (^{3}He,d) and (^{3}He,t) reactions for $\theta_{lab} = 30°$ measurements. The

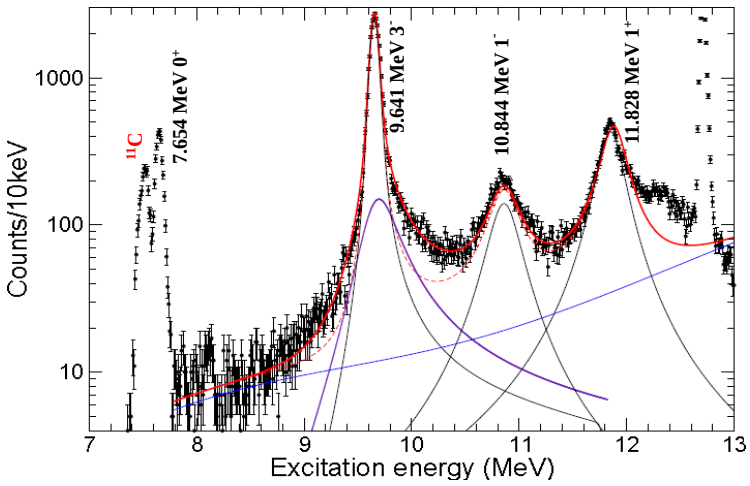

Figure 7.4: Excitation energy spectrum for the ^{11}B(^{3}He,d) reaction at laboratory angle $\theta_{lab} = 30°$ with the peaks at 10.84 MeV and 11.83 MeV fitted with a Lorentzian lineshape. At 9.641 MeV the 3^- peak was generated from an R-matrix calculation convoluted with the 63 keV experimental energy resolution. Added to that is a 2^+ resonance peak at 9.7 MeV also generated from an R-matrix calculation. The blue curve is a background with the solid red curve an overall fit. The dashed red curve shows the fit without a 2^+ state at 9.7 MeV.

red curve shows the excitation energy spectrum extracted from the ^{10}B(^{3}He,d) reaction. This target nominally consists of 20% ^{11}B and 80% ^{10}B. The presence of ^{10}B is seen through the strong peaks at 7.60 MeV and 12.2 MeV excitation energy, which are respectively the ground state and the 4.804 MeV excited state in ^{11}C populated through the ^{10}B(^{3}He,d) reaction. The blue curve corresponds to the measurement performed using the Li_2CO_3 target where the gate was also applied to deuterons. Only two peaks can be seen coming from this target at the higher excitation energy region which could respectively identified as the ground states of ^{13}N and ^{17}F.

The question can be asked if the spurious peak seen in the original measurement could arise due to the detection of tritons. To investigate this, analysis was performed by applying a software gate on tritons, thus selecting the ^{11}B(^{3}He,t) reaction. The resulting contamination events in the ^{12}C excitation

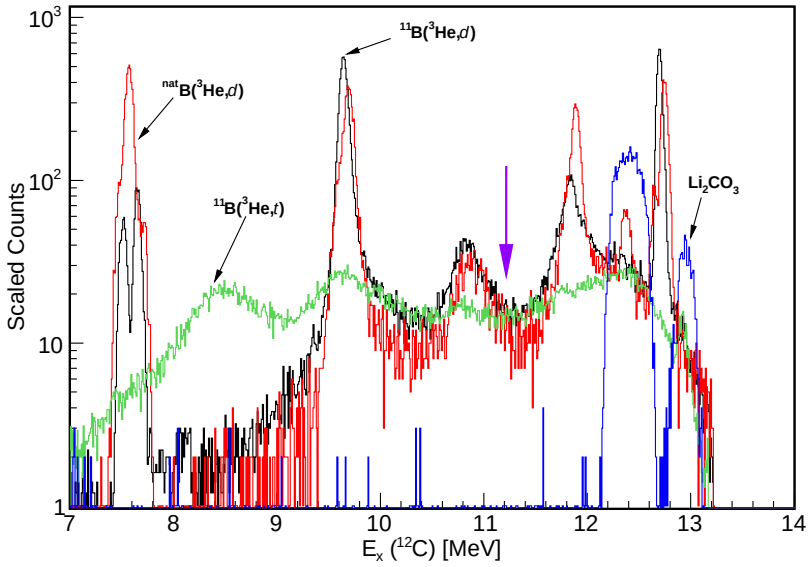

Figure 7.5: Investigation of potential background contribution in the excitation energy spectra populated in (^{3}He,d) and (^{3}He,t) reactions at $\theta_{lab} = 30°$. Also shown is an arrow indicating where the 11.16 MeV state is expected.

energy spectrum is represented by the green curve in Fig. 7.5. The black curve corresponds to the ^{11}B(^{3}He,d) reaction for the laboratory angle of $\theta_{lab} = 30°$ measurement. In the 11.16 MeV region (indicated by an arrow), none of the contaminant histograms show any evidence of a state.

As mentioned in section 3.7, the ERDA method found evidence of other contaminants in the ^{11}B target, namely ^{10}B, ^{12}C, ^{14}N and ^{16}O. These nuclei are shown in Fig. 7.6 where the energies lost by the nuclei on the ERDA detector are plotted against time-of-flight. Except for the Nitrogen target, these contaminants were not explicitly tested with the beam. Reaction kinematics calculations were also performed for these targets in order to investigate if the reaction would contribute in the region of interest. Using known states of the possible excited nuclei and the Q-values one would deduce a region where states from contaminants would be located in the ^{12}C excitation energy spectrum. Table 7.2 shows the targets investigated and their respective Q-values, also shown is the Q-value leading to the 11.16 MeV state. The kinematics calculations showed none of these target contaminants could populate a state

in the $E_x = 11.16$ MeV excitation energy region in ^{12}C.

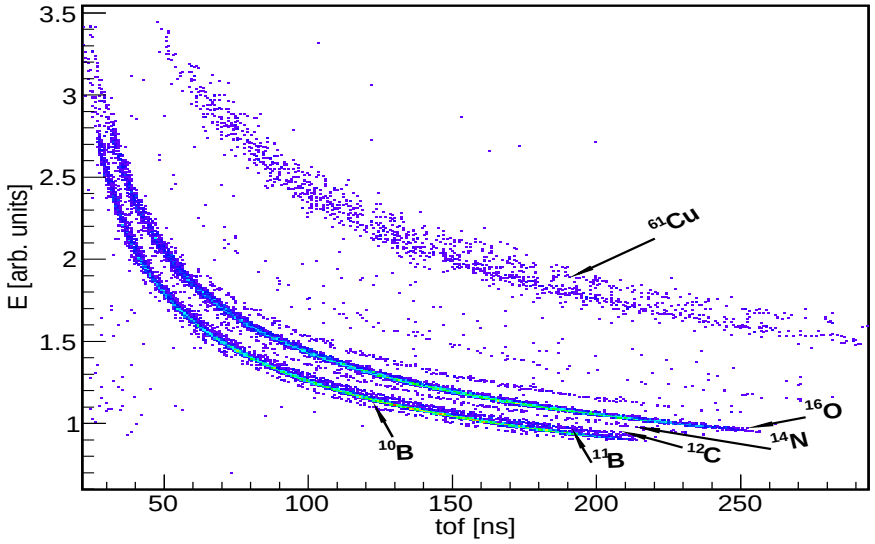

Figure 7.6: Energy versus time-of-flight 2D scatterplot of the light nuclei scattered from a 26.3 MeV ^{61}Cu beam, as obtained in an ERDA measurement. The ERDA beam and the target nuclei are indicated.

Target	Reaction	Q-Value [MeV]
Boron	^{11}B(^{3}He,d)^{12}C [11.16 MeV]	-0.697
	^{10}B(^{3}He,d)^{11}C	3.195
Carbon	^{12}C(^{3}He,d)^{13}N	-3.549
	^{13}C(^{3}He,d)^{14}N	20.57
Nitrogen	^{14}N(^{3}He,d)^{15}O	1.803
	^{15}N(^{3}He,d)^{16}O	6.633
Oxygen	^{16}O(^{3}He,d)^{17}F	-4.893
	^{17}O(^{3}He,d)^{18}F	0.113
	^{18}O(^{3}He,d)^{19}F	2.500
Lithium	^{6}Li(^{3}He,d)^{8}Be	0.113
	^{7}Li(^{3}He,d)^{9}Be	11.76

Table 7.2: Contaminant nuclei investigated with kinematics calculations shown with their respective Q-values. Also shown is the ^{11}B(^{3}He,d)^{12}C reaction Q-value leading to the $E_x = 11.16$ MeV state.

The background from the beam was also investigated through measurements on an empty target. For an empty target measurement a target frame identical to that used for the ^{11}B target was used with no foil mounted on it. This measurement was performed in order to quantify the contribution from scattered beam halo particles. Due to the fact that the present measurement employed an external beamstop, the total count rate was 1 Hz per 5 npA in the focal plane detectors which was very much lower than 25 Hz experienced with the ^{11}B target. It was therefore concluded that the beam halo had no effect on the ^{12}C excitation energy spectrum, as can be seen in Fig. 7.7. Because of the excellent low background in the present dataset it is difficult to comment on the presumption the $E_x = 11.16$ MeV state was observed in the original measurement could be due to beam quality.

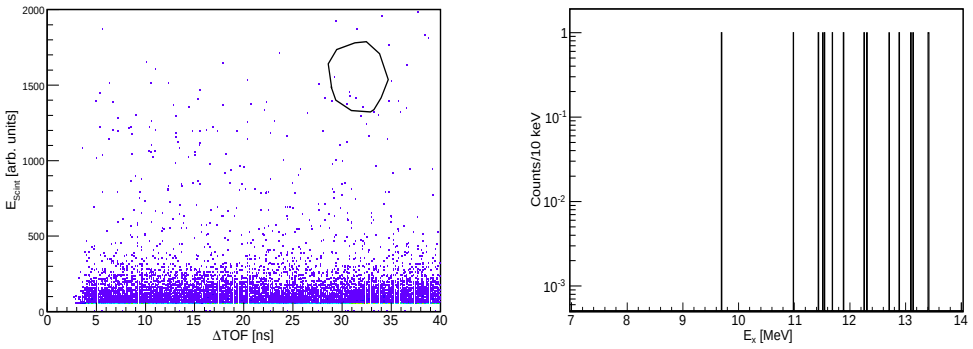

(a) (b)

Figure 7.7: Spectra obtained for empty target measurement at laboratory angle of $\theta_{lab} = 25°$. The data was recorded over a period of 20 minutes. (a) shows the two-dimensional spectrum of the pulse height in the scitillator versus relative TOF. The circled area represents region where deuterons are expected to be as was seen in the PID spectrum. (b) shows the excitation energy spectrum obtained by applying a software gate on the circled area in order to investigate background induced by beam halo on the final excitation energy spectrum. By applying the gate only 13 events made it through the cut. This is only 0.2% of the events obtained with the ^{11}B target also over a period 20 minutes with similar beam intensity.

7.2 (p,t) reaction

Fitting analysis of the ^{12}C excitation energy spectrum obtained from the ^{11}B(^{3}He,d)^{12}C reaction showed evidence of the 2^+ state in the 10 MeV excitation energy region. This is consistent with the results from recent measurements [27, 28, 29, 30, 31, 32], where evidence of the 2^+ state in this excitation energy region were reported. The measurement was performed in the present study to further characterize this newly found state. Results obtained for this measurement are the topic of this section. Firstly, the singles excitation energy will be extracted. Thereafter, in order to study the decay properties of the populated states, the inclusion of the coincidences will be required.

7.2.1 Singles Excitation Energy Spectrum

Figure 7.8 shows the ^{12}C excitation energy spectrum between 7 and 17 MeV populated using the ^{14}C(p,t)^{12}C reaction. It was obtained at a proton energy of E_{lab} = 66 MeV and a laboratory angle of θ_{lab} = 21°. Marked in the figure are the six strongly populated ^{12}C states, namely, the 7.654 MeV 0^+, 9.641 MeV 3^-, 12.71 MeV 1^+, 14.083 MeV 4^+, 15.110 MeV 1^+ and the 16.105 MeV 2^+ state. The two contaminant peaks are also marked with symbols *i.e.* $^{11}C_{gs}$ (at 10.75 MeV) and $^{14}O_{gs}$ (at 15.49 MeV). These two contaminant peaks are also visible in Fig. 5.9.

Table 7.3 shows the energy levels of ^{12}C obtained from Ref. [23]. Only the levels that are situated in the excitation energy between 7 and 17 MeV are listed. Information within the square brackets illustrates that the results are inconclusive. From Table 7.3 and Fig. 7.8 it is evident that some states were strongly populated while other states were not populated in the present measurement. For some states, however, their population is ambiguous, either because they were weakly populated or their obscured by other broad states making their observation difficult. In the excitation energy region of interest

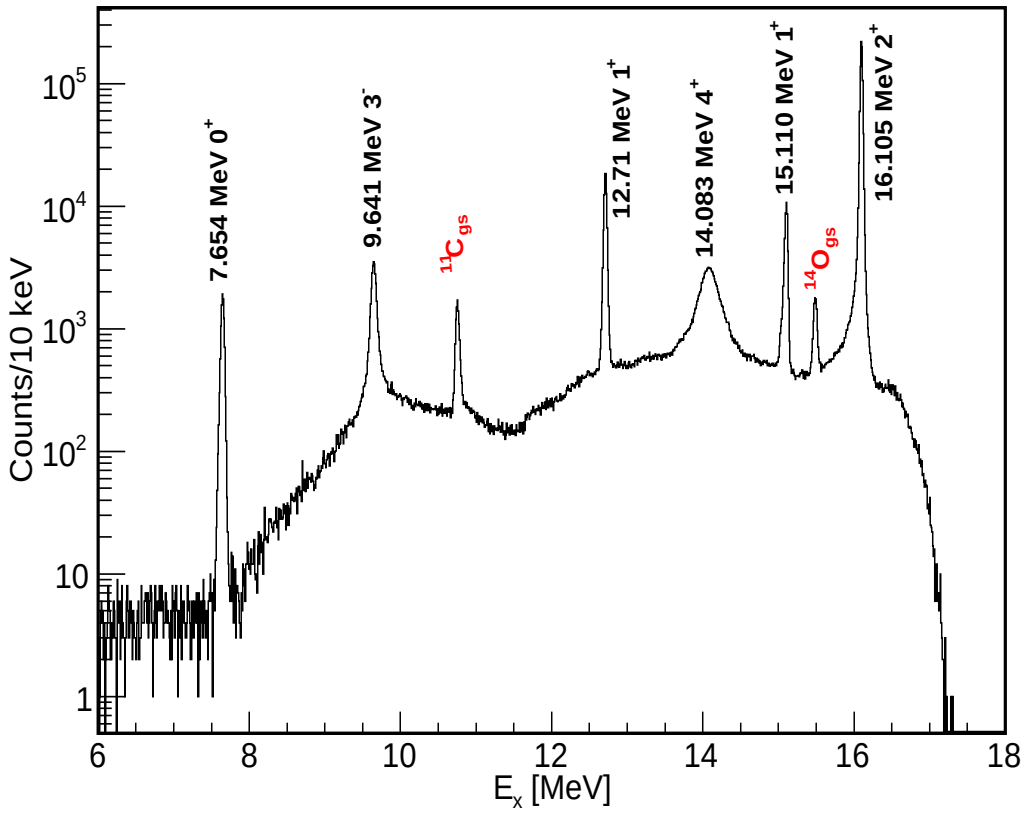

Figure 7.8: The ^{12}C excitation energy spectrum populated using the ^{14}C$(p,t)^{12}$C reaction for singles events.

i.e. the 10 MeV region, the states in question are; the broad $J^{\pi} = 0^{+}$ state believed to exist at $E_x \sim 10.3$ MeV with width of $\Gamma \sim 3$ MeV wide, the $J^{\pi} = 2^{+}$ excitation of the Hoyle state and the $J^{\pi} = 1^{-}$ state at $E_x = 10.844$ with width of $\Gamma = 0.315$. A peak fitting analysis was performed in order to fully understands the excitation energy spectrum. It is expected that the fit will replicate the measured spectrum provided the strengths of all the populated states are included. By using this method one can find information of the elusive states in this region. Presented in the next sections are the steps followed in order to perform the final peak fitting analysis of the excitation energy spectrum.

E_x in ^{12}C [MeV $\pm \times 10^{-3}$ MeV]	J^π	T	$\Gamma_{c.m.}$ [MeV]
7.654 ± 0.15	0^+	0	$(8.5 \pm 1.0) \times 10^{-6}$
9.641 ± 5	3^-	0	0.034 ± 0.005
10.3 ± 300	$[0^+]$	0	3.000 ± 0.70
10.844 ± 16	1^-	0	0.315 ± 0.025
[11.16 ± 50]	$[2^+]$	[0]	[0.430 ± 0.080]
11.828 ± 16	2^-	0	0.260 ± 0.025
12.710 ± 6	1^+	0	$(18.1 \pm 2.8) \times 10^{-6}$
13.352 ± 15	2^-	0	0.375 ± 0.040
14.083 ± 15	4^+	0	0.258 ± 0.015
15.110 ± 3	1^+	1	$(43.6 \pm 1.3) \times 10^{-6}$
15.44 ± 40	$[2^+]$	[0]	1.5 ± 0.200
16.1058 ± 7	2^+	1	$(5.3 \pm 0.2) \times 10^{-3}$
16.57	2^-	1	0.300×10^{-3}

Table 7.3: The energy levels of ^{12}C obtained from Ref. [23]. Only the states in the covered energy region are shown. The 11.16 MeV state is shown in red since it has been concluded that it does not exist in the work perfomed in this study [91].

Fitting procedure

In order to fix the boundaries in the fitting process, only the region of interest was taken into account, thus only the excitation energy region between 7.5 and 11.5 MeV was considered. Over the years this particular part of the excitation energy region in the ^{12}C nucleus has proved to be difficult to interpret. This is owing to the fact that the nature of some of the states in this region is not well understood. Although this region suffers from an overlap of a number of broad states, there are, however, some precisely known states in this region, namely, the 7.654 MeV 0^+ state (the Hoyle state), the 9.641 MeV 3^- state, and the 10.844 MeV 1^- state. To perform the fitting procedure, information about the states i.e. the energies and widths are included in the fitting routine.

Figure 7.9 shows the ^{12}C excitation energy spectrum between E_x = 7.5 - 11.5 MeV measured using the ^{12}C(p,t) reaction. Also shown in the figure is the fit (solid red curve) produced using only the precisely known states in this

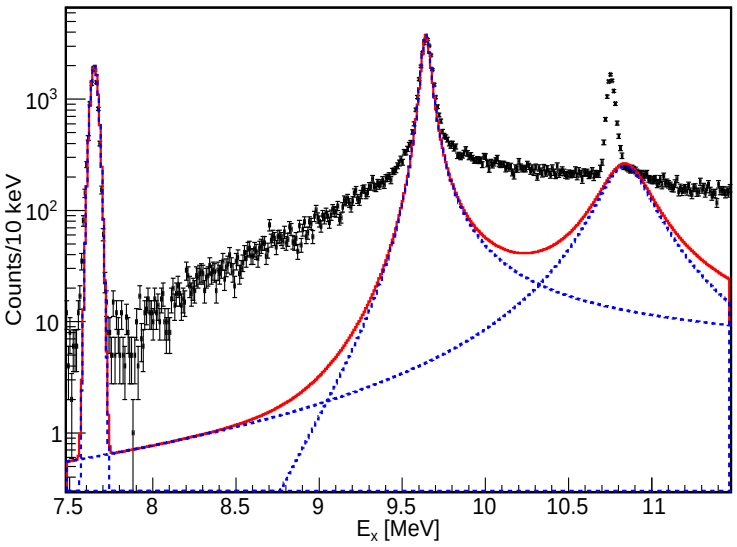

Figure 7.9: ^{12}C excitation energy spectrum in the E_x = 7.5 - 11.5 MeV excitation energy region. Also shown is the fit performed using the three precisely known states in this region. The lineshapes of the individual states used are indicated by the blue dashed curves.

excitation energy region. The lineshapes of individual states are also shown (dashed blue curves). These individual lineshapes were generated as follows:

- Due to its narrow width, lower than the experimental resolution of 28 keV, the Hoyle state was generated using a Gaussian distribution function.
- The 9.641 MeV 3^- state was generated using the R-matrix calculation (presented in Chapter 6).
- Since the 10.844 MeV state is away from the α-decay threshold, it is expected that the effects of the centrifugal barrier are negligible. Hence, its lineshape was generated using the Lorentzian distribution.

In generating the fit, the energies and widths of the states were not free parameters. Only the amplitudes of the states were allowed to vary. It is evident that using only the strength of these three precisely known states does not

reproduce the measured spectra. The large $\chi^2/d.o.f$ value of 61.46 was obtained[6]. This highlights the need to add other strength from state(s) in order to improve the fit.

From Table 7.3, the excitation energy region of interest is characterized by a broad 0^+ state located at $E_x = 10.3$ MeV. Hitherto, the characteristics of this state remain somewhat of a mystery. In recent studies, different results about the true nature of this state have been reported. In 2005, Fynbo *et al.* [92] determined the energy of the broad 10-MeV resonance using the R-Matrix fitting technique and found the $J^\pi = 0^+$ state to be at an excitation energy of $E_x = 11.23 \pm 0.05$ MeV with a width of $\Gamma = 2.5 \pm 0.2$ MeV. In 2011, Itoh *et al.* [29] found the 0^+ state to be situated at excitation energy of $E_x = 9.93 \pm 0.03$ MeV with a width of $\Gamma = 2.71 \pm 0.08$ MeV. They also reported the possibility of the 0^+ component being composed of two 0^+ states located at $E_x = 9.04 \pm 0.09$ MeV with a width of $\Gamma = 1.45 \pm 0.18$ MeV and at $E_x = 10.56 \pm 0.06$ MeV with a width of $\Gamma = 1.42 \pm 0.18$ MeV. The proposition of the two 0^+ components in this region was also suggested in Ref. [93]. Considering the difference between these results, the inclusion of the 0^+ state in the fitting procedure was not straightforward. In this study various techniques were employed in order to acquire the best possible parameters for this state.

Parameterization of the broad 0^+ state(s)

In order to obtain these parameters two different datasets were used, namely the already available ^{12}C(α,α') [94] and ^{12}C(p,p') [95] datasets. Both datasets were obtained using the high energy resolution K600 magnetic spectrometer at iThemba LABS, South Africa. The ^{12}C(α,α') dataset was obtained at an laboratory angle of $\theta_{lab} = 0°$ using an α beam energy of $E_{lab} = 160$ MeV, while the ^{12}C(p,p') dataset was obtained at an laboratory angle of $\theta_{lab} = 4°$

[6] d.o.f refers to degrees of freedom.

using a proton energy of 100 MeV. It is at these laboratory angles that the angular distribution calculations of 0^+ states performed in Refs. [29] and [27] appeared to be at or near a maximum for $^{12}C(\alpha,\alpha')$ and $^{12}C(p,p')$, respectively. Therefore, at these angles an enhancement in 0^+ states is expected. Hence, the weakly populated states such as the 2^+ state will be obscured [29].

In order to obtain the parameters the two dataset were fitted and the parameters that produced the best fit were selected. In addition to the 0^+ component(s) being investigated, the following states were included: the 7.65 MeV 0^+ state, 9.641 MeV 3^- state and the 10.844 MeV 1^- state. For these three states, the energy and width were not free parameters, only the amplitudes were allowed to vary. Whereas for the 0^+ component the following parameters were tested:

- A state centered at 9.93 MeV with a width of 2.71 MeV [29].
- A state centered at 10.3 MeV with a width of 3.0 MeV [23].
- A state centered at 11.23 MeV with a width of 2.5 MeV [92].
- Two 0^+ components, one centered at 9.04 MeV with a width of 1.45 MeV and one centered at 10.56 MeV with a width of 1.42 MeV [29].

Figures 7.10 and 7.11 respectively show the ^{12}C excitation energy spectra for $^{12}C(\alpha,\alpha')$ and $^{12}C(p,p')$ with their respective fits. To produce the fit, different lineshapes were used for the included states. The Gaussian function was used for the 7.65 MeV 0^+ state and the broad 10 MeV 0^+ component(s). The 9.641 MeV 3^- peak was generated from an R-matrix calculation and the Lorentzian function was used to generate the 10.84 MeV 1^- state. If the width of the state is less than the measured energy resolution, then the width was set according to the measured energy resolution, which was 70 keV for $^{12}C(\alpha,\alpha')$ and 30 keV for the $^{12}C(p,p')$ measurement. In order to be able to select the best parameters for the 0^+ component(s), the $\chi^2/d.o.f$ values obtain in each fit were recorded

and overall values were compared. The parameters that produced the lowest $\chi^2/d.o.f$ value were selected and used in the fitting of the excitation energy spectrum obtained from the ^{14}C(p,t) reaction.

Table 7.4 shows the $\chi^2/d.o.f$ values obtained from different 0^+ component(s) parameters. From the table it is evident that parameters that produced the better $\chi^2/d.o.f$ value in comparison with others are the two 0^+ components. The large $\chi^2/d.o.f$ values for ^{12}C(p,p') dataset are due to the fact that the lineshape correction performed to optimized the energy resolution was performed using the 9.641 MeV 3^- state instead of the Hoyle state. As a result, the Hoyle state could not be reproduced very well with the Gaussian or Lorentzian function leading to a large root-mean-square (rms) value in this region. This supports the idea that the broad state within the 10 MeV region could be composed of the two 0^+ components. Therefore, to account for the broad 0^+ state in the fitting procedure performed, the two 0^+ components were included in the following fits.

Normalizing ^{14}C(p,t) spectrum to ^{12}C(α,α') and ^{12}C(p,p').

From the cross section calculations performed in Chapter 6, it was shown that the laboratory angle at which the present measurement was performed (θ_{lab} = 21°) is the angle at which one would expect enhancement in 2^+ states and suppression of 0^+ states. Hence, it is expected that the 0^+ states would be weakly populated at this laboratory angle. If populated, one would expect the tail of the 0^+ component at E_x = 9.04 MeV to be visible on the low excitation energy side. In order to include it in the fitting procedure, the 0^+ state strength situated at E_x = 9.04 MeV was normalized on the populated excitation energy spectrum at E_x = 8.5 MeV, as it was the case in Refs. [27, 30]. Figure 7.12 shows the ^{12}C(α,α') and ^{12}C(p,p') datasets normalized with the ^{14}C(p,t) data at E_x = 8.5 MeV showing how the strength of the 0^+ component coincide with the ^{14}C(p,t) excitation energy spectrum. Hence, in the fitting procedure the

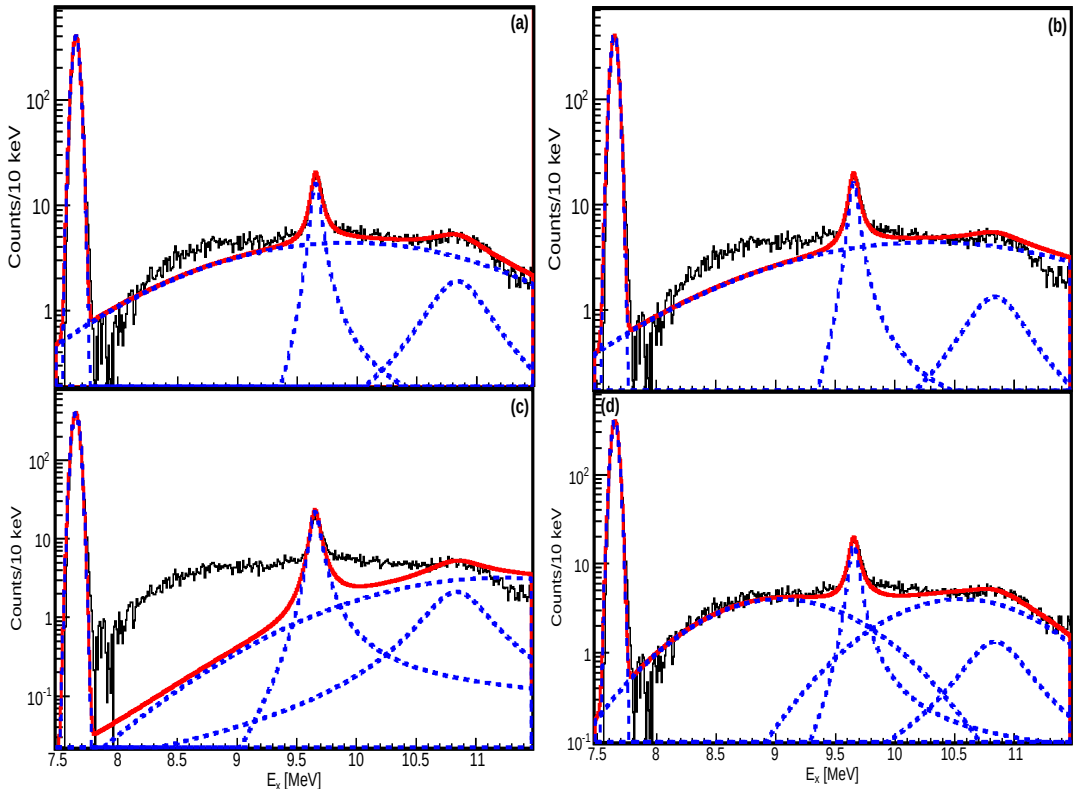

Figure 7.10: Excitation energy spectra for ^{12}C obtained using α-particle inelastic scattering at E_{lab} = 160 MeV at $\theta_{lab} = 0°$ fitted to the 7.65 MeV 0^+, 9.64 MeV 3^- and the 10.84 MeV 1^-. Added to the fit is the strength of the broad 10 MeV 0^+ component(s), (a) the 9.93 MeV with a width of 2.71 MeV, (b) the 10.0 MeV with a width of 3.90 MeV, (c) the 11.23 MeV with a width of 2.5 MeV and (d) the two 0^+ contributions are added, the 9.04 MeV with a width of 1.45 MeV and the 10.56 MeV with a width of 1.42 MeV. The solid red curve shows the overall fitting results of the complete fit and the blue dashed curves show the individual peaks.

Dataset	**State [MeV]**	$\chi^2/d.o.f$	**Dataset**	**State [MeV]**	$\chi^2/d.o.f$
^{12}**C**(α,α')	9.93	1.081	^{12}**C**(p,p')	9.93	22.60
	10.30	1.052		10.30	23.46
	11.23	1.976		11.23	66.61
	9.04 & 10.56	0.803		9.04 & 10.56	22.41

Table 7.4: Table showing the $\chi^2/d.o.f$ values obtained from different 0^+ component(s) parameters used in fitting the ^{12}C excitation energy spectra obtained from ^{12}C(α,α') and ^{12}C(p,p') dataset.

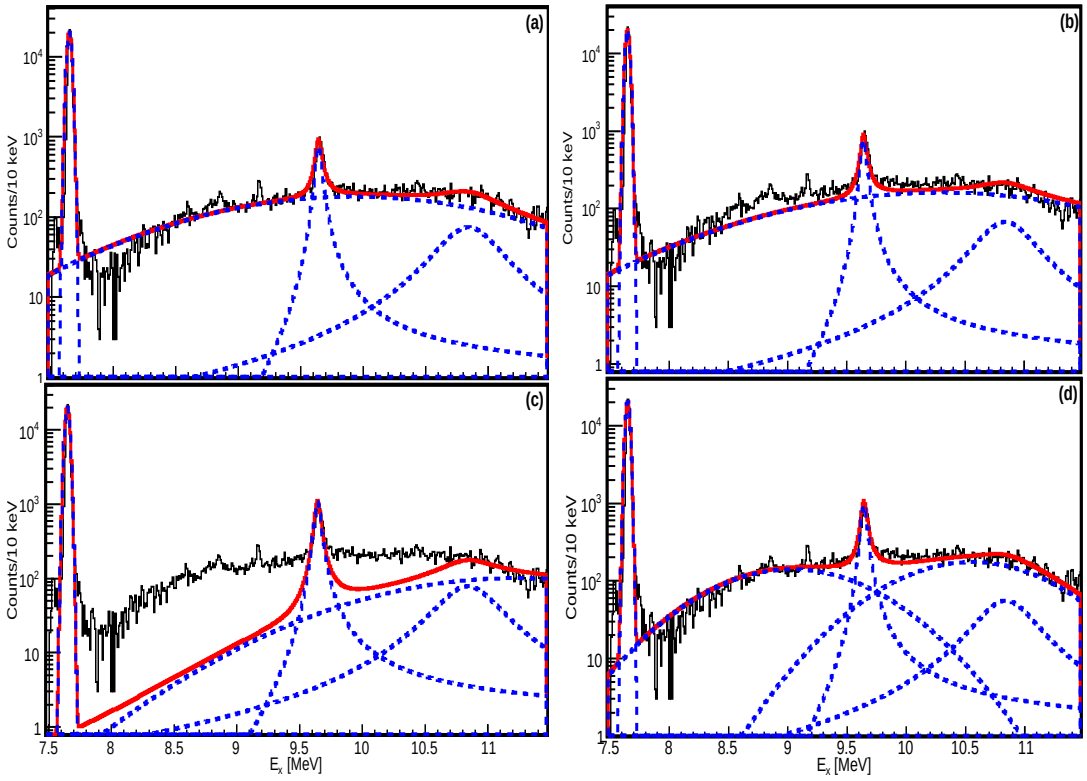

Figure 7.11: Excitation energy spectra for ^{12}C obtained using proton inelastic scattering at E_{lab} = 100 MeV at θ_{lab} = 4° fitted to the 7.65 MeV 0^+, 9.64 MeV 3^- and the 10.84 MeV 1^-. Added to the fit is the strength of the broad 10 MeV 0^+ component(s), (*a*) the 9.93 MeV with a width of 2.71 MeV, (*b*) the 10.0 MeV with a width of 3.90 MeV, (*c*) the 11.23 MeV with a width of 2.5 MeV and (*d*) the two 0^+ contributions are added, the 9.04 MeV with a width of 1.45 MeV and the 10.56 MeV with a width of 1.42 MeV. The solid red curve shows the overall fitting results of the complete fit and the blue dashed curves show the individual peaks.

amplitude of this state was fixed to data at E_x = 8.5 MeV.

Fitting the singles ^{14}C(p,t) spectrum

With the parameters of the broad 0^+ components characterized, the next step was to fit the singles ^{12}C excitation energy spectrum shown in Fig. 7.8. Figure 7.13 shows the ^{12}C excitation energy spectrum measured from the ^{14}C(p,t) reaction. The red-dashed curve shows the fit performed using the two 0^+ components at E_x = 9.04 MeV and E_x = 10.56 MeV, as well as the 7.654 MeV 0^+, the 9.641 MeV 3^-, and the 10.844 MeV 1^- states. Similar to the preced-

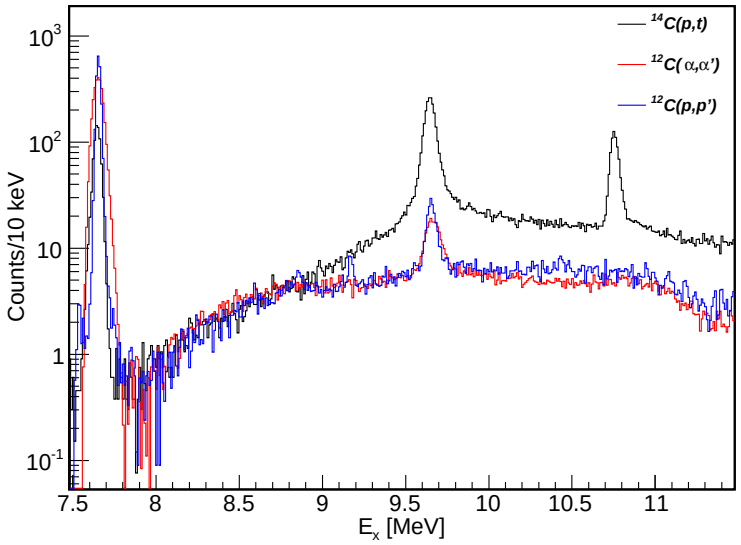

Figure 7.12: The ^{12}C(α,α') and ^{12}C(p,p') excitation energy spectra normalized to the ^{14}C(p,t) excitation energy spectrum at E_x = 8.5 MeV.

ing procedures, the Gaussian function was used to produce the lineshape of the 7.654 MeV 0^+, 9.04 MeV 0^+, and 10.56 MeV 0^+ states, and a Lorentzian function was used for the 10.844 MeV 1^- state. For the 9.641 MeV 3^- state, a one channel R-matrix formulation was used. The energy and width of all the states were fixed parameters, with only the amplitudes allowed to vary (except for 9.04 MeV 0^+ state). For the Hoyle state, which has a natural width less than the measured experimental resolution, the width was convolved with the experimental resolution of 28 keV. The broad 9.04 MeV 0^+ strength was normalized to the data at E_x = 8.5 MeV. It is evident from the red-dashed curve that the fit produced with these strengths fails to reproduce the measured spectrum at the excitation energy region between $E_x \sim$ 8.9 and 10.5 MeV. This is also confirmed by the $\chi^2/d.o.f$ value of 25.54 (corresponding to the region E_x = 7.5 to 11.2 MeV with the contaminant peak excluded). This discrepancy could not be associated to the strength from a contaminant as the contaminants investigation performed in section 5.4 eliminates the possibility of having a contaminant peak at this excitation energy region. Thus, it could

only be associated with the omission of the 2^+ strength which needs to be added as in Refs. [27, 30].

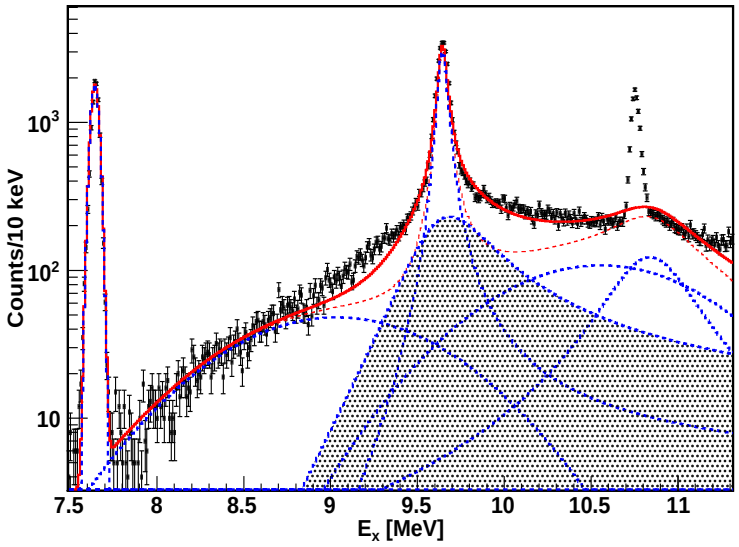

Figure 7.13: The excitation energy spectrum of ^{12}C as measured from the ^{14}C(p,t) reaction. The red dashed shows the fit with all known ^{12}C states. The solid red curve represents the fit performed with the added contribution of the 2^+ strength. The dashed blue curves show the individual states added to the fit, with the 2^+ lineshape shown as the hatched area.

In order to add the missing 2^+ strength to the fit, the lineshape of the 2^+ resonance was generated using the one channel R-matrix formulation. As part of the fitting procedure, the available 2^+ parameters reported in Refs. [27, 30, 29, 31] were tested. These parameters are summarized in Table 7.5, where the energies, width as well as the $\chi^2/d.o.f$ values obtained from he fit are shown. It is worth noting that the one channel R-matrix calculation was used to extract the 2^+ resonance lineshapes in Refs. [27, 30, 31] whereas in Ref. [29] a Gaussian function was used. However, in the present study, all the lineshapes were obtained from R-matrix calculations. Figure 7.14 shows the 2^+ R-matrix generated lineshapes associated with the different parameter sets.

Owing to the large values of $\chi^2/d.o.f$ (see Table 7.5), efforts were made in order to improve the overall fit by adjusting the resonance energy, width and

Energy [MeV]	Width [MeV]	$\chi^2/d.o.f$
9.6	0.600	10.4
9.75	0.750	8.13
9.84	1.010	8.17
10.03	0.800	13.3

Table 7.5: The energies and width of the 2^+ resonances used in the fit. The $\chi^2/d.o.f$ values obtained are shown in the 3^{rd} column.

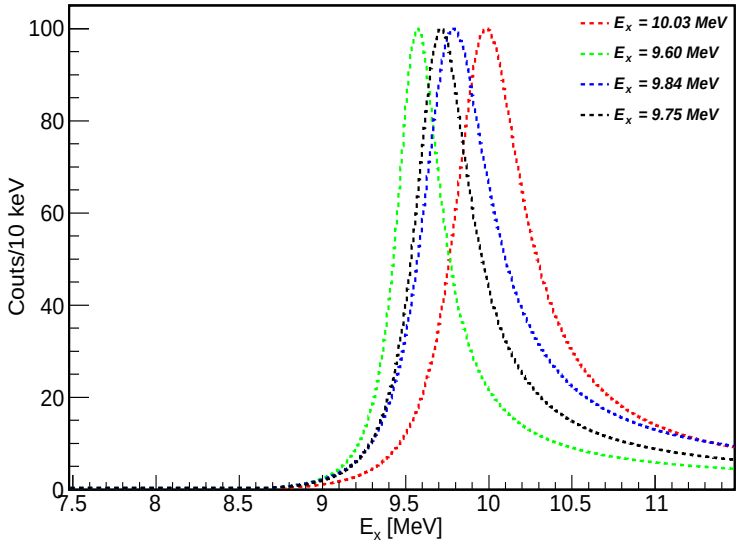

Figure 7.14: The 2^+ resonance lineshapes produced by using the resonance parameters reported in Refs. [27, 30, 29, 31].

the amplitude of the 2^+ resonance lineshape. The solid red curve in Fig. 7.13 shows the fit with the additional 2^+ strength added. It can be seen that the fit is a good reproduction of the data. The $\chi^2/d.o.f$ value obtained for this fit is 5.98. The hatched region shows the lineshape of the 2^+ state added to the fit. The observed parameters obtained for this state are $E_x = 9.69 \pm 0.11$ MeV with width of $\Gamma = 1.434 \pm 0.22$ MeV.

Does the use of two 0^+ components affect the parameters of the 2^+ resonance?

The width of the obtained 2^+ resonance is much larger than those reported in Refs. [27, 30, 29]. This was associated with the fact that in the present work two 0^+ components were utilized while one broad 0^+ component was used to account for the broad strength in the 10 MeV excitation energy region in Refs. [27, 30, 29]. To investigate this effect, a fit was produced using the 10.3 MeV 0^+ state. Figure 7.15 shows the fitted ^{12}C excitation energy spectrum. The red dashed curve shows the fit produced using only known states as was presented in the preceding section. The only difference is the use of the one 0^+ component at $E_x = 10.3$ with width of $\Gamma = 3$ MeV instead of the two 0^+ components previously used. It is evident that this fit fails to reproduce the measured spectrum at excitation energy region between $E_x \sim 8.9$ and 10.5 MeV. Therefore the additional 2^+ strength was also added to improve the fit by varying the resonance energy and width. This was done through $\chi^2/d.o.f$ minimisation. The solid red curve shows the best fit obtained using the 2^+ resonance at $E_x = 9.66 \pm 0.12$ MeV with width of $\Gamma = 1.09 \pm 0.17$ MeV. This shows that using the one 0^+ component instead of the two 0^+ components (used in the present study) would influence the width extracted for the 2^+ resonance.

7.2.2 Characterization of the Populated States

In order to probe the decay properties of the populated states, the analysis of coincidence events was required. Only double and triple coincidence events were considered in the present study with quadruple coincidence events discarded due to low statistics. Figure 7.16 lists the populated states as well as their expected decay modes. Since all the states are situated above the α-decay threshold, located at $E_x = 7.2748$ MeV, they are all expected to decay via α emission. Furthermore, the proton separation energy for ^{12}C is situated at E_x

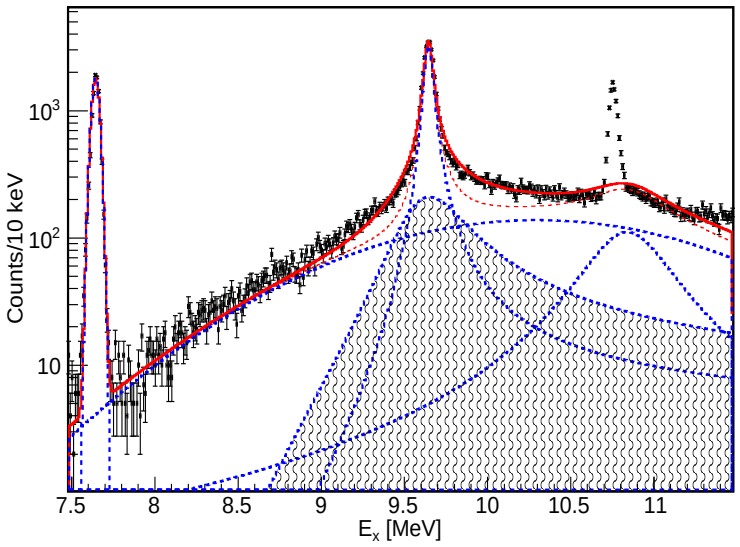

Figure 7.15: The excitation energy spectrum of ^{12}C as measured from the ^{14}C(p,t) reaction. Also shown are the fits obtained by including one 0^+ component instead of two.

= 15.957 MeV, hence the 16.105 MeV state is also open to proton emission. Apart from the typical decay channels i.e. α, γ and proton decays, emission of a e^+e pairs (π) has been observed for the 7.6542 MeV Hoyle state [9, 13, 96].

In the present study, the decay through α emission is of interest. It has been shown (section 5.5.4) that this decay process can happen in two different ways. From the populated states, it is clear that the (p,t) reaction is able to populate both the natural parity states, namely $J^+ = 0^+$, 2^+, 4^+ and 3^- as well as the unnatural parity states, such as the $J^+ = 1^+$ states. The natural parity states are states of which the spin (J) and parity (π) satisfy the relation $\pi = (\text{-}1)^J$, whereas for the unnatural parity states this relation does not hold. The natural parity states can decay through all the decay modes whereas the unnatural parity states can not decay sequentially via the ground state of ^{8}Be. This is because this decay mode violates parity conservation relation.

Several studies have been performed to investigate the α-decay branching ratios of some excited states in ^{12}C nucleus. In 2012, Manfredi *et al.* [14] studied the α-decay of the Hoyle state and the 9.641 MeV 3^- states and con-

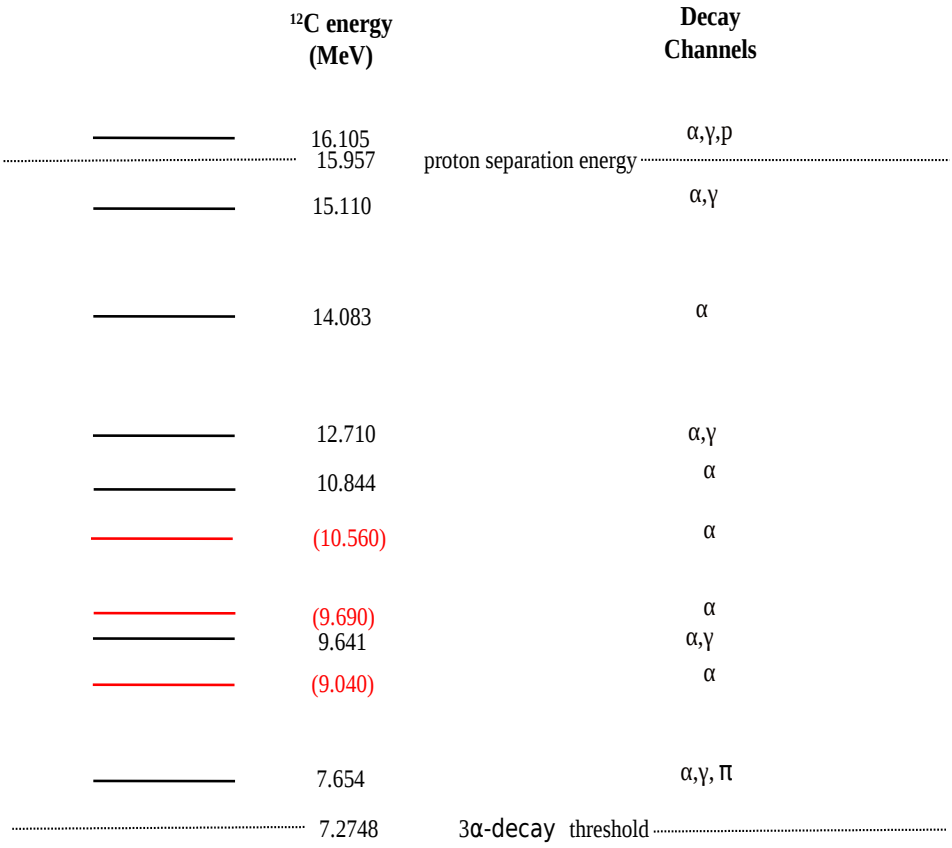

Figure 7.16: The ^{12}C energy levels populated using the ^{14}C$(p,t)^{12}$C reaction with their expected decay channels. Also indicated are the 3α and proton decay thresholds.

cluded that both these states decay most exclusively through the ground state of ^{8}Be. In 2003, Fynbo *et al.* [97] studied the three-body decay of the 12.71 MeV 1^+ state and found that it can decay through both the ^{8}Be$_{2^+}$ state and democratic decay. They could not, however, specify the branching ratios of these two decay modes. Theoretically, the α-decay branching ratios have been investigated by Álvarez-Rogriguez *et al.* [98] where the complex scaled hyperspherical adiabatic expansion method was used to compute momentum and

energy distributions of the three α-particles emerging from the decay of the low-lying ^{12}C resonances. Table 7.6 presents the estimated ratios of sequential decay via $^{8}\mathrm{Be}_{gs}$ compared to direct decays, for various states in ^{12}C as calculated in Ref. [98].

J^{π}	E_x [MeV]	Sequential via $^{8}\mathrm{Be}_{gs}$ [%]	Direct [%]
0_1^+	7.66	95	5
2_1^+	8.66	97	3
3^-	9.60	96	4
4_1^+	10.52	92	8
1^-	10.88	70	30
0_2^+	11.22	59	41
2_2^+	11.76	15	85
2_3^+	13.76	4	96
4_3^+	14.10	20	80
6^+	14.40	5	95

Table 7.6: The estimated ratios of sequential decay via $^{8}\mathrm{Be}_{gs}$ and direct decays for the natural-parity states of ^{12}C, obtained from the theoretical calculations of Ref. [98].

From the table, the 2_1^+ state located at $E_x = 8.66$ MeV can be related to the 2^+ excitation of the Hoyle state. It is clear that the α-decay branching ratio of this state is dominated by the sequential decay path via $^{8}\mathrm{Be}_{gs}$. This should then also be expected for the 2^+ state reported in the present study. Figure 7.17 shows the spectrum of the relative energy between two α-particles for triple coincidence events. Labeled in the figure are different decay modes. From the figure it is evident that one can easily distinguish between the $^{8}\mathrm{Be}_{gs}$ decay mode and "other" modes ($^{8}\mathrm{Be}_{2^+}$ and direct decay). The other modes, however, cannot be easily distinguished from one another. In the present study, efforts were made to study these decay modes separately i.e. ^{8}Be ground state mode and other decay modes[7].

[7]Here "other" refers to different decay modes i.e. sequentially though ^{8}Be 2^+ state, sequentially though the ^{8}Be ground state ghost anomaly, and democratic decay.

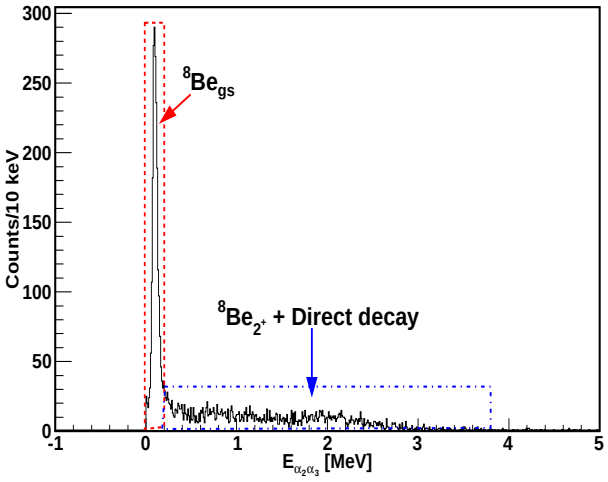

Figure 7.17: Relative energy between two α-particles for triple coincidence events showing how different decay modes can be distinguished.

7.2.2.1 Breakup through the ^{8}Be ground state

It has already been shown that events where the excited ^{12}C nucleus decays through the $^8Be_{gs}$ can be selected by placing a gate on the 0.091 MeV peak shown in Fig. 7.17. These events can also be seen with a red locus shown in Fig. 7.18 for double coincidence events. In Fig. 7.18, the relative energy between the first emitted α-particle and the reconstructed intermediate ^{8}Be is plotted against the ^{12}C excitation energy for both the experimental and simulated data. The green locus in the experimental spectrum indicates the decay thorough other decay modes that could not be distinguished from one another. The simulated data were generated for ground state decay and the miss-reconstructed events are indicated. Figure 7.19 shows the ^{12}C excitation energy spectrum produced by applying a software gate on the $^8Be_{gs}$ events. It should be noted that, by applying this gate, the ^{11}C contaminant peak vanishes. As in the singles events, the peak fitting analysis was performed in order to fit this spectrum.

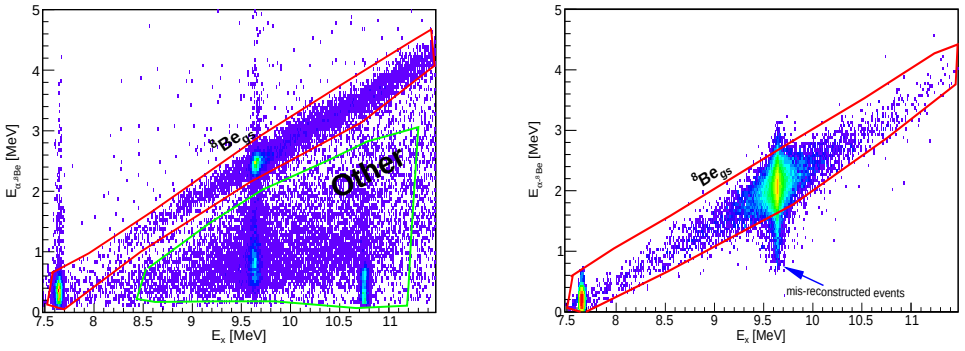

(a) (b)

Figure 7.18: The relative energy between the first emitted α-particle and the intermediate ^{8}Be nucleus plotted against the ^{12}C excitation energy spectrum for the (a) experimental data and (b) simulated data. The red locus around the ^{8}Be$_{gs}$ events is shown.

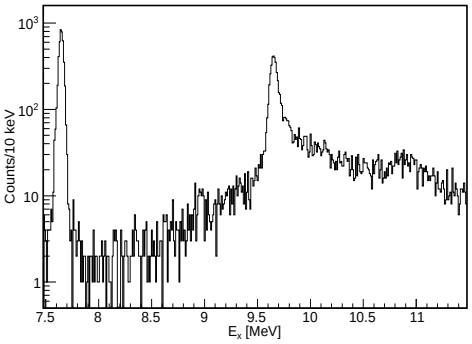

Figure 7.19: The ^{12}C excitation energy spectrum produced from ^{8}Be$_{gs}$ decay gated events, indicated in Fig. 7.18 with a red locus.

Efficiency Corrections

Prior to the peak fitting analysis, the effects of the detection efficiency of the silicon array on the excitation energy spectrum were investigated and corrected. This was done using the *SimSort* code by performing Monte Carlo simulations in the region of interest. The conditions used in experimental data analysis, namely the calibration coefficients and detection thresholds, were also applied to the simulated events. Figure 7.20 shows the efficiency plots that indicate how the detection efficiency varies as function of excitation energy in the re-

gion between E_x = 7.5 - 11.5 MeV. Two types of coincidences were simulated, the double coincidence 7.20(a) and triple coincidence 7.20(b). From the figure it is visible that for double coincidence the efficiency decreases with increasing excitation energy whereas for triple coincidence events the region of interest, i.e the 10 MeV region, seems to be the more efficient than at lower energies. With the efficiency of the double coincidences low in the region of interest, an efficiency correction was needed in order to obtain a ^{12}C excitation energy spectrum which is not efficiency dependent.

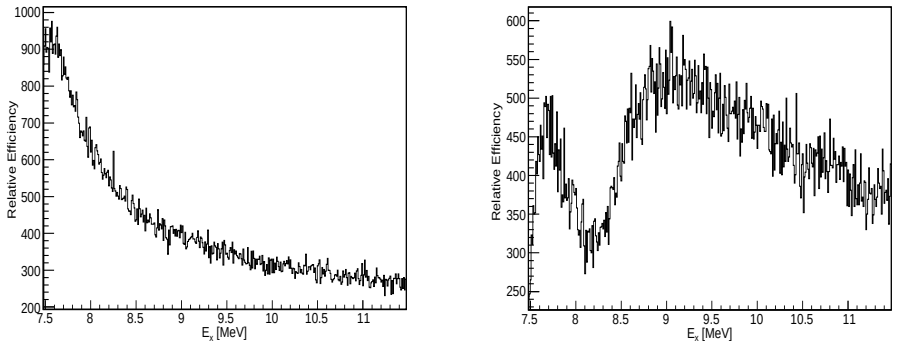

(a) (b)

Figure 7.20: Efficiency plots showing how the Silicon array efficiency varies with excitation energy for two types of coincidences (a) double coincidence events (b) triple coincidence events simulated for ground state decay mode.

Figure 7.21 shows the ^{12}C excitation energy spectra illustrating how correcting for efficiency affects the excitation energy spectra. Two curves are shown, before the correction (black) and after the correction (red). In order to investigate if the newly found 2^+ could decay through the ^{8}Be$_{gs}$ decay mode, the ^{8}Be ground state gated ^{12}C excitation energy spectrum was fitted using the fitting procedure used previously for the singles spectrum.

Fitting Procedure

Figure 7.22 shows the ^{12}C excitation energy spectrum for ^{8}Be$_{gs}$ gated events. Also shown is the fit (red dashed) produced using the following states: the

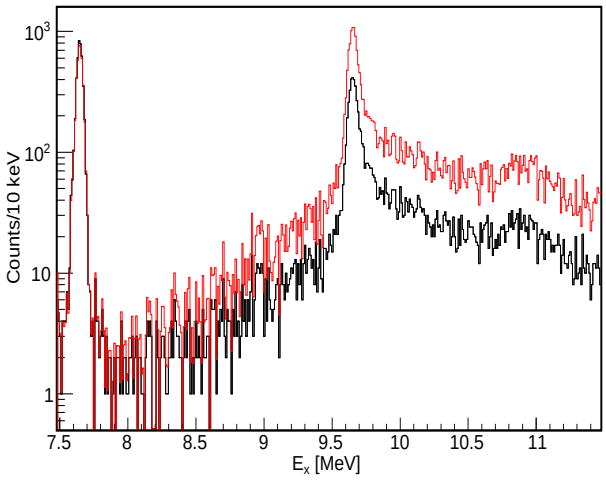

Figure 7.21: The ^{12}C excitation energy spectra produced from ^{8}Be$_{gs}$ decay gated events before efficiency correction (black) and after the correction (red).

Hoyle state (7.654 MeV 0^+), the 9.641 MeV 3^- state, two 0^+ components at $E_x = 9.04$ MeV and $E_x = 10.56$ MeV, as well as the 10.844 MeV 1^- state. The individual lineshapes of these states are also shown with blue dashed curves. They were produced using different methods. The Gaussian distribution was used to produce the lineshape of the Hoyle state and the two broad 0^+ components. For the 9.641 MeV 3^- state the R-matrix formalism was utilized. The Lorentzian function was used to produce the 10.844 MeV 1^- state. To produce the fit only the amplitudes of the states were allowed to vary whereas their resonance energy and width were fixed. For the narrow states, however, the width was convolved with the experimental resolution of 28 keV. From the figure, it is evident that the fit fails to reproduce the data in the energy range between 9.7 and 10.5 MeV. This fit has a $\chi^2/d.o.f$ value of 10. The failure to reproduce the data was also associated with the missing strength of the 2^+ state in ^{12}C. To account for this strength a 2^+ strength was added to the fitting procedure. The resulting fit is shown in Fig. 7.22 (solid red curve). The 2^+ lineshape added to the fit is shown with the hatched area. To produce this fit, different 2^+ strengths were tested by varying the resonance energy, width and the amplitude. This process was performed while investigating the value

of $\chi^2/d.o.f$ of each fit. The fit that produced the best $\chi^2/d.o.f$ value was then chosen and is represented by solid red curve. The final 2^+ parameters used to produce the best fit are 9.97 $\pm$ 0.20 MeV and 1.03 $\pm$ 0.21 MeV for resonance energy and width respectively. The $\chi^2/d.o.f$ value obtained with this fit is 3.96.

Comparing these 2^+ parameters with the ones obtained from the singles spectrum, one can see that there is a shift in the resonance energy while the width decreased. The resonance energy shifted to higher energy by 310 keV whereas the width decreased by 60 keV. This shift in resonance is a result of barrier effects which are expected to affect resonance α-decay. These potential barrier effects on resonance formation and decay are discussed later in this chapter.

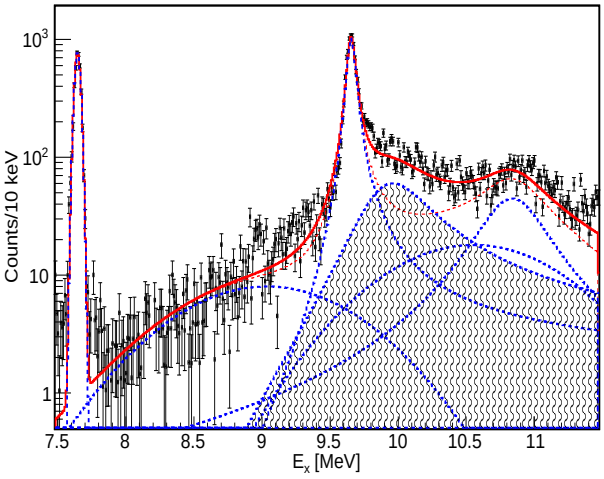

Figure 7.22: The ^{12}C excitation energy spectrum produced from ^{8}Be$_{gs}$ decay gated events. Also shown are fits produced using different procedures (see text).

7.2.2.2 Breakup through other Decay Modes

As illustrated in Fig. 7.19(a), two types of gates can be applied in order to study different decay modes i.e. ^{8}Be ground state mode and other decay modes. The locus shown as "other" in Fig. 7.19(a) represents events where the excited ^{12}C

nucleus decays through modes that could not be exclusively separated from one another. Efforts were made in the present study to investigate the ^{12}C excitation energy spectrum produced by gating on these decay modes.

Firstly, a detection efficiency correction is required in order to get an excitation energy spectrum which is independent of efficiency. This was done using a similar manner as done for the ^{8}Be ground state gated events. Figure 7.23 shows the efficiency plot for double coincidence events simulated by assuming a resonance in ^{8}Be at excitation energy $E_x = 1.8$ MeV and width $\Gamma = 1$ MeV. These values were obtained by characterizing the broad bump located between 0.2 - 3 MeV as seen Fig. 7.17. It is clear from Fig. 7.23 that as the excitation energy increases the detection efficiency decreases. Thus, one would need to perform an efficiency correction to account for the detection efficiency at higher excitation energy region.

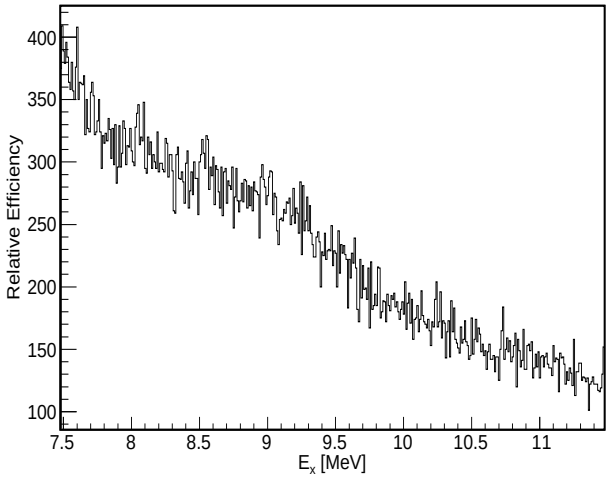

Figure 7.23: Efficiency plot showing how the Silicon array efficiency varies with excitation energy for double coincidence events simulated for other decay modes.

Figure 7.24 shows the ^{12}C excitation energy spectra produced by gating on other decay modes as indicated by the green locus in Fig. 7.19(a), before (red) and after (black) the efficiency correction. It is visible that applying the efficiency correction resulted in the boost in the counts for the excitation

energy spectrum. The peak fitting analysis was also performed in order to fit the efficiency corrected ^{12}C excitation energy spectrum.

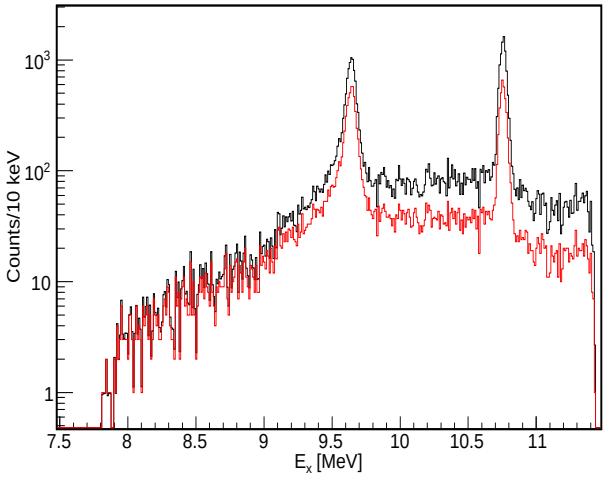

Figure 7.24: The ^{12}C excitation energy spectra produced by gating on other decay modes before efficiency correction (black) and after the correction (red).

Figure 7.25 shows the ^{12}C excitation energy spectrum produced by gating on other decay modes. Also shown is the fit (red dashed) produced using the following states: the 9.641 MeV 3^- state, two 0^+ components at $E_x = 9.04$ MeV and $E_x = 10.56$ MeV, as well as the 10.844 MeV 1^- state. It is expected that the Hoyle state decays exclusively through ^{8}Be ground state decay mode. Hence, by gating on other decay modes the Hoyle state is expected to vanish. The individual lineshapes of the included states are represented by blue dashed curves. They were produced using different methods. The Gaussian function was used to produce the lineshapes of the two broad 0^+ components. The R-matrix calculations were utilized for the 9.641 MeV 3^- state. The 10.844 MeV 1^- state was produced using the Lorentzian function. To produce the fit only the amplitudes were allowed to vary while their resonance energy and width were fixed parameters. From the figure, it is evident that the fit fails to reproduce the measure spectrum in the excitation energy range between 9.1 and 10.5 MeV. This fit has a $\chi^2/d.o.f$ value of 11.55. The failure to reproduce

data was also associated with the missing strength of the 2^+ state in ^{12}C at this excitation energy region. To account for this strength a 2^+ strength was added to the fitting procedure. The resulting fit is shown in Fig. 7.22 (solid red curve). The 2^+ lineshape added to the fit is shown with the hatched area. To produce the fit, different 2^+ strengths produced with R-matrix formalism were tested by varying the resonance energy, width and the amplitude. This process was performed while investigating the value of $\chi^2/d.o.f$ obtained from each fit. The fit that produced the lowest $\chi^2/d.o.f$ value was chosen and is represented by solid red curve. The 2^+ resonance parameters that yielded the best fit are 9.55 ± 0.22 MeV and 1.15 ± 0.24 MeV for resonance energy and width respectively. The $\chi^2/d.o.f$ value obtained with this fit is 5.56.

From the 2^+ parameters obtained above, it is visible that there is a shift in both the resonance energy and width with respect to parameters obtained from singles spectrum. The resonance energy shifted to lower energy by 140 keV while the width decreased by 284 keV. It should be noted that the shift was also observed for the ground state gated events with the difference being that for the ground state the resonance energy shifted to higher energy. The shift in the parameters is also associated with the effects of the potential barrier expected to affect the resonance decay near decay threshold.

Barrier Effects on Resonance α-Decay

It has already been emphasized in Chapter 6 that the formation and the decay of resonances near the α-decay threshold can be affected by an additional barrier to the Coulomb barrier, namely the centrifugal barrier. The potential barrier experienced by the α-particle within the ^{12}C nucleus is defined as [74]:

$$V(r) = \frac{Zze^2}{r} + \frac{l(l+1)\hbar^2}{2Mr^2} \ , \tag{7.1}$$

where the r is the distance between the α-particle and the ^{8}Be nucleus, Ze and ze are respectively the charges of α-particle and ^{8}Be nucleus, M is the mass

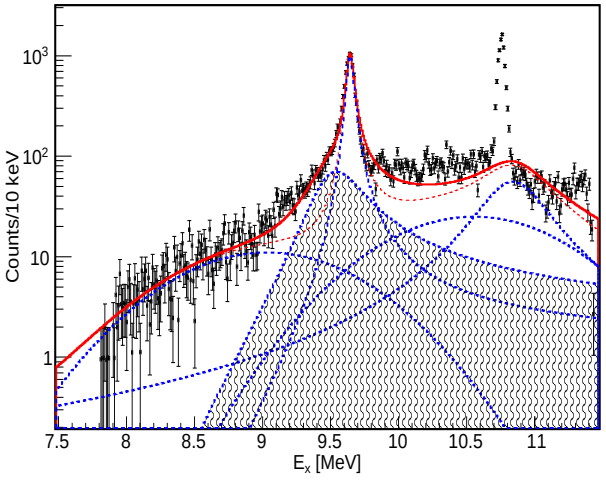

Figure 7.25: The ^{12}C excitation energy spectrum produced by gating on other decay modes. Also shown are two fits as well as the lineshapes of the individual resonances added to the fits.

of the ^{12}C nucleus and l represents the angular momentum. The first term of Eq. (7.1) represents the Coulomb barrier while the second is the centrifugal barrier. The angular momentum differs for formation and decay of the ^{12}C nucleus. For the formation process, l represents the angular momentum of the resonance at which the ^{12}C nucleus was formed. For the α-decay, however, l represents the angular momentum of the α-particle relative to the ^{8}Be nucleus. It is clear from Eq. (7.1) that for $l = 0$, the second term (centrifugal barrier) vanishes.

Since the sequential decay of the 2^+ resonance is open to both two distinct decay modes, namely the ground state and the first excited state of the ^{8}Be nucleus, the angular momentum of the α-particle relative to the ^{8}Be nucleus will be different for the two decay modes. For the ground state decay mode, the angular momentum of the α-particle relative to the ^{8}Be nucleus would two while the angular momentum of the α-particle relative to the ^{8}Be nucleus for the first excited state decay mode is zero. For zero angular momentum the second term in Eq. (7.1) will vanish, thus the α-particle will experience two different potential barrier for the two decay modes. As a result, the α-particles

will penetrate the barrier from different sides of the resonance leading to the shift in the excitation energy obtained by gating on these two distinct modes and two sets of 2^+ parameters would be obtained.

Figure 7.26 shows the 2^+ lineshapes used in producing the best fits for singles (black), the ^{8}Be ground state gated (blue), as well as the other decay modes (red) events. It is clear that by gating on the ^{8}Be ground state, the lineshape of the 2^+ resonance shifts to higher energy with respect to the singles lineshape. For the other decay modes, however, the resonance shifted to lower energy. These shifts are due to the barrier effects explained above.

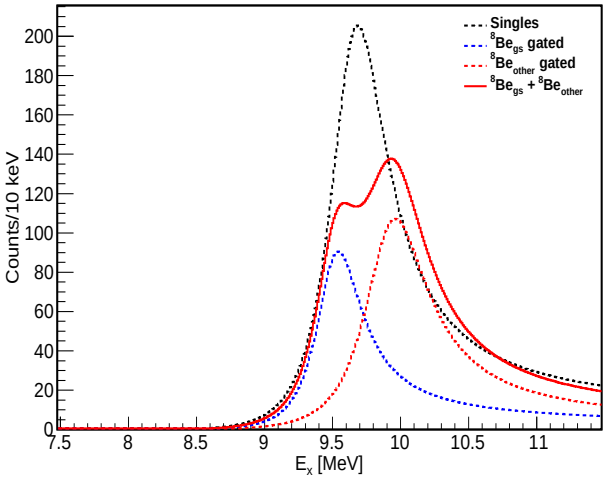

Figure 7.26: The 2^+ lineshapes used in fitting the singles (black), ^{8}Be ground state gated (blue), and other decay modes (dashed-red) events. The solid red curve shows the combination of the ^{8}Be ground state gated and the other decay modes.

7.2.2.3 Experimental α-Decay Branching Ratio

As illustrated in Table 7.6 one can theoretically calculate and compare the decay modes of excited states in ^{12}C nucleus. This can also be done experimentally as was done by Manfredi *et al.* for the Hoyle state and the 9.641 MeV 3^- state [14]. Using the obtained values one can determine the decay modes that dominate for certain excited states. From Table 7.6 the newly found 2^+

state can be associated with the state located at $E_x = 8.66$ MeV. This state should be dominated by the decay through the ^{8}Be ground state with 97% decay via ground state while only 3% decaying through other modes. From the measurement performed in the present study it was possible to determine the decay mode that dominate the newly found 2^+ state. This was done using the 2^+ resonance lineshapes shown in Fig. 7.26.

In order to do this the absolute efficiencies of the 2^+ resonance to both decay modes were obtained from the Monte Carlo simulations. The simulations were performed with the following information for the ^{8}Be nucleus:

- The ground state decay mode was simulated using $E_x = 0.09$ MeV with width of $\Gamma = 5.57 \times 10^{-6}$ MeV.
- The other decay mode was simulated using $E_x = 1.8$ MeV with width of $\Gamma = 1.4$ MeV. The parameters were obtained by characterizing the broad bump in Fig. 7.17.

The experimental branching ratio, BR, is the ratio between the decay rate N_A of an individual decay channel of a state and the total decay rate, N_T, of that state and is

$$BR = \frac{N_A/\epsilon_A}{N_T} \times 100\% = \frac{\text{no of counts in Silicon Array}/\epsilon_A}{\text{no of counts in K600 (singles)}} \times 100\% \ , \quad (7.2)$$

where ϵ_A is the detection efficiency obtained from simulations. The value of N_T (number of counts in K600) for the 2^+ resonance is found by integrating the fitted singles lineshape while the value of N_A (number of counts in silicon array) is found by integrating the fitted 2^+ lineshape obtained from each decay mode. The ratio is multiplied by 100 for comparison with the values presented in Table 7.6.

Table 7.7 shows the measured ratios of α-decay through ^{8}Be ground state and other decay modes for the newly found 2^+ resonance of ^{12}C. The uncertainties include the statistical error in the data and the systematic uncertainty

J^π	E_x [MeV]	$^8Be_{gs}$ [%]	$^8Be_{other}$ [%]
2^+	9.69	52(3)	28(4)

Table 7.7: The calculated ratios of α-decay through $^8Be_{gs}$ and other decay modes for the newly found 2^+ resonance of ^{12}C.

arising from the imperfection of the peak fitting analysis performed. From the results it is evident that the newly found state is dominated by the decay through the ^{8}Be ground state with ∼52% of it decaying via this mode while ∼28% decay through other decay modes resulting in $^8Be_{gs}$/ $^8Be_{other}$ ratio of ∼2. With the ∼7% uncertainty on the measurement considered, a question could be asked about the missing ∼10%.

It is debatable if this state could also decay via γ-emission. Recently Rana *et al.* [32] observed the 2^+ at $E_x = 9.65$ MeV with width of $\Gamma = 0.607$ MeV and claimed that it decays to the Hoyle state via γ-emission. The γ-decay probability estimates were performed in order to investigate the plausibility of this scenario for the state observed in the present study.

The γ-Decay Probability Estimates

In order to determine whether a transition is relatively weak or strong, one can calculate the transition probabilities in Weisskopf units. It is an estimate of the single-particle transition probability for a single-particle excitation.

It is an open question whether the newly found 2^+ state would decay to the low-lying states through γ-emission. If this state were to decay through γ-emission, it would be open to the decay to the Hoyle state (E2 transition), 4.439 MeV 2^+ state (E2 transition) and the ground state (E2 transition), as illustrated in Fig. 7.27. The Weisskopf units for the decay widths for E2 transition can be calculated using the following equation [106]:

$$\Gamma_W(E2) = 4.9 \times 10^{-8} A^{\frac{4}{3}} E_\gamma^5 \ , \tag{7.3}$$

where Γ_W is the width in eV, A is the mass number of the decaying nucleus

and E_γ is the energy of the γ-ray in MeV . The newly found 2^+ has the total width of $\Gamma = 1.43$ MeV. Using Eq. (7.3) one can calculate the γ-decay width of each transition. The calculated values are as follows: $\Gamma_W = 4.07\times10^{-5}$ eV for 2^+ (9.690 MeV) $\longrightarrow$ 0^+ (Hoyle state), $\Gamma_W = 5.37\times10^{-3}$ eV for 2^+ (9.690 MeV) $\longrightarrow$ 2^+ (4.439 MeV) and $\Gamma_W = 0.12$ eV for 2^+ (9.690 MeV) $\longrightarrow$ 0^+ (ground state). From decay width obtained above, one can conclude that, for a state with the total width greater than 1 MeV the γ-decay of this state to the low-lying states is highly unlikely or it should be extremely weak if happens at all. Thus, one would conclude that the decay of the newly found 2^+ state through γ-emission is not a plausible scenario. The question now arise about the missing $\sim$10% in the decay of this state. Several possibilities could be the cause of this missing strength, namely, the electronics dead times and unconsidered geometrical uncertainties. This, however, can be investigated in the setup proposed in section 8.2.

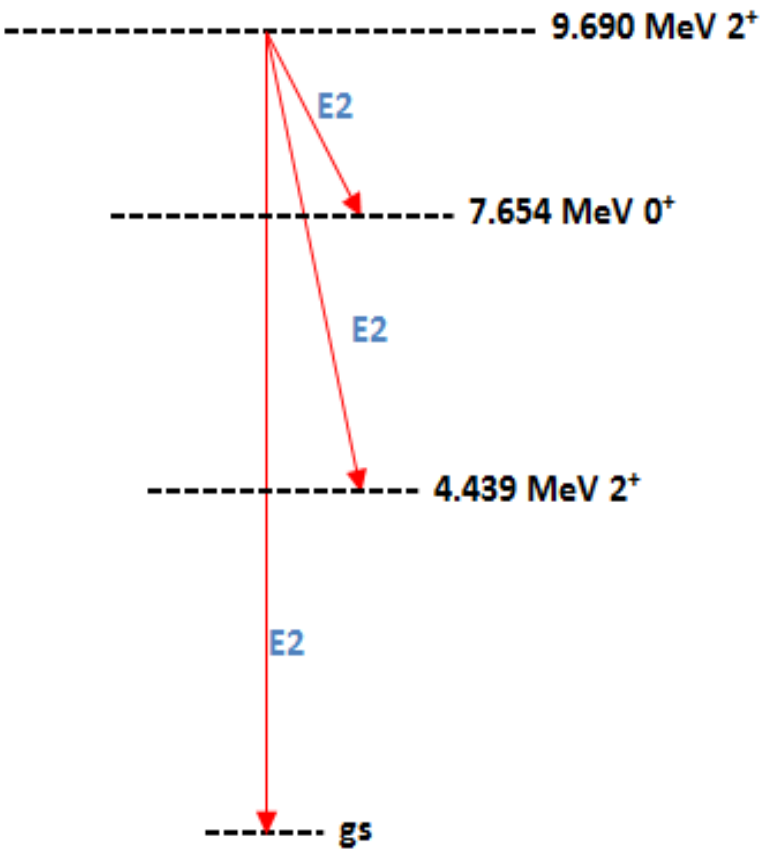

Figure 7.27: The simplified γ-decay transitions scheme of the newly found 2^+ state to the Hoyle state, 4.440 MeV 2^+ state and the ground state.

Chapter 8

Conclusions and Outlook

8.1 Conclusions

The work presented in this thesis attempted to address long-standing questions regarding the exact location of the 2^+ excitation of the Hoyle state in the ^{12}C nucleus. To complete this study two different measurements were performed.

First the excitation energy spectrum of the ^{12}C nucleus was measured using the ^{11}B(^{3}He,d)^{12}C reaction at three different laboratory angles, namely θ_{lab} = 25°, 30°, and 35°. The measurement was performed with the K600 magnetic spectrometer using a E_{lab} = 44 MeV ^{3}He beam. The primary goal of this work was to investigate the existence of the E_x = 11.16 MeV state in the ^{12}C nucleus as it was observed in the measurement reported in Ref. [24].

A detailed analysis of the ^{11}B(^{3}He,d)^{12}C measurement was performed, and no evidence of the 11.16 MeV state was observed in the present study as opposed to the original measurement. The influence of various possible contaminant reactions were investigated, but the results showed no candidate reaction capable of yielding strength around 11.16 MeV in the ^{12}C excitation energy spectrum. Therefore, the source of the apparent 11.16 MeV state seen in the original work could not be determined. A simplified peak fitting analysis was performed where the R-Matrix formalism was utilized and no strength around

11.16 MeV was required in order to reproduce the measured spectrum. The fit only required additional strength in the 10 MeV excitation energy region. These results confirmed the recent findings that showed evidence of the 2^+ resonance in the 10 MeV excitation energy region.

The results obtained from the ^{11}B(^{3}He,d)^{12}C measurement led to a more experimental work being performed in order to search for the 2^+ state in the 10 MeV excitation energy region. To do this the ^{12}C excitation energy spectrum was measured using the complete kinematics measurement of the ^{14}C(p,t)^{12}C[3α] reaction. The measurement was also performed using the K600 magnetic spectrometer at a laboratory angle of $\theta_{lab} = 21°$ coupled to a silicon detector array. It is at this angle that the CCBA calculations performed showed an enhancement of 2^+ states while the 0^+ states should be suppressed.

In addition to the population of the excited states in ^{12}C, the study of their decay properties were also required. This was achieved by utilizing the silicon detectors which were put inside the scattering chamber to detect the decay product of the ^{12}C excited states in coincidence with the tritons detected in the spectrometer focal plane.

The analysis performed on the complete kinematics measurement was twofold. The first part concentrated on singles events whereas the second part required the inclusion of the silicon coincidences. To fully understand the excitation energy spectrum obtained, a peak fitting analysis was performed to fit the singles spectrum in the excitation energy region of interest. In order to include all the known states in the fitting procedure some insight regarding the true nature of the broad 0^+ states around the 10 MeV excitation energy region was required. To do this the fitting of the ^{12}C excitation energy spectra measured with inelastically scattered protons and α-particles was performed. This method revealed that instead of the broad 0^+ component around the 10 MeV region being one state it could be be composed of two 0^+ components as was suggested in Ref. [29]. The two 0^+ components were used in the present study.

The fitting of the singles spectra required an additional 2^+ state in order to reproduce the measured spectrum. The 2^+ resonance parameters used to produce the best fit are 9.69 ± 0.11 MeV and 1.43 ± 0.22 MeV for resonance energy and width respectively. The results obtained from singles events are comparable with results obtained from other investigations [26, 27, 28, 29, 30]. The only difference between the previous studies and the parameters obtained in the present are the width of the resonance. In the present parameters, the width appears to be broader. This was associated with the fact that in the previous work, only one broad 0^+ component was used. To investigate these effects the fit was produced following the procedure in Ref. [27, 30], where only one 0^+ state at excitation energy of E_x = 10.3 MeV with width of Γ = 3.0 MeV was used. The best fit obtained using this method was found when the 2^+ resonance with energy of E_x = 9.66 ± 0.12 MeV and a width of Γ = 1.09 ± 0.17 MeV was included in the fit. This emphasizes that using two 0^+ components instead of one component affects on the resonance parameters obtained. These results show the need to further investigation into the true nature of the 0^+ state(s) in the 10 MeV region in order to obtain a precise characterization of the 2^+ resonance.

In order to probe how the newly found 2^+ resonance decays, coincidence events were analyzed. Since only the decay through the ^{8}Be ground state could be separated from other decay modes, two types of events were analyzed in the present work, namely decay via the ^{8}Be ground state and other decay modes, namely decay via the 2^+ state of ^{8}Be and democratic 3α decay. The peak fitting analysis to fit the excitation energy spectrum obtained from the ^{8}Be ground state gated events was similar to the one performed for the singles spectrum. The fit also required an additional 2^+ strength in order to reproduce the measured spectrum. The best fit was obtained with the resonance energy of E_x = 9.97 ± 0.20 MeV and a width of Γ = 1.03 ± 0.21 MeV. Interestingly, these parameters differ from the ones obtained from the singles

spectrum. This is expected since the barrier effects on the resonance formation and its decay should be different. This barrier effect is believed to be a source of the difference between the parameters obtained in Refs. [27, 29, 30], where only inclusive measurements were analyzed, and the parameters from Ref. [31], where the ^{8}Be ground state decay events were analyzed. These effects emphasize the need to perform both inclusive and exclusive measurements.

The lineshape of the 2^{+} state of ^{12}C was investigated for other decay modes than ^{8}Be ground state by excluding α_0 events. A similar peak fitting analysis revealed a shift to lower energy in the resonance energy. The parameters obtained are $E_x = 9.55 \pm 0.22$ MeV and $\Gamma = 1.15 \pm 0.24$ MeV for resonance energy and width respectively. The shift in the resonance energy also emphasizes the effects of the potential barrier on the decay of the resonance.

An attempt was made to determine the branching ratio of the decay of the newly found 2^{+} state. This was done using the 2^{+} resonance lineshapes obtained from the fit in reproducing measured spectra. The results obtained showed that this state decays predominately through the ^{8}Be ground state with $\sim$52%(3) decaying through this decay mode while $\sim$28%(4) decay through other decay modes. With the $\sim$7% uncertainties from the statistical error in the data and the systematic uncertainty. It is open question if the remaining $\sim$10% of this state could decay through γ-emission. The calculations of the Weisskopf units for the decay width performed showed that this scenario is highly unlikely.

In the present study, the inclusion of the 0^{+} strength was handled in the most simplified manner. It is a known fact that the states of the same angular momentum and parity (J^{π}) interfere [69, 92]. This effect was not included in the fitting procedure performed in the present work. Even though the fits reproduce the experimental data, it will be of best interest to perform the fitting using sophisticated R-Matrix software such as *AZURE* [99] that takes the resonance interference effects into account.

It is believed that the newly found state is the missing 2^+ band built on the Hoyle state. In terms of the prediction of such state according to cluster models calculations, the location of this state would be the one predicted by the BEC model. This would mean that this state has a well-developed α-cluster structure. Hence it also implies that both this state and its 0^+ counterpart are composed of a dilute gas of α-particles. This will rule out the possibility of α-particles being arranged in a linear form.

8.2 Outlook

From the results presented in this thesis it is evident that more work still needs to be done in order to arrive at conclusive results regarding the exact location and true nature of the 2^+ excitation of the Hoyle state. With the recent improvements in the capabilities of the K600 magnetic spectrometer, several studies can now be performed in order to better understand the structural properties of the ^{12}C nucleus.

It is a known fact that the Dalitz plot technique firstly introduced by Dalitz [100] can be used to determine the spin and parity of a state in a three body decay event. This technique was successfully used by Kirsebom *et al.* [35] to visualize and analyze data in order to determine the spin and parity of the populated states in the ^{12}C nucleus. In order to use this method the detection of all decaying products is required. In the present work, the detection efficiency for three α-particles was very low. Thus these events could not be analyzed in the present data and as a result the Dalitz plot technique could not be utilized. In order to be able to use this technique an experiment with high detection efficiency of three α-particles must be performed. With the recent acquisition of new equipment such as ADC modules, mesytec MSCF-16-F amplifier modules (which performs both signal shaping as well as time filter amplification), additional silicon detectors can now be added in the experi-

mental setup, thus making it possible to increase the 3α detection efficiency. In addition thin scintillation detectors for the focal plane have been developed and the test runs have been performed. These will make it possible to perform measurements with low beam energies where triggering through the coincidence between the two scintillation detectors can be achieved. This will make it possible to acquire data at higher beam intensities since the trigger will be cleaner.

It has already been mentioned that the true nature of the 0^+ state(s) around the 10 MeV region requires a thorough investigation. To do this one would need to perform measurements at an angle where low spin states such as 0^+ states are most likely to be populated. It has been shown that zero degree measurements can be used in this regard [101]. The development of a small angle mode scattering chamber makes it possible to perform both zero degree as well as small forward angles measurements. Performing both inelastic scattering and transfer reaction measurements at small angles will help in extracting the true nature of the 0^+ state(s) around the 10 MeV region.

One of the recent intriguing results about the nature of the 2^+ excitation of the Hoyle state come from the work performed by Rana *et al.* [32]. They found that this state could decay to three α-particles through the Hoyle state. This is worth further investigation. Recently feasibility studies were performed where γ-detectors such as a High Purity Germanium (HPGe) and a big Sodium Iodine (NaI) crystal (HAGAR) [102, 103] were used as ancillary detectors to the K600 magnetic spectrometer. The test setup is shown in Fig. 8.1. The detection of charged particles in the K600 magnetic spectrometer focal plane in coincidence with γ-rays detected with these γ-detectors was achieved. To investigate Rana's findings a measurement combining the spectrometer, γ-detectors as well as silicon detectors can be performed. This will provide answers regarding the states that γ-decay to low-lying states that subsequently decays into α-particles. Such signatures have also been seen for other states

such as the 12.71 MeV 1^+, 15.110 MeV 1^+ and the 16.105 MeV 2^+ states [104, 105].

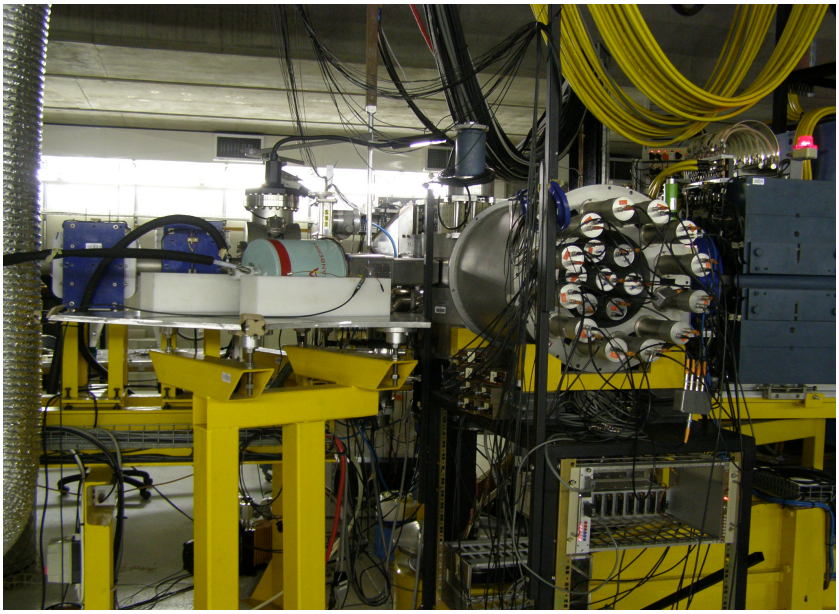

Figure 8.1: An experimental setup with both the HPGe and Hagar NaI γ-detectors placed around the scattering chamber to detect γ-rays in coincidence with charged particles detected in the K600 magnetic spectrometer focal plane.

Appendix A

Calculation of Energy and K values

Calculations for Table 4.1 were performed for a 5 MeV deuterons fieldset. For this setting, it is assumed that deuterons with 45 MeV energy will arrive at the mid point of the focal plane with momentum P_{cen}. Deuterons with minimum energy will arrive at the lower momentum side of the focal plane with momentum P_{min}, while those with maximum energy will arrive at the high momentum side with momentum P_{max}. This is illustrated in Fig A.1. The K600 spectrometer have a medium dispersion momentum range of

$$\frac{P_{max}}{P_{min}} = 1.097 \ . \tag{A.1}$$

From Fig. A.1 it can be seen that

$$P_{cen} + \Delta P = P_{max} \ , \tag{A.2}$$

and

$$P_{cen} - \Delta P = P_{min} \ . \tag{A.3}$$

It then follows that

$$\frac{P_{cen} + \Delta P}{P_{cen} - \Delta P} = 1.097 \ . \tag{A.4}$$

The aim is to calculate the energy range (minimum and maximum) of deuterons at this field setting. After calculating the momentum (P_{cen}) for 45 MeV deuterons, equation (A.4) can be used to find the minimum momentum P_{min} and the maximum momentum P_{max}. P_{cen} is calculated relativistically using the following equation:

$$E_{tot} = \sqrt{P_{cen}^2 c^2 + (m_0 c^2)^2} \ , \tag{A.5}$$

where

$$E_{tot} = E_{kin} + m_0 c^2,$$

E_{tot} is the total energy, E_{kin} is the kinetic energy, and m_0 is the rest mass of deuteron. Using Eq. (A.5), P_{cen} is found to be equal to 1122.63 MeV/c. With the help of Eq. (A.4), P_{min} and P_{max} are respectively found to be equal to 1070.69 MeV/c and 1174.55 MeV/c. Now using minimum and maximum momenta values, the energy range of deuterons are calculated relativistically using equations

$$E_{min} = \sqrt{P_{min}^2 c^2 + (m_0 c^2)^2} - m_0 c^2 \ , \tag{A.6}$$

$$E_{max} = \sqrt{P_{max}^2 c^2 + (m_0 c^2)^2} - m_0 c^2 \ . \tag{A.7}$$

E_{min} and E_{max} were found to be 40.8 MeV and 49.2 MeV respectively. These energy values are used in calculating value K range values in column 3 of Table 4.1. The equation used on calculating the vaue of K in column 3 is

$$K = \frac{mE}{q^2} \ . \tag{A.8}$$

Using the these range values, one can find the energy range for different charged particles. Charged particles considered here are deuterons, protons, tritons, ^{3}He, and ^{4}He.

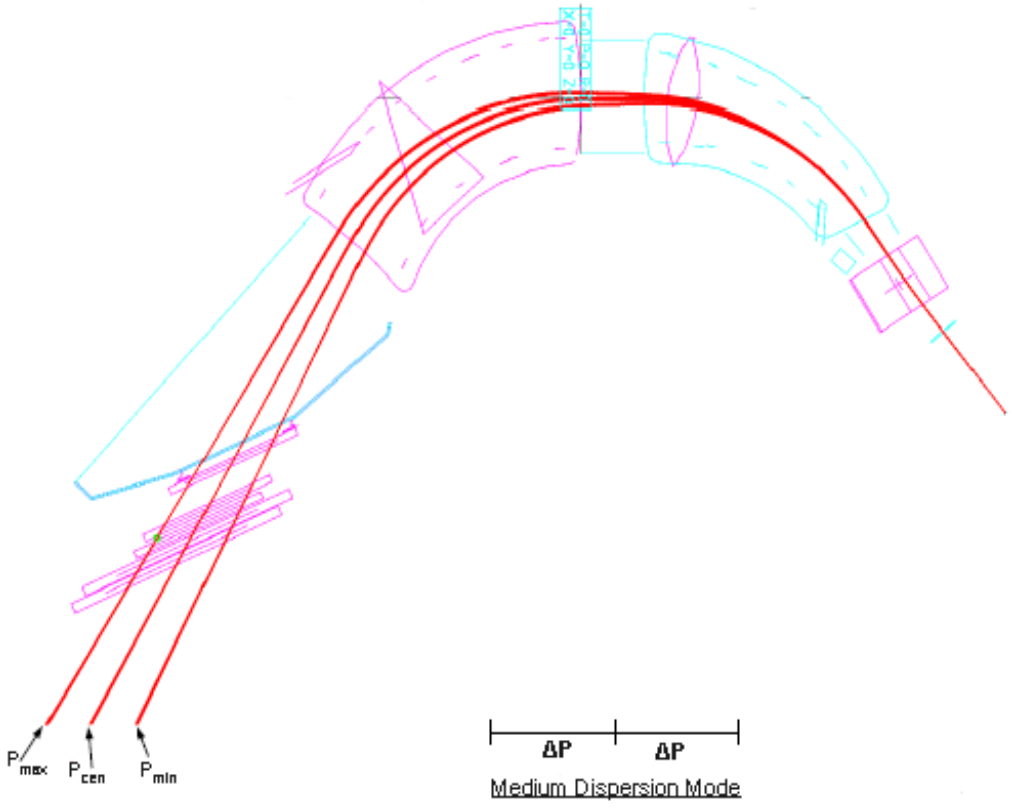

Figure A.1: The figure of the K600 spectrometer illustrating the values of P_{min} and P_{max}.

Appendix B

The SimSort Code

SimSort, which is an acronym of Simulation and Sorting code, is a software package used for simulating as well as analyzing data from nuclear physics experiments. It is mainly used in coincidence measurements, γ-ray, and charged particle spectroscopy [107]. The code was developed by P. Papka using the C++ programming language under ROOT environment. The SimSort code takes any type of data format and convert it into ROOT files. Using the software package ROOT, data are manipulated with the full capability of this very powerful package [57].

The code is basically involved with determining the kinematics information of the nuclear reactions products. Using these information, the code can extract physical information of the reactions products. To interact with SimSort, the user writes an input file. The input file should include information about the reaction of interest, number of particles to be detected, and all other conditions related to the experimental setup needed to be investigated. Using information from the input file, SimSort can then perform event sorting. Event sorting involves reading the conditions set in the input file to differentiate invalid events from valid events. Events that successfully meets the conditions are stored in a ROOT tree, for analysis while those that fail are discarded.

For all valid events, Simsort will extract information such as number of

detectors hits, strips that triggered during an event in the array, position, and energy of selected particles. Using these detectors information the velocity vectors of all the particles are deduced, hence the relative energies and angular distributions are determined.

Advantages of using SimSort is that it can be used for both simulation and experimental data analysis. For the work undertaken in this study, SimSort was used for three different purposes. Firstly SimSort was used to perform simulation prior to the experiment in order to optimize the geometrical setup of the detectors. This involves investigating where the α particles from decaying ^{12}C are expected to be detected. Different detection configurations were investigated and the setup with highest possible detection efficiency was chosen and used during the measurement. The code was also used in conjunction with the K600 spectrometer focal plane software to analyze the experimental data. Lastly SimSort was used to simulate the measurement in order to interpret experimental results. For this purpose SimSort takes into account all the conditions involved in the experiment in order to completely mimic experimental measurement.

Appendix C

Determining the Uncertainties

The uncertainties in the peak fitting process were studied by calculating the distribution in χ^2/dof of the fit to the ^{12}C excitation energy spectrum as a function of resonance energy (E_{res}) tested. The lineshape of each resonance energy and width was obtained from Eq. (6.2) and was added to the overall fit while recording the values of the resulting χ^2/dof. The uncertainty in E_{res} was determined using the values for which the total χ^2/dof was equal to χ^2/dof_{MIN} + 1 for a 68.3 % confidence level corresponding to the 1σ limit. Figure C.1 shows the calculation of the uncertainties in the 2^+ resonance energy from the distribution of χ^2/dof.

To determine the uncertainties for the resonance width the values obtained for E_{res} uncertainties (ΔE_{res}) were used. As illustrated in Eq. (6.3), the resonance width is energy dependent. One can take the widths associated with the upper and lower resonance energies as the lower and upper uncertainty values of the resonance width.

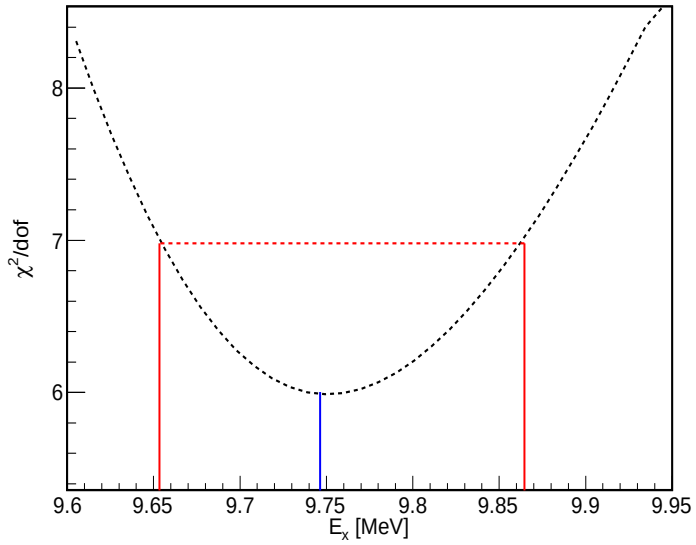

Figure C.1: The distribution in χ^2/dof for each resonance energy tested. Each point along the curve is the minimum value of χ^2/dof calculated for a particular value of the resonance energy. The red line shows the 68.3 % confidence level.

Appendix D

The iThemba LABS ^{12}C Data sets

Over the years different measurements have been undertaken to investigate the structural properties of the ^{12}C nucleus using the K600 magnetic spectrometer. Figure D.1 shows the ^{12}C excitation energy spectra measured using different probes covering an excitation energy region between 4 and 25 MeV (normalized to the Hoyle state). Information on the origin of these spectra are listed below:

- The ^{11}B(^{3}He,d)^{12}C and ^{14}C(p,t)^{12}C datasets originate from the present study.
- The spectra for inelastic scattering of a protons at laboratory angle of $\theta_{lab} = 10°$ with a proton beam energy of $E_{lab} = 66$ MeV and $\theta_{lab} = 13°$, and with proton beam energy of $E_{lab} = 200$ MeV from Ref. [27].
- The inelastic scattering of protons at the laboratory angle of $\theta_{lab} = 4°$ with a proton beam energy of $E_{lab} = 100$ MeV originates from Ref. [95].
- The inelastic scattering of α-particles at the laboratory angle of $\theta_{lab} = 0°$ with an α beam energy of $E_{lab} = 160$ MeV originates from Ref. [94].
- The spectra for inelastic scattering of α-particles at the laboratory angle of $\theta_{lab} = 9.5°$ with an α beam energy of $E_{lab} = 196$ MeV was taken from [108].

It is visible from D.1 that none of the measurement populated a state at E_x = 11.16 MeV (indicated by an arrow). This provides further supports for the findings presented in this thesis which is that the state at E_x = 11.16 MeV does not exist.

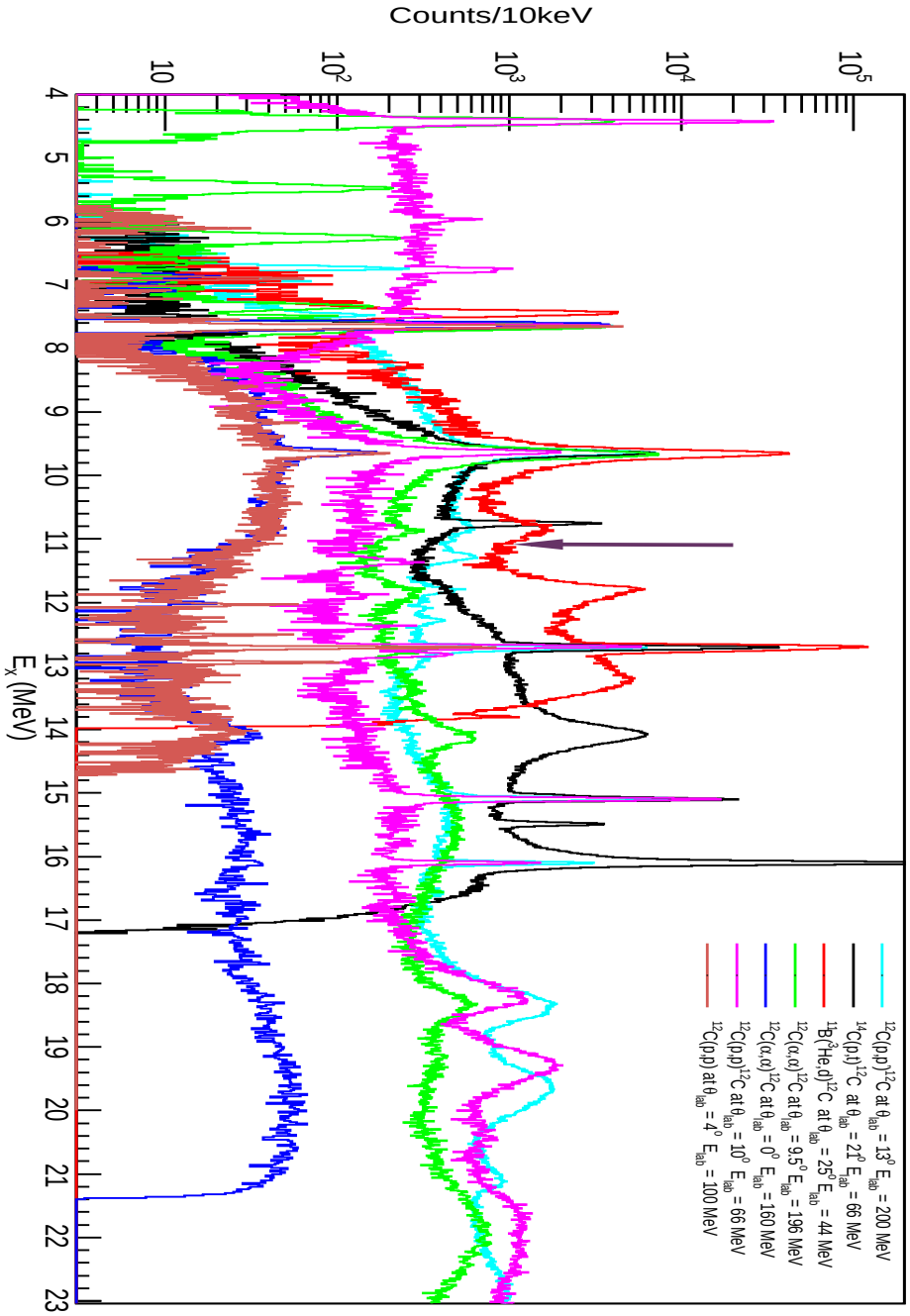

Figure D.1: The ^{12}C excitation energy spectra measured from different datasets with the K600 magnetic spectrometer at iThemba LABS.

Bibliography

[1] G. E. Brown, T. T. S. Kuo, J. W. Holt, and S. Lee, *Nucleon-Nucleon Interaction and the Many Body Problem*, (2010).

[2] B. Povh, M. Lavelle, K. Rith, and C. Scholz, Frank Zetsche, *Particles and Nuclei: An Introduction to the Physical Concepts*, (2002).

[3] G. Gamow, Oroc. Roy. Soc. A **126**, 632 (1930).

[4] C. Beck and P. Papka, in *Lecture Notes in Physics 818: Clusters in Nuclei*, edited by C. Beck (Springer-Verlag, Berlin Heidelberg, 2011).

[5] H. Horiuchi *et al.*, Prog. Theo. Phys. Suppl., 192 (1968).

[6] K. Ikeda *et al.*, Prog. Theo. Phys. Suppl., 464 (1968).

[7] R. B. Wiringa *et al.*, Phys. Rev. C **62**, 014001 (2000).

[8] F. Hoyle, Astrophys. J. Suppl. Ser. **1**, 121 (1954).

[9] C. W. Cook *et al.*, Phys. Rev. **107**, 508 (1957).

[10] Y. Fukushima *et al.*, J. Phys. Soc. Jpn. Suppl., 44 (1978).

[11] M. Kamimura and Y. Fukushima, Proc. INS *Int. Symp. on Nuclear Direct Reaction Mechanism, Fukuoka, Japan*, p. 409 (1978).

[12] M. Kamimura, Nucl. Phys. A **351**, 456 (1981).

[13] M. Chernykh *et al.*, Phys. Rev. Lett. **105**, 022501 (2010).

[14] J. Manfredi *et al.*, Phys. Rev. C **85**, 037603 (2012).

[15] Ad. R. Raduta *et al.*, Phys. Lett. B **705**, 65 (2011).

[16] O. S. Kirsebom *et al.*, J. Phys.: Conf. Ser. **436** 012072 (2013).

[17] H. Morinaga, Phys. Rev. **101**, 254 (1956).

[18] A. Tohsaki *et al.*, Phys. Rev. Lett. **87**, 192501 (2001).

[19] Y. Funaki *et al.*, Phys. Rev. C **67**, 051306 (2003).

[20] M. Chernykh *et al.*, Phys. Rev. Lett. **98**, 032501 (2007).

[21] E. Epelbaum *et al.*, Phys. Rev. Lett. **109**, 252501 (2012).

[22] A. C. Merchant *et al.*, Nucl. Phys. A **549**, 431 (1992).

[23] F. Ajzenberg-Selove *et al.*, Nucl. Phys. A **506**, 1 (1990).

[24] G. M. Reynolds *et al.*, Phys. Rev. C **3**, 442 (1971).

[25] M. Freer *et al.*, Phys. Rev. C **76**, 034320 (2007).

[26] M. Itoh *et al.*, Nucl. Phys. A **738**, 268 (2004).

[27] M. Freer *et al.*, Phys. Rev. C **80**, 041303 (2009).

[28] W. R. Zimmerman *et al.*, Phys. Rev. C **84**, 027304 (2011).

[29] M. Itoh *et al.*, Phys. Rev. C **84**, 054308 (2011).

[30] M. Freer, M. Itoh *et al.*, Phys. Rev. C **86**, 034320 (2012).

[31] W. R. Zimmerman *et al.*, Phys. Rev. Lett. **110**, 152502 (2013).

[32] T. K. Rana *et al.*, EPJ Web of Conf, **66**, 03010 (2014).

[33] C. Angulo *et al.*, Nucl. Phys. A **656**, 3 (1999).

[34] M. Gai *et al.*, J. Phys. C **267**, 012046 (2011).

[35] O. S. Kirsebom *et al.*, Phys. Rev. C **81**, 064313 (2010).

[36] D. M. Brink, *Proceedings of the International School of Physics Enrico Fermi*, Varenna Course 36: 247 (1966).

[37] D. M. Brink *et al.*, Nucl. Phys. A **216**, 109 (1973).

[38] E. Uegaki *et al.*, Prog. Theo. Phys. **62**, 6 (1979).

[39] P. Descouvemont and D. Baye, Phys. Rev. C **36**, 54 (1987).

[40] A. Ono *et al.*, Phys. Rev. Lett. **68**, 2898 (1992).

[41] A. Ono *et al.*, Phys. Rev. C **47**, 2652 (1993).

[42] Y. Kanada-Eńyo *et al.*, Phys. Rev. C **52**, 628 (1995).

[43] Y. Kanada-Eńyo *et al.*, Phys. Rev. C **52**, 647 (1995).

[44] Y. Kanada-Eńyo *et al.*, Prog. Theo. Phys. 142 (2001).

[45] Y. Kanada-Eńyo, Prog. Theo. Phys. 117 (2007).

[46] M. Chernykh *et al.*, Phys. Rev. Lett. **98**, 032501 (2207).

[47] R. Neveling, F. D. Smit, H. Fujita, and R. T. Newman, *Guide to the K600 Magnetic Spectrometer*, *unpublished*, (2011).

[48] J. A. Swartz, MSc. thesis, University of Stellenbosch, (2010), *http://hdl.handle.net/10019.1/4297*.

[49] W. Bertozzi *et al.*, Nucl. Instrum. Meth. **141**, 457 (1977).

[50] Saint-Gobain Crystals, *http://www.crystals.saint-gobain.com*.

[51] The Midas Data Acquisition System, PSI (Paul Sherrer Institute), Switzerland, *https://midas.psi.ch*, (2009).

[52] The Midas Data Acquisition System, TRIUMF, Canada, *https://midas.triumf.ca*, (2013).

[53] Technical Information Manual of MULTIHIT TDC's, CAEN, Model V1190A, *unpublished*.

[54] Mesytec MPR-32 Multichannel Preamplifier for Silicon Detectors, *User's Manual*.

[55] N. Kheswa and L. Mathebula, *private communication*.

[56] A. M. Mukhamedzhanov *et al.*, Phys. Rev. C **84**, 024616 (2011).

[57] Root web site, *http://root.cern.ch/*.

[58] P. Jipsen and J. Maritz, *Program ELOSS V2.0*, iThemba LABS (1992).

[59] K. G. Fissum *et al.*, Nucl. Instrum. Meth. A **474**, 108 (2001).

[60] R. Neveling, PhD thesis, University of Stellenbosch, (2001), *unpublished*.

[61] A. L. Negret, PhD thesis, Ghent University, (2005), *unpublished*.

[62] Decay radiation for ^{228}Th,
http://www.nndc.bnl.gov/chart/decaysearchdirect.jsp?nuc=228Th&unc=nds.

[63] Decay radiation for ^{224}Ra,
http://www.nndc.bnl.gov/chart/decaysearchdirect.jsp?nuc=224Ra&unc=nds.

[64] Decay radiation for ^{220}Rn,
http://www.nndc.bnl.gov/chart/decaysearchdirect.jsp?nuc=220Rn&unc=nds.

[65] Decay radiation for ^{216}Po, *http://www.nndc.bnl.gov/chart/decaysearchdirect.jsp?nuc=216Po&unc=nds*.

[66] Decay radiation for ^{212}Pb, *http://www.nndc.bnl.gov/chart/decaysearchdirect.jsp?nuc=212Pb&unc=nds*.

[67] Decay radiation for ^{212}Bi, *http://www.nndc.bnl.gov/chart/decaysearchdirect.jsp?nuc=212Bi&unc=nds*.

[68] Decay radiation for ^{212}Po, *http://www.nndc.bnl.gov/chart/decaysearchdirect.jsp?nuc=212Po&unc=nds*.

[69] C. Aa. Diget, PhD thesis, University of Aarhus, Denmark, (2006), *unpublished*.

[70] F. C. Barker *et al.*, Aust. J. Phys. **29**, 245 (1976).

[71] F. C. Barker and P. B. Treacy, Nucl. Phys. **38**, 33, (1962).

[72] S. Hyldegaard *et al.*, Phys. Rev. C **81**, 024303 (2010).

[73] P. Papka *et al.*, Phys. Rev. C **75**, 045803 (2007).

[74] B. B. Srivastava, *Fundamentals of Nuclear Physics*, Rastogi, (2006).

[75] F. von Hippel, Phys. Rev. D**5**, 3 (1972).

[76] W. Ning, Comm. Theor. Phys. **61**, 89 (2014).

[77] A. M. Lane and R.G. Thomas, Rev. Mod. Phys. **30**, 257 (1958).

[78] P. Descouvemont and D. Baye, *The R-Matrix Theory*, *unpublished*, (2010).

[79] G. R. Satchler, *Direct Nuclear Reactions*, Clarendon Press, Oxford, (1983).

[80] A. F. Gurbich, *Physics of the Interaction of Charged Particles with Nuclei, Lecture Notes*, (2003).

[81] I. J. Thompson, Comp. Phys. Rep. **7** 167 (1988).

[82] M. Yasue *et al.*, Nucl. Phys. A**510**, 285 (1990).

[83] S. A. Goncharov *et al.*, EPJ Web of Conf, **66**, 03034 (2014).

[84] S. E. Abdel-kariem, Appl. Rad. Isot. **64**, 925 (2006).

[85] A. J. Koning, *et al.*, Nucl. Phys. A **713**, 231 (2003).

[86] W. W. Daehnick, *et al.*, Phys. Rev. C **21**, 6 (1980).

[87] D. Y. Pang, *et al.*, Phys. Rev. C **79**, 024615 (2009).

[88] B. F. Bayman and A. Kallio, Phys. Rev. **156**, 1121 (1967).

[89] S. Cohen and D. Kurath, Nucl. Phys. A **101**, 1 (1967).

[90] D. R. William, Nucl. Instrum. Meth. **167**, 179 (1979).

[91] F. D. Smit, F. Nemulodi, *et al.*, Phys. Rev. C **86**, 3 (2012).

[92] H. O. U. Fynbo *et al.*, Nature **433**, 136 (2005).

[93] C. Kurokawa and K. Kato, Nucl. Phys. A **792**, 87 (2007).

[94] R. Neveling *et al.*, *Development of high energy resolution inelastic α-particle scattering at zero degrees*, Research Proposal to iThemba LABS PAC, (2011).

[95] H. Fujita *et al.*, *Development of a forward-angle mode for the K600 spectrometer*, Research Proposal to iThemba LABS PAC, (2011).

[96] D. E. Alburger *et al.*, Phys. Rev. C **16**, 2394 (1977).

[97] H. O. U. Fynbo *et al.*, Phys. Rev. Lett. **91**, 8 (2003).

[98] R. Álvarez-Rogriguez *et al.*, Phys. Rev. C **77**, 064305 (2008).

[99] R. E. Azuma *et al.*, Phys. Rev. C **81**, 045805 (2010).

[100] R. Dalitz, The Philosophical Magazine, **44**, 1068 (1953).

[101] J. A. Swartz, PhD. thesis, University of Stellenbosch, (2013), *http: http://scholar.sun.ac.za*.

[102] A. Zucchaiatti, PhD thesis, University of Witwatersrand, (1988), *unpublished*.

[103] D. Steyn, MSc thesis, University of Cape Town, (1990), *unpublished*.

[104] Kirsebom *et al.*, Phys. Lett. B **68**, 44 (2009).

[105] C. Aa. Diget J. Phys.: Conf. Ser. **381**, 012116 (2012).

[106] N. A. Jelly, *Fundamentals of Nuclear Physics* , (1990).

[107] P. Papka, *SimSort, Simulation and Analysis code*, *unpublished*, (2006).

[108] F. D. Smit *et al.*, *A test of making (α,α') measurements with the K600 spectrometer at finite angles.*, Research Proposal to iThemba LABS PAC, (2011).